3D Freeform Waveguides in Integrated Optics — Concepts, Modeling, and Applications

Zur Erlangung des akademischen Grades eines

DOKTOR-INGENIEURS

von der KIT-Fakultät für
Elektrotechnik und Informationstechnik
des Karlsruher Instituts für Technologie (KIT)

genehmigte

DISSERTATION

von

Aleksandar Nesic, M.Sc.

geboren in Belgrad, Serbien

Tag der mündlichen Prüfung:　　　　　　　　　　25.03.2021

Hauptreferent:　　　　　　　　　　　　Prof. Dr. Christian Koos
Korreferent:　　　　　　　　　　　　Prof. Dr. Valerio Pruneri
Korreferent:　　　　　　Prof. Dr. Dr. h. c. Wolfgang Freude

Table of contents

Kurzfassung

Die photonische Integration ermöglicht die Kombination verschiedener optischer Komponenten zu funktionalen Baugruppen in Form von integrierten photonischen Schaltungen (*engl. photonic integrated circuits* — PIC). Diese optischen Analoga von integrierten elektronischen Schaltungen finden Anwendungen in verschiedenen Bereichen der Nachrichtentechnik, der Signalverarbeitung, der Metrologie und der Sensorik. Integrierte photonische Schaltungen werden in verschiedenen Integrationsplattformen hergestellt, wie z. B. Silizium-auf-Isolator, Silizium-Nitrid, III-V-Verbindungen, und jede Integrationsplattform hat bestimmte Vor- und Nachteile. Um die Möglichkeiten der photonischen Integration voll auszunutzen, indem man das Beste aus jeder Integrationsplattform nimmt, ist es notwendig, integrierte photonische Schaltungen, gefertigt auf verschiedenen Plattformen, zu kombinieren. Eine einfache Möglichkeit, verschiedene integrierte photonische Schaltungen zu verbinden, ist 3D-Laserlithographie von 3D-gedruckten Polymerwellenleitern. Im Idealfall werden die integrierte photonische Schaltungen nebeneinander platziert, und die Wellenleitertrajektorien werden auf der Grundlage der Positionen der Kopplungspunkte auf dem PIC geplant. Dieses Konzept kann auch für die Verbindung von integrierten photonischen Schaltungen mit optischen Fasern verwendet werden, wodurch ein vollständiges optisches Packaging ermöglicht wird. Die Herausforderung besteht darin, eine optimale Wellenleitertrajektorie und -form zu finden, die zu minimalen Verlusten führt, denn die bestehenden theoretischen Verlustmodelle sind nur für bestimmte Spezialfälle gültig, und der Rechenaufwand der Maxwell-Gleichungslöser ist sehr groß. Darüber hinaus können 3D-gedruckte Wellenleiter verwendet werden, um die Flexibilität beim Entwurf von PIC-Layouts zu erhöhen, indem planare Wellenleiterkreuzungen durch 3D-gedruckte Wellen-

leiterbrücken ersetzt werden. Das Problem der nicht-planaren PIC-Topologien wird immer wichtiger, da die Anzahl der optischen Komponenten pro integrierter photonischer Schaltung über ~10^3 hinausgeht, was den Zahlen der elektronischen Komponenten in integrierten elektronischen Schaltungen in den 1970er und 1980er Jahren ähnelt. Schließlich könnte die Flexibilität der 3D-Laserlithographie als ergänzende Technologie zur 2D-Lithographie genutzt werden, um fortschrittlichere photonische Bauelemente als einfache Wellenleiter zu realisieren.

Diese Dissertation befasst sich mit der Modellierung und Simulation von 3D-Freiform-Wellenleitern sowie mit Anwendungen der 3D-Laserlithographie zur Realisierung von planaren kreuzungsfreien integrierten photonischen Schaltungen und ultrabreitbandigen Polarisationsstrahlteilern.

Zunächst führt Kapitel 1 den Leser in das Thema der Dissertation ein und liefert eine Motivation für die vorgestellte Forschungsarbeit.

Kapitel 2 liefert theoretische und technologische Grundlagen zu optischen Wellenleitern, Schaltern und polarisationsmanipulierenden Elementen in der integrierten Optik, die für ein besseres Verständnis der nachfolgenden Kapitel notwendig sind.

Kapitel 3 präsentiert einen transformationsoptischen Ansatz bei der Modellierung von Freiform-Lichtwellenleitern zur Beschleunigung von Simulationen im Zeitbereich auf einem rechteckigen Gitter. Eine Reihe von Freiform-Wellenleitern wurde mit dem erwähnten Ansatz in 3–6 Mal kürzeren Zeit im Vergleich zum konventionellen Ansatz simuliert. Die Wellenleiter wurden anschliessend 3D-gedruckt und experimentell charakterisiert, was eine gute Korrelation zu den Simulationen ergab.

Kapitel 4 stellt eine Silizium-Photonik *Switch-and-select*-Schaltung mit einer nichtplanaren Topologie vor, die mit 3D-gedruckten Wellenleiterbrücken realisiert wurde, die planare Wellenleiterkreuzungen ersetzen. Dieses Kapitel enthält auch eine graphentheoretische Analyse, die Ansätze mit Wellenleiterbrücken und mit planaren Wellenleiterkreuzungen vergleicht, sowie Richtlinien für den

Entwurf von *Switch-and-select*-Schaltungen mit einer optimalen Anzahl von Wellenleiterbrücken.

Kapitel 5 stellt einen wellenleiterbasierten ultrabreitbandigen 3D-gedruckten Polarisationsstrahlteiler und -Rotator vor. Designansatz, Simulationen, Herstellung auf der Facette einer Monomodefaser und experimentelle Charakterisierung einschließlich eines Dual-Polarisations-Datenübertragungsexperiments mit einer Durchsatzrate von 640 Gbit/s werden ebenfalls vorgestellt.

Schließlich fasst Kapitel 6 die Ergebnisse zusammen und gibt einen Ausblick auf die weitere Forschung. Die Dissertation schließt mit Anhängen und einer Publikationsliste.

Preface

Photonic integration enables combining different optical components into functional assemblies in the form of photonic integrated circuits (PIC). These optical analogons of electronic integrated circuits (EIC) are finding application within different areas that include communications, signal processing, metrology, and sensing. PIC are made using different integration platforms such as silicon-on-insulator, silicon-nitride, III-V compounds, and each integration platform has certain advantages and drawbacks. To fully exploit the capabilities of photonic integration by taking the best from each integration platform, it is necessary to combine PIC from different platforms. A straightforward way of connecting different PIC is by employing 3D-printed polymer waveguides through 3D laser lithography. Ideally, the PIC are coarsly placed close to each other, and the waveguide trajectories are planned based on the positions of the coupling points on the PIC. This concept can also be used for connecting PIC to optical fibers, thus enabling full optical packaging. The challenge is finding an optimum waveguide trajectory and shape that would result in minimum losses. This is because the existing theoretical loss models are valid only for certain special cases, and the computational effort of Maxwell's equation solvers is immense. In addition, 3D-printed waveguides can be used in adding a flexibility in designing PIC layouts by replacing planar waveguide crossings by 3D-printed waveguide overpasses. The problem of non-planar PIC topologies is becoming increasingly important as the number of optical components per PIC is going beyond $\sim 10^3$, which is similar to figures of electronic components in EIC during the 1970s and 1980s. Finally, the flexibility of 3D laser lithography could be used as a complementary technology

to standard 2D lithography for realizing more advanced photonic devices than just simple waveguides.

This thesis addresses modeling and simulation of 3D freeform waveguides as well as applications of 3D laser lithography for realizing planar crossing-free PIC, and ultra-broadband polarization beam splitters.

First of all, Chapter 1 introduces the reader to the topic of the thesis and provides motivation for the presented research work.

Chapter 2 provides the theoretical and technological basics of optical waveguides, switches, and polarization manipulating elements in integrated optics that are necessary for better understanding of subsequent chapters.

Chapter 3 presents a transformation optics approach in modeling of freeform optical waveguides for speeding-up time-domain simulations on a rectangular grid. A series of freeform waveguides was simulated using the mentioned approach in a significantly shorter time compared to the conventional approach. The waveguides were subsequently 3D-printed and experimentaly characterized, showing a good correlation to simulations.

Chapter 4 introduces a silicon photonic switch-and-select (SAS) circuit with a non-planar topology, realized with 3D-printed waveguide overpasses that replace planar waveguide crossings. This chapter also includes a graph-theoretical analysis that compares approaches with waveguide overpasses and with planar waveguide crossings, as well as guidelines for designing switch-and-select PIC with an optimum number of waveguide overpasses.

Chapter 5 presents a waveguide-based ultra-broadband 3D-printed polarization beam splitter and rotator. Design approach, simulations, fabrication on the facet of a single mode fiber, and experimental characterization including a dual-polarization 640 Gbit/s data transmission experiment are also provided.

Finally, Chapter 6 summarizes the results and gives an outlook for further research. The thesis finishes with appendices and a list of publications.

Achievements of the present work

In this thesis, 3D printed freeform waveguides were investigated from a point of view of modeling and design, as well as from a perspective of applications in integrated optics. 3D-printed freeform waveguides may play an important role in complementing planar photonic integrated circuits by adding additional degrees of freedom enabled by virtue of 3D printing.

In the following, a summary of achievements that were accomplished during the work on this thesis are provided:

Demonstration of novel transformation optics based modeling and simulations of freeform waveguides verified by experiments

Freeform waveguide 3D models were mathematically transformed into straight waveguide 3D models by applying a waveguide-trajectory-based coordinate transformation function, enabling an optimal fitting of the transformed waveguides into rectangular box shaped simulation volumes. Based on the coordinate transformation function, material properties of straight waveguides in the transformed space were calculated by using principles of transformation optics. The waveguides were simulated in the transformed and, as a reference, in the original space. Both types of simulations provided almost identical results for transmission and electric field distribution, with simulations in the transformed space being completed in a significantly shorter simulation time. The waveguides were 3D printed on a silicon photonic chip, and experimentally measured transmission values showed a good qualitative match to simulated values. The presented transformation optics approach is applicable to a wide range of numerical solvers [J1].

First demonstration of a photonic integrated circuit with a non-planar topology realized with 3D printed waveguide overpasses

A silicon photonic 4×4 switch-and-select circuit was designed and fabricated through a commercial fabless manufacturing process. The photonic integrated circuit has a non-planar topology, and it was complemented by 3D-printed waveguide overpasses, thus completely avoiding planar waveguide crossings. A layout designing algorithm for minimizing the number of waveguide overpasses and a detailed graph theoretical analysis of switch-and-select circuits has been provided. The analysis demonstrates that several orders of magnitude fewer waveguide overpasses than planar waveguide crossings are needed for realizing high-radix switch-and-select circuits. The experimentally tested waveguide overpasses exhibit better than $-2\,\mathrm{dB}$ transmission, and less than $-75\,\mathrm{dB}$ crosstalk in the C-band [J3]. The work has been originally presented at the European Conference on Optical Communications 2016 (ECOC 2016) [C4] where it was honored with the best student paper award.

First demonstration of a 3D-printed ultra-broadband waveguide-based polarization beam splitter and rotator

A waveguide-based polarization beam splitter and rotator has been designed and simulated. The device has been 3D printed on the facet of a single mode fiber and was experimentally tested. Characterization with a polarization analyzer confirms the polarization splitting and rotation predicted by the simulations, with a measured polarization extinction ratio of more than $11\,\mathrm{dB}$ in a $400\,\mathrm{nm}$ wavelength range. A dual-polarization 16QAM data transmission experiment at a wavelength of $\lambda = 1550\,\mathrm{nm}$ and a symbol rate of $80\,\mathrm{GBd}$ corresponding to an aggregate data rate of $640\,\mathrm{Gbit/s}$ demonstrates that there is no optical signal-to-noise ratio penalty compared to a commercial fiber-based polarization beam splitter [J2]. The results of this work have been included in patent applications [P1] and [P2]. *Note that the achievements related to the polarization beam splitter and rotator resulted from*

equal contributions of the author of the thesis and M. Blaicher. The author's work was focused on design and optimization of the polarization beam splitter, while the work of M. Blaicher was mainly focused on fabrication. The experimental characterization was done jointly by the author and M. Blaicher. For more details about individual contributions, see the introductory part of Chapter 5.

1 Introduction

The advent of integrated optics [1] has marked a turning point in the way how we understand optics and photonics. Miniaturization of optical components and their integration into optical systems in form of photonic integrated circuits (PIC) has numerous advantages over the traditional approach with bulky discrete optical elements. Some of the most obvious advantages are that alignment of optical components is redundant, the integrated systems are robust to movements and vibrations, the footprint is several orders of magnitude smaller, and there is a potential for a reproducible low-cost mass production through optical lithography processes. The initial application field of integrated optics were optical communications, and one of the main reasons for that is the transparency of photonic integrated waveguides in the infrared region that matches the transparency windows of optical fibers [2]. Nowadays, integrated optics is pushing its way into other application areas such as optical metrology [3, 4], optical spectroscopy [5], LIDAR [6], optical imaging [7], all-optical signal processing [8], neural networks [9], sensing and biophotonics [10], to name just a few. Yet, to fully unlock the potential of integrated optics there are a few more challenges to be overcome. Some of the most prominent are photonic packaging, restrictions of photonic integrated devices to planar structures, and polarization sensitivity.

In analogy to electronic packaging that interconnects electronic integrated circuits (EIC) into functional units, the task of photonic packaging is to interconnect and bring together PIC. Photonic packaging is especially interesting for combining different photonic integration platforms with complementary advantages. These include, e.g., silicon-on-insulator (SOI) with a high refractive index contrast and a high integration density, silicon nitride (Si_3N_4) with low loss waveguides that are

applicable for obtaining high Q-factor optical ring-resonators, and III-V platforms such as indium-phosphide (InP) with a direct energy bandgap that is suitable for lasers. In addition, to couple light in and out of a PIC it is necessary to optically connect them to optical fibers, analogously to EIC whose pads need to be electrically connected to contacts on their packaging cases or to connectors on a printed circuit board. The concept of precise chip-to-chip or chip-to-fiber alignment suffers from the difficulty of matching different mode sizes, and from involving an expensive active alignment process. Electronic packaging is done by a simple concept of interconnecting EIC with wire bonds — microscopic metallic wires. Analogously, interconnecting different PIC and optical fibers with relaxed alignment conditions into fully packaged photonic systems, while at the same time adapting different mode sizes, can be done with 3D printed polymer waveguides, also known as photonic wire bonds (PWB). This concept has been experimentally demonstrated for chip-to-chip and chip-to-fiber packaging scenarios [11–13]. However, to achieve an optimum coupling between devices interconnected by photonic wire bonds, it is necessary to find an optimum photonic wire bond shape. The optimization is typically done numerically by making a parameterized photonic wire bond 3D model and running a simulation. However, since PWB are freeform waveguides, simulations with a rectangular grid and a rectangular box simulation domain (typical for most time-domain techniques) are inefficient because the region of interest (the PWB and its close vicinity) generally involves only a small portion of the simulation domain.

When it comes to the planar nature of the PIC, an obvious issue comes with PIC with non-planar circuit topologies that require waveguide crossings. Over recent years, very efficient low-loss and low-crosstalk planar waveguide crossings have been demonstrated in SOI [14, 15] and Si_3N_4 [16] platforms. However, for very complex PIC topologies, the number of planar waveguide crossing can be huge [17], which would deteriorate the overall performance and the footprint of the PIC. One can also think of using 3D-printed waveguide overpasses instead of planar waveguide crossings. A clear advantage of a 3D-printed waveguide overpass is

2

that it can replace a multitude of planar waveguide crossings, and that in principle it can be 3D-printed between any two points on the PIC. In addition, a waveguide overpass would be physically separated from the planar waveguides that it crosses, and one could expect much better crosstalk figures compared to planar waveguide crossings.

Finally, the 3D-printing technology offers unprecedented degrees of freedom in making photonic micro- and nano devices, far beyond photonic wire bonds that are only used for the mere transport of light. The full potential of 3D-printing as a complementary technology to planar PIC for making optical devices with more advanced functionalities is yet to be unleashed. One example of such advanced functionalities would be polarization manipulation. This is of great importance for PIC that are generally optimized for TE polarization and suffer from high polarization dependent losses. Design flexibility in PIC is limited to 2D, and existing planar devices for polarization splitting and rotation in PIC typically operate in a limited wavelength range [18–20] or involve complicated multi-layer lithography steps [21, 22]. 3D-printing on the other hand unlocks a full 3D-design freedom and enables fabrication of potential devices with complex shapes that otherwise could not be fabricated with planar optical lithography processes. Such devices could be directly printed on a wide range of PIC as well as directly on optical fibers. In combination with photonic wire bonds, polarization-aware photonic packaging is achievable.

This thesis focuses on the three mentioned challenges: making simulations of 3D-printed waveguides more efficient, complementing planar PIC with 3D-printed waveguide overpasses, and using 3D-printing technology for making high-performance polarization manipulating devices which would be unrealizable with standard optical lithography processes. The thesis is structured as follows: Basic theoretical and technological concepts necessary for a better understanding of the subsequent chapters are provided in Chapter 2. In Chapter 3 a transformation optics based concept of modeling and simulating of freeform waveguides is presented. Chapter 4 introduces the concept of 3D-printed waveguide overpasses

(WOP) exemplified by a demonstrator switch-and-select (SAS) PIC in silicon photonics, alongside with a graph-theoretical analysis of the number of required WOP for realizing SAS circuits. Chapter 5 gives theoretical investigations and designs as well as simulations and experimental characterizations of a 3D-printed polarization beam splitter/polarization rotator. A summary of the thesis as well as ideas and guidelines for future work are provided in Chapter 6, and more details on presented concepts and devices together with a glossary of acronyms and symbols are given in appendix. The thesis concludes with a list of cited publications and a list of own publications.

2 Theoretical and technological background

This chapter provides an overview of theoretical and technological concepts that are fundamental for the content of subsequent chapters, where novel concepts are described in detail. First, different types of optical waveguides in integrated optics are presented, followed by a method for generating 3D models of freeform waveguides, and a state-of-the-art review of modeling 3D waveguides. Afterwards, the concept of optical switching in integrated optics is introduced, and the switch-and-select switching fabric is explained in more detail. The chapter concludes with a review of photonic devices for polarization manipulation in integrated optics.

2.1 Optical waveguides in integrated optics

Optical waveguides are fundamental optical devices in integrated optics. They form a basis on which many other optical components are built. Examples include phase shifters, Mach-Zehnder interferometers, polarizers, polarization beam splitters, wavelength filters, ring resonators, and couplers. There are different types of optical waveguides in integrated optics, and here a review of most common waveguide types is provided. To describe the waveguides we assume a coordinate system that is positioned such that x and y axes are perpendicular to, and the coordinate z is parallel to the longitudinal waveguide axis (direction of light propagation).

The simplest form of a waveguide is a slab waveguide that consists of a core layer which is infinitely extended along the x-direction and restricted along the y-direction; this layer resides on a substrate, and it is covered by a cladding material, see Fig. 2.1(a). If the cladding and the substrate are made from the same material

the slab waveguide is symmetric, otherwise it is asymmetric. The mode-field of a slab waveguide can be analytically calculated [23], and although the slab waveguide is a fiction that assumes an infinitely extended core along x, it is a basis for understanding more complex waveguides for which there is no analytical solution.
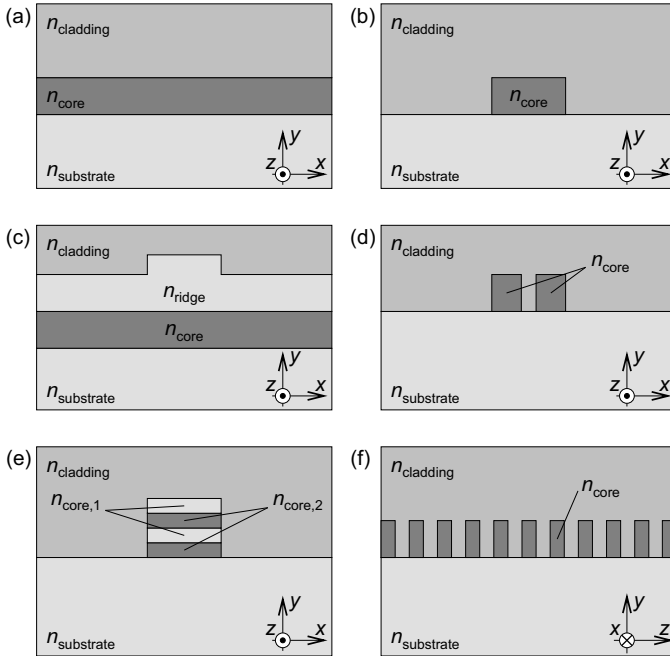
Figure 2.1: Integrated optical waveguides. (a) Slab waveguide. If $n_{substrate} = n_{cladding}$, the waveguide is symmetric, otherwise it is asymmetric. (b) Strip waveguide. If $n_{substrate} = n_{cladding}$ the waveguide is called a channel waveguide. (c) Ridge waveguide. If $n_{core} = n_{ridge}$, the waveguide is called rib waveguide, although the two names are often used interchangeably. (d) Slot waveguide. The core is selectively etched, thereby forming a slot along the z axis. The slot is filled with a low-index cladding material. (e) Multi-layer stack waveguide. The core is formed by stacked layers of different materials. (f) Sub-wavelength grating (SWG) waveguide. The core is selectively and periodically etched to form a domino like structure. The gaps between the dominoes are filled with a cladding material.

The strip waveguide is a waveguide whose core is restricted along both the x- and y-axes, resides on a substrate and is covered by a cladding, see Fig. 2.1(b). This type

of waveguide is common in silicon photonics (SiP), and typically has a relatively high attenuation of ~ 2 dB/cm due to light scattering on sidewall roughness. To alleviate this problem, the waveguide core is usually made slightly multimode, so that it is big enough to contain almost the complete field of the fundamental mode within the core; typical cross section size in SiP is $\sim (500 \times 220)$ µm^2. If the substrate and the cladding are made from the same material, the waveguide is called a channel waveguide.

A ridge waveguide is formed by placing a layer with a variable thickness (ridge layer) between the core and the cladding of a slab waveguide. More precisely, the ridge layer features a "bump" with an increased thickness and a finite width (along the x-axis), see Fig. 2.1(c). The mode-field in the core layer is concentrated under the bump, and the scattering losses due to sidewall roughness are significantly reduced compared to a strip/channel waveguide. A variant with merged core and ridge layers is called rib waveguide. The structure of a rib waveguide is simpler compared to the structure of a ridge waveguide, but at a price of higher scattering losses. The terms ridge and rib waveguide are sometimes used interchangeably in the literature.

Slot waveguides are waveguides with a slot within the core that is filled with a lower index cladding material, see Fig. 2.1(d). These waveguides are interesting because of the discontinuity of the x-component of the electric field, which is perpendicular to the core-slot interface. At this interface, due to the refractive index difference, the x-component of the electric field undergoes a jump, and has a higher value within the slot. This is because of the continuity of the normal component of the electric displacement vector at the interface between the slot and the core, $D_{x,\text{core}} = D_{x,\text{slot}}$. From here it follows that $\varepsilon_0 \varepsilon_{r,\text{core}} E_{x,\text{core}} = \varepsilon_0 \varepsilon_{r,\text{slot}} E_{x,\text{slot}}$, and finally

$$E_{x,\text{slot}} = \frac{\varepsilon_{r,\text{core}}}{\varepsilon_{r,\text{slot}}} E_{x,\text{core}}. \tag{2.1}$$

With the electric field concentrated in the slot, it is possible to fill in the slot with low-index materials that, e.g., feature second order nonlinearities (that do not

exist in silicon due to the point symmetry of its crystal lattice) and complement the integrated optics platform. This concept has been extensively used in silicon-organic hybrid (SOH) modulators [24].

In multi-layer stack waveguides, the core is made by a layered deposition of materials with different refractive indices, and a subsequent selective removal of the multi-layer stack by etching, see Fig 2.1(e), where a core made from two kinds of material has been illustrated. These waveguides are used to achieve optical anisotropy (birefringence), which can be exploited for making polarization selective devices [22] and also active optical devices [25].

Sub-wavelength grating (SWG) waveguides are waveguides whose core is periodically (along the z-axis) etched thereby forming a domino-like core structure, with gaps between the dominoes that are filled with a cladding material, see Fig. 2.1(f). The name for these waveguides originates from the fact that the gap and the domino thickness along z are much smaller than the medium wavelength of the propagating light. Dispersion engineering is obtained by adjusting the fill factor (ratio of the width of a domino to the combined width of a domino and a gap), and by choosing the cladding material. These waveguides find application in telecommunications, signal processing, and sensing [26].

A common characteristic of integrated optical waveguides is their strong polarization dependence (loss, spectral characteristics, dispersion). This is a consequence of the sub-wavelength size of the waveguide cores, and of a strong light confinement within the core. As a result, integrated optical waveguides are typically optimized for the polarization which is predominantly oriented along the x-axis, quasi-TE polarization. It should be noted that a channel waveguide with a square cross-section theoretically does not exhibit any polarization dependence, but due to a high index contrast, already slight cross section variations which are inevitable in the fabrication process would result in a polarization dependence [27].

2.1.1 Light coupling between single-mode fibers and integrated optical waveguides

Light is typically coupled into and out of integrated optical waveguides using single-mode fibers (SMF). Unlike integrated optical waveguides, SMF feature a full rotational symmetry, and they feature two degenerate polarization states of the fundamental mode. In addition, compared to integrated optical waveguides, light is only weakly guided in SMF, due to a low index contrast between the cladding and the core. As a consequence, mode field diameters (MFD) of the guided modes in optical fibers and integrated optical waveguides are very different — in optical fibers the MFD is of the order of 9 μm, while, e.g., in SiP waveguides quasi-TE polarized light has a sub-micrometer MFD, see Fig. 2.2. This poses a challenge for obtaining a low-loss coupling between SMF and integrated optical waveguides, as the mode-field sizes must be adapted. One way to do so is by using grating couplers (GC) on the surface of the PIC [28]. Grating couplers are diffraction gratings that collect light from an optical fiber and direct it to an integrated optical waveguide. This approach suffers from low bandwidth and relatively high insertion losses that can, however, be mitigated by adding a backside mirror beneath the GC [29], at the expense of additional technological complexity. Other approaches include lensed fibers and vertically bent waveguides by ion implantation [30], and 3D-printed vertically bent lensed couplers [31]. In all mentioned approaches the SMF is approaching the PIC from the top, and it is aligned with the respective coupler — this is called surface-coupling. In general, surface-coupling leads to non-planar packages, and it is hard to interface surface-coupled chips with other edge-emitting chips such as InP-based lasers. The coupling can also be done by routing an integrated optical waveguide to the edge of a PIC, and by bringing a SMF facet next to the facet of the integrated optical waveguide — this is called facet or edge coupling. The coupling efficiency in this case can be improved by using lensed fibers, various mode field adapters on the PIC side [32], or 3D-printed lenses either on the SMF and/or on the PIC side [33].

All mentioned approaches, however, require alignment of individual SMF or SMF
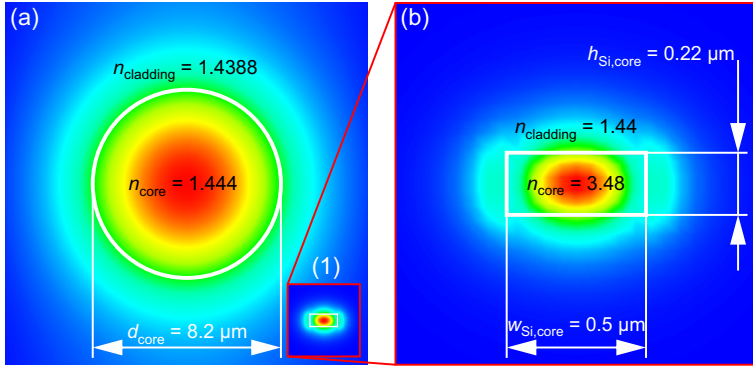
Figure 2.2: Comparison of the mode-field sizes in SMF and SiP waveguides at a wavelength of $\lambda = 1550$ nm. (a) Mode-field of the fundamental mode in a SMF. The white circle outlines the interface between the core and the cladding. Inset (1): Mode-field of the fundamental quasi-TE mode in a SiP channel waveguide, displayed at the same scale as the SMF. (b) Close-up of the mode-field of the SiP waveguide. The white rectangle outlines the waveguide core.

arrays to couplers on the PIC side. A way to avoid alignment, while at the same time having broadband coupling is to use 3D-printed freeform waveguides, so called photonic wire bonds. Furthermore, the shape and the cross-section of freeform waveguides can be made such that it includes mode-field adapters that adapt the mode sizes between the different integration platforms. This concept has been successfully used for demonstrating optical coupling between two PIC [11], between an optical fiber and a PIC [12], and a combination of both types of coupling for obtaining fully packaged multi-chip modules [13, 34]. One of the biggest challenges of this approach is finding an optimum waveguide trajectory and shape for obtaining a maximum coupling between the connected devices. The optimization of freeform waveguides is a subject of intensive research.

2.1.2 Mathematical description of 3D freeform waveguides and 3D model generation

The input data for generating a 3D freeform waveguide trajectory are coordinates of its starting and ending point in (x, y, z)-space, as well as two vectors that represent

the trajectory tangents in these two points. The trajectory is then generated as a parameterized curve, e.g. a B-spline. This curve is then subject to a systematic optimization with respect to the insertion losses of the corresponding freeform waveguide. However, if there is a time constraint for generating the trajectory, a simplified and fast optimization can be done such that only certain factors like minimum bend radius and maximum absolute value of the first derivative of the trajectory equation need to be observed. The trajectory is then discretized with sample points in (x, y, z)-space.

To generate a 3D model of the freeform waveguide, a cross-section shape in each trajectory sample is needed. In case the cross-section is circular, the only additional thing that is needed to generate the 3D model is the tangent vector $\mathbf{T}$ in all trajectory points, and it can be easily calculated. The circular cross section is approximated by a regular n-sided polygon, and the shape of the waveguide 3D model is obtained by centering the corresponding circle in each trajectory sample point such that $\mathbf{T}$ is always perpendicular to the plane of the circle. In case the cross section does not feature a full rotational symmetry, e. g., in case of an ellipse or a rectangle, generation of the 3D model requires additional thoughts. Imagining the cross-section shape as an aircraft that flies along the trajectory curve, one may define roll, pitch, and yaw angles with respect to a global coordinate system. The tangent vector $\mathbf{T}$ defines pitch and yaw angles, and to describe how the cross-section shape rolls in each trajectory point it is necessary to define the roll angle. For this purpose, a 2D coordinate frame consisting of vectors $\mathbf{U}$ and $\mathbf{V}$ that are mutually perpendicular and perpendicular to $\mathbf{T}$ needs to be defined, and one can use the rotation minimizing frame (RMF) [35, 36], which is often used in computer graphics and 3D modeling [37]. In contrast to the better known Frenet-Serret frame, which is not defined in inflection points and straight parts of the trajectory, and which rotates by 180° after each inflection point, the RMF is defined in all trajectory points, and does not rotate at inflection points. Defining the roll angle of 0° in the first trajectory point, the RMF will be rotated by a roll angle of R_1 in the last trajectory point. If the desired roll angle in the last point is

$R_2 \neq R_1$, then the difference between the desired angle and the obtained roll angle is $\Delta R = R_2 - R_1$. If the trajectory consists of m samples, then the cross-section shape in the ith sample needs to be additionaly rotated (rolled) by $\frac{i-1}{m-1}\Delta R$. In this way, the cross-section shape in the last sample will be rotated by ΔR, the cross-section shape in the second last sample slightly less, and so on until the cross-section shape in the first sample that will not undergo any rotation.

2.1.3 Modeling of optical waveguides

Finding an optimum freeform waveguide for connecting two spatially fixed optical devices and achieving maximum possible optical transmission requires an accurate loss estimation method. The problem is to find an optimum freeform waveguide trajectory between two points in 3D Cartesian space, as well as the corresponding freeform waveguide shape, i. e., a freeform waveguide cross-section along the trajectory that need not necessarily be constant. The loss mechanisms in freeform waveguides include material absorption, multi-mode excitation, radiation, scattering, and modal field mismatch. The influence of these mechanisms depends on the freeform waveguide material properties, the light polarization, as well as the freeform waveguide geometrical parameters such as trajectory length, trajectory curvature and its first derivative, freeform waveguide cross-section evolution along the trajectory, and freeform waveguide surface roughness. Although there are analytical models that tackle different loss mechanisms in optical waveguides [38–43], these models are limited to special cases by certain assumptions and simplifications, and neither one of them takes into account all loss mechanisms at the same time. Thus far, there is no universal accurate analytical model for calculating transmission losses of true freeform waveguides, and most of the research effort has been dedicated to optimizing a limited number of scenarios such as connections of a straight and a curved waveguide, S-, 90°-, and 180°-bends [41, 44–50].

Since the light propagation in freeform waveguides is governed by Maxwell's equations, the freeform waveguides can be alternatively described by numerical solvers

of Maxwell's equations. However, the freeform waveguide length is typically much larger than the wavelength of light, which leads to very large computational domains that require an immense computational effort. Consequently, the beam propagation method (BPM) has been introduced as a fast approximation technique for simulating and optimizing optical waveguides [51–55]. However, the BPM as a rule assumes slowly varying waveguides (along the propagation direction) and ignores back reflection, which renders the BPM inadequate for describing general waveguide-based optical devices that might, e. g., contain a Bragg grating or photonic crystals. In principle, it is possible to expand the BPM by taking into account back reflection and rapid spatial variations, but at the cost of the computational complexity that would become comparable to those of the rigorous solvers. Recently, the fundamental mode approximation (FMA) method for a fast transmission loss estimation and a real-time optimization of single-mode freeform waveguide was reported [56]. The FMA relies on a look-up table consisting of pre-calculated eigenmodes (propagation constants and modal field distributions) of waveguide segments with constant radii of curvature, their bending losses as well as transition losses due to modal field mismatch between two adjacent segments with different radii of curvature. The FMA discretizes freeform waveguide to segments with constant radii of curvature and calculates the transmission losses based on the look-up table. While exceptionally fast (optimization times of the order of ms with pre-calculation done), this method disregards the existence of higher-order modes, and does not provide accurate results for multi-mode waveguides.

This review shows that it is necessary to come up with new concepts for estimation of freeform waveguide losses. A possible candidate which is a compromise between loss estimation time and accuracy is the transformation optics concept [57–60]. This concept enables conversion from a freeform waveguide that has simple material properties and a complicated geometry to an equivalent transformed freeform waveguide that has a simple geometry, i. e. straight trajectory, but complicated material properties. The key advantage of the straight trajectory is that the waveguide can be optimally fit to a rectangular box computational domain,

(which is a standard for most time-domain Maxwell's equations solvers), thus reducing the overall simulation time. The details of this concept as are provided in Chapter 3.

2.2 Photonic integrated switches

3D printed waveguides can also open new perspectives in integrated optics by replacing a multitude of waveguide crossings in PIC with a single 3D-printed overpass. An example of PIC that require a large number of waveguide crossings are switching fabrics. A switching fabric is a network of switches that interconnects multiple inputs and multiple outputs. Traditionally, switching fabrics were used in telephone exchanges to establish telephone calls between subscribers, and nowadays the switching fabrics have scaled down to photonic integrated devices that interconnect optical inputs and outputs on a single photonic chip [61]. Over the last century, the mathematical theory of switching and optimizing switching fabrics has been well developed [62]. However, these optimizations were done with a view to electronics. Some aspects of switching fabrics that are not perceived as a problem in electronics can pose a challenge in integrated optics — an example is the number of crossings required for realizing the switching fabric. Comprehensive review on switch fabrics in integrated optics can be found in [63] and [64]. The focus in this thesis is on switch-and-select (SAS) fabrics, since they feature a huge number of waveguide crossings that can be replaced by 3D-printed waveguide overpasses. This is because in SAS fabrics each input must be connected with each output with a dedicated waveguide. The graph-theoretical representation of an $n \times n$ SAS fabric (n inputs and n outputs) is a complete bipartite graph $K_{n,n}$ with a number of crossings that is proportional to $n^4/16$ according to a still unproven conjecture [65, 66]. This directly maps to the number of required waveguide crossing on the PIC layout.

2.2.1 2×2 cross-bar switch

The basic building block of switching fabrics in integrated optics is a 2×2 cross-bar switch. The term cross-bar switch originates from electric switches that were historically applied in telephone exchanges. These switches were equipped with metal bars that were placed crossed or parallel to each other to achieve the two possible switch states that were accordingly named cross and bar state. A 2×2 cross-bar switch consists of two inputs, I_1 and I_2, and two outputs, O_1 and O_2. This device has two possible states: I_1 is connected to O_2 while I_2 is connected to O_1 (cross-state), and I_1 is connected to O_1 while I_2 is connected to O_2 (bar-state), see Fig. 2.3(a). An optical analog of a mechanical 2×2 cross-bar switch can be obtained by combining two multi-mode-interference couplers (MMI) and two phase shifters into a Mach-Zehnder interferometer (MZI) [61], see Fig. 2.3(b). The working principle of such a 2×2 cross-bar switch can be explained by using transfer matrices. The electric field at the 2×2 cross-bar switch inputs is described by a vector $\underline{\mathbf{E}}_I = \begin{bmatrix} \underline{E}_{I_1} & \underline{E}_{I_2} \end{bmatrix}^{\mathrm{T}}$, and at the outputs by a vector $\underline{\mathbf{E}}_O = \begin{bmatrix} \underline{E}_{O_1} & \underline{E}_{O_2} \end{bmatrix}^{\mathrm{T}}$. An MMI is described by a transfer matrix

$$\underline{\mathbf{T}}_{\mathrm{MMI}} = \frac{1}{\sqrt{2}} \begin{bmatrix} 1 & -\mathrm{j} \\ -\mathrm{j} & 1 \end{bmatrix}, \tag{2.2}$$

and the middle part with the two phase shifters is described by a transfer matrix

$$\underline{\mathbf{T}}_{\mathrm{PS}} = \begin{bmatrix} A_1 \mathrm{e}^{\mathrm{j}\varphi_1} & 0 \\ 0 & A_2 \mathrm{e}^{\mathrm{j}\varphi_2} \end{bmatrix}, \tag{2.3}$$

where $A_1, A_2 \in [0, 1]$ are amplitude transmission factors of the two phase shifters, and where φ_1, φ_2 are the phase shifts induced by the phase shifters in the two arms. We can then write the following equation:

$$\underline{\mathbf{E}}_O = \underline{\mathbf{T}}_{\mathrm{MMI}} \, \underline{\mathbf{T}}_{\mathrm{PS}} \, \underline{\mathbf{T}}_{\mathrm{MMI}} \, \underline{\mathbf{E}}_I, \tag{2.4}$$

which when expanded reads

$$\begin{bmatrix} \underline{E}_{O_1} \\ \underline{E}_{O_2} \end{bmatrix} = \frac{1}{\sqrt{2}} \begin{bmatrix} 1 & -j \\ -j & 1 \end{bmatrix} \begin{bmatrix} A_1 e^{j\varphi_1} & 0 \\ 0 & A_2 e^{j\varphi_2} \end{bmatrix} \frac{1}{\sqrt{2}} \begin{bmatrix} 1 & -j \\ -j & 1 \end{bmatrix} \begin{bmatrix} \underline{E}_{I_1} \\ \underline{E}_{I_2} \end{bmatrix}. \tag{2.5}$$

In case of lossless phase shifters, $A_1 = A_2 = 1$, the last equation reduces to
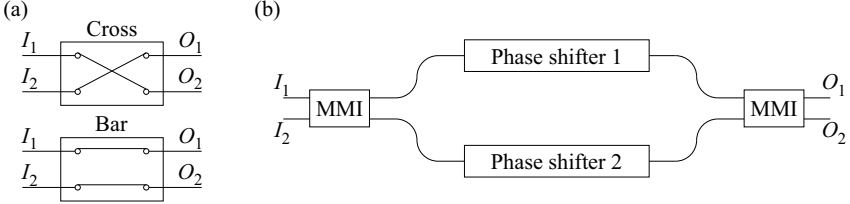
Figure 2.3: 2×2 cross-bar switch with two inputs (I_1 and I_2) and two outputs (O_1 and O_2). (a) A sketch of the cross and the bar state. (b) Realization of a 2×2 cross-bar switch in integrated optics in the form of a Mach-Zehnder interferometer. The two switch states can be achieved by adjusting the phase shifts induced by the phase shifters in the two arms, see Eqs. (2.5)–(2.8).

$$\begin{bmatrix} \underline{E}_{O_1} \\ \underline{E}_{O_2} \end{bmatrix} = \frac{e^{j\varphi_1}}{2} \begin{bmatrix} \left(1 - e^{j(\varphi_2 - \varphi_1)}\right) & -j\left(1 + e^{j(\varphi_2 - \varphi_1)}\right) \\ -j\left(1 + e^{j(\varphi_2 - \varphi_1)}\right) & -\left(1 - e^{j(\varphi_2 - \varphi_1)}\right) \end{bmatrix} \begin{bmatrix} \underline{E}_{I_1} \\ \underline{E}_{I_2} \end{bmatrix}. \tag{2.6}$$

If $\varphi_2 - \varphi_1 = 2n\pi$, where where n is an integer, the switch is in cross state:

$$\begin{bmatrix} \underline{E}_{O_1} \\ \underline{E}_{O_2} \end{bmatrix} = -je^{j\varphi_1} \begin{bmatrix} 0 & 1 \\ 1 & 0 \end{bmatrix} \begin{bmatrix} \underline{E}_{I_1} \\ \underline{E}_{I_2} \end{bmatrix}. \tag{2.7}$$

If $\varphi_2 - \varphi_1 = n\pi$, the switch is in bar state:

$$\begin{bmatrix} \underline{E}_{O_1} \\ \underline{E}_{O_2} \end{bmatrix} = e^{j\varphi_1} \begin{bmatrix} 1 & 0 \\ 0 & 1 \end{bmatrix} \begin{bmatrix} \underline{E}_{I_1} \\ \underline{E}_{I_2} \end{bmatrix}. \tag{2.8}$$

Both factors $-je^{j\varphi_1}$ and $e^{j\varphi_1}$ from Eqs. (2.7) and (2.8) have a magnitude of 1 and represent phase shifts induced by the phase shifters.

2.2.2 Switch-and-select (SAS) switching fabric based on the 2×2 cross-bar switch

Switch-and-select (SAS) is a type of switching fabric where each input is connected to each output by a separate waveguide. If a SAS connects m inputs to n outputs, there is a total of mn connecting waveguides, higher than in other switching fabrics, which requires a higher number of waveguide crossings than any other switching fabric. In SAS, each of the m inputs is equipped with a $1 \times n$ switch, and each of the n outputs is equipped with an $m \times 1$ selector. The name of the fabric is derived from the fact that for establishing a connection between an input and an output, the corresponding switch at the input and the corresponding selector at the output must be set in the desired state. The switches and selectors at the inputs and the outputs can be made as cascades of 1×2, 2×1, and 2×2 cross-bar switches, see also Chapter 4 and Appendix B — 1×2 and 2×1 cross-bar switches are simply obtained from 2×2 cross-bar switches by using only one input or only one output, see Fig. 2.4(a). The switching algorithm is simple since each switch at each input only needs to know to which of the n waveguides it needs to switch, and each selector at each output only needs to know from which of the m waveguides it needs to select. An additional advantage is good isolation of the connections between the inputs and the outputs, since no two signals can at the same time pass through any of the cross-bar switches. It should be said that there exist switching fabrics that do not require waveguide crossings [67], and such fabrics are also called crossing-free fabrics. However, such a terminology is not completely true since in this case individual 2×2 cross-bar switches serve as waveguide crossings in the cross state. Fig. 2.4(b) shows a 2×2 SAS realized with four 2×2 cross-bar switches. Obviously, one can use only one single 2×2 cross-bar switch to interconnect two inputs and two outputs, however, the isolation would be worse since both connection would be established by the same switch. The price for using the SAS fabric is an increased number of 2×2 cross-bar switches, and an increased number of waveguide crossings that scales with the fourth power of the number of inputs and outputs, see Chapter 4 and Appendix B,

where a detailed analysis of SAS circuit topologies has been presented, and where it has been shown that the number of waveguide overpasses required to realize the same circuit without waveguide crossings scales with the power of 2. This illustrates the potential of using 3D-printed waveguide overpasses in replacing planar waveguide crossings in PIC with a high topological complexity.
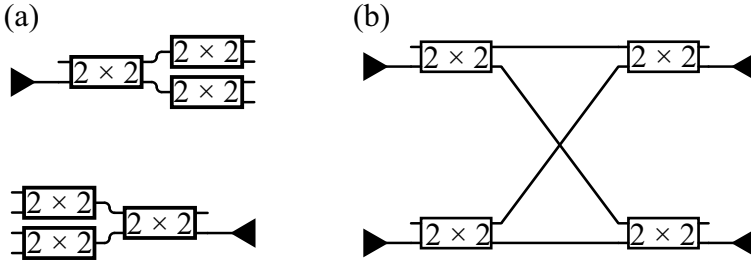
Figure 2.4: Switch-and-select (SAS) switching fabric. (a) By cascading 2×2 cross-bar switches $1 \times n$ switches at the SAS inputs and $n \times 1$ selestors at SAS outputs can be realized. Here $m = n = 4$. (b) 2×2 SAS circuit. Although a simple 2×2 cross-bar switch is sufficient to connect two inputs to two outputs, the isolation between the connection is non-optimum since both connections are established with the same 2×2 cross-bar switch. SAS improves the isolation by forbidding that two different connections at the same time use one 2×2 cross-bar switch. The price one has to pay is an increased number of 2×2 cross-bar switches in the SAS topology, and a complicated circuit layout with an increased number of waveguide crossings.

2.3 Polarization of light

Polarization of light is the geometrical orientation of the oscillations of the electric field component that is perpendicular to the propagation direction of the light. Referring the polarization to the direction of the oscillating electric field is a convention — besides the electric field, the magnetic field is also oscillating perpendicularly to the propagation direction and to the electric field. The polarization state can be described by the pattern that the real part of the electric field vector draws in the xy-plane, which is perpendicular to the direction of light propagation. These patterns are called Lissajous figures, and in general, the Lissajous figures drawn by the electric field vectors are ellipses, so called

polarization ellipses. Assuming propagation in free space, the wave equation for the x- and y- components of the electric field can be written as

$$E_x = E_{0x}e^{j(\omega t - kz)} \text{ and}$$
$$E_y = E_{0y}e^{j(\omega t - kz + \Delta\varphi)},$$

(2.9)

where $k = 2\pi/\lambda$ is a wave number, and $\Delta\varphi$ is a phase difference between the two components of the electric field. At a fixed position z, the real parts of the two components read:

$$E_x = E_{0x}\cos(\omega t - kz) \text{ and}$$
$$E_y = E_{0y}\cos(\omega t - kz + \Delta\varphi).$$

(2.10)

Equations (2.10) define the polarization ellipse [68, 69], see Fig. 2.5

$$\frac{E_x^2}{E_{0x}^2} + \frac{E_y^2}{E_{0y}^2} - 2\cos(\Delta\varphi)\frac{E_x E_y}{E_{0x}E_{0y}} = \sin^2(\Delta\varphi).$$

(2.11)

The shape and the orientation of the polarization ellipse depends on the phase difference and on the magnitudes of the two field components. The dependence is given by the following equations [69] (pg. 200, Eqs. (6.1-6) and (6.1-7))

$$\tan 2\theta = \frac{2\frac{E_{0y}}{E_{0x}}}{1 - \left(\frac{E_{0y}}{E_{0x}}\right)^2}\cos(\Delta\varphi)$$

$$\sin 2\chi = \frac{2\frac{E_{0y}}{E_{0x}}}{1 + \left(\frac{E_{0y}}{E_{0x}}\right)^2}\sin(\Delta\varphi).$$

(2.12)

In Eqs. (2.12), θ denotes the angle that the major axis of the ellipse make with the x-axis, while $|\tan(\chi)| = b/a$ denotes the ratio of the minor to the major axis of the ellipse, see Fig. 2.5. In case of $\Delta\varphi = 0 \pm n\pi$, where n is an integer, the polarization ellipse reduces to a line segment, and the light is called linearly

polarized. In case the phase difference is $\pi/2 \pm n\pi$, $n = 0, 1, 2, ...$, the polarization ellipse becomes a circle, and the light is called circularly polarized. In all other cases the Lissajous figure described by the electric field vector is an ellipse, and the light is said to be elliptically polarized. Linear and circular polarizations can be understood as special cases of elliptical polarization. In case of the circular polarization, depending on whether the circle is described by the electric field in clockwise or counterclockwise direction (when looking towards the light source), the light is said to be right or left circularly polarized [69].
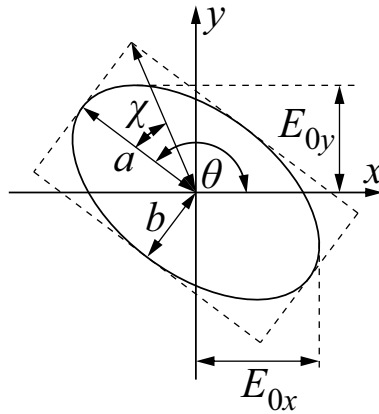
Figure 2.5: Polarization ellipse. The tip of the electric-field vector describes an elliptical Lissajous figure in the (x, y)-plane, which is perpendicular to the direction of light propagation. The state of polarization is described by the parameters θ and χ, where θ represent the direction of the major axis of the polarization ellipse, and $|\tan(\chi)|$ is the ellipticity. These parameters depend on the magnitudes E_{0x} and E_{0y} of the x- and y-components of the electric field as well as on the phase difference $\Delta\phi$ between them, as given by Eqs. (2.12). In case of linear polarization, the polarization ellipse reduces to a line segment, while for circular polarization it becomes a circle.

2.3.1 Mathematical representation of polarization

To mathematically describe the polarization of fully polarized light, a formalism called Jones calculus is used. In this formalism, the state of polarization is described by a 2D vector called Jones vector, and optical elements that modify the state of polarization are represented by (2×2) matrices, so called Jones matrices.

The change of light polarization when passing through an optical element is then mathematically described by a matrix-vector multiplication. The mathematical treatment is named after Robert Clark Jones who first described it [70]. Jones vectors consist of complex amplitudes of the electric field along the x and y axes of the plane perpendicular to light propagation. For simplicity, Jones vectors are usually normalized, and the x-component is a real number. The information that a Jones vector contains are amplitudes of the x and y components of the electric field and the phase difference between them. The Jones vector is:

$$\mathbf{J} = \begin{bmatrix} E_{0x} & E_{0y}e^{j\Delta\varphi} \end{bmatrix}^{\mathrm{T}}. \tag{2.13}$$

Jones calculus is applicable only to fully polarized light. To more generally describe the polarization state of light that is not necessarily fully polarized, Stokes vectors are used. Stokes vectors consist of four elements $\mathbf{S} = \begin{bmatrix} S_0 & S_1 & S_2 & S_3 \end{bmatrix}^{\mathrm{T}}$ that are called Stokes parameters. The parameter $S_0 = E_{0x}^2 + E_{0y}^2$ is proportional to the light intensity, and the remaining three parameters are given by [69]

$$\begin{aligned} S_1 &= S_0 \cos{(2\chi)} \cos{(2\theta)} \\ S_2 &= S_0 \cos{(2\chi)} \sin{(2\theta)} \\ S_3 &= S_0 \sin{(2\chi)}, \end{aligned} \tag{2.14}$$

where χ and θ were defined in Fig. 2.5. For simplicity, Stokes vectors can be normalized to such that

$$\mathbf{S} = \begin{bmatrix} 1 & S_1/S_0 & S_2/S_0 & S_3/S_0 \end{bmatrix}^{\mathrm{T}} = \begin{bmatrix} 1 & s_1 & s_2 & s_3 \end{bmatrix}^{\mathrm{T}}. \tag{2.15}$$

The remaining three elements of a normalized Stokes vector define Stokes three-vector $\mathbf{s} = \begin{bmatrix} s_1 & s_2 & s_3 \end{bmatrix}$ [68]. The components of this vector can then be used as parameters for representing the polarization state of fully polarized light on the surface of the Poincaré sphere, see also Appendix C.3.

2.3.2 Polarization manipulation in integrated optics

A big challenge in integrated optics is polarization control and manipulation. While a standard single mode fiber can carry two independent signals in two degenerate orthogonal polarization states of the fundamental mode, optical waveguides in PIC have a strong polarization dependence. Integrated optical waveguides have hybrid modes, which are, according to the dominant component of the electric field, called quasi-TE and quasi-TM. As already mentioned, PIC typically exploit only one preferable polarization direction that is generally parallel to the PIC surface. This polarization direction corresponds to the quasi-TE mode. The most obvious benefit of making use of the polarization component that is perpendicular to the PIC surface (quasi-TM) is for doubling the data transmission capacity in telecommunications. Other application scenarios such as optical coherence tomography, spectroscopy, lidar, or sensing can also benefit from dual polarization schemes in terms of increased sensitivity or by polarization resolved imaging. In order to employ dual polarization schemes in integrated optics it is necessary to split the two orthogonal polarizations coming from an optical fiber, to align them to the preferable polarization direction (quasi-TE), and to couple the two (now equally polarized) signals into two distinct optical waveguides on the PIC. The key components for this operation are the polarization beam splitter (PBS) and the polarization rotator (PR). In addition, polarizing filters can be used after PBS/PR assemblies for removing unwanted spurious quasi-TM polarization components and therefore increasing the polarization extinction ratio (PER).

Polarization beam splitters

PBS can be realized in integrated optics in different ways and exploiting different principles. A straightforward approach that at the same time performs optical coupling, polarization splitting, and polarization rotation is the approach with a 2D grating coupler (2D-GC). A 2D-GC consists of two identical GC that are rotated in the PIC plane by 90° with respect to each other and spatially overlapped [71]. If a SMF with two orthogonal polarization states is aligned to such a 2D-GC, each of

the two polarization states will be picked up by a different partial GC and launched to the corresponding optical waveguide attached to it. The 2D-GC launches the two orthogonal fiber polarization states as identical polarizations in the PIC waveguides. Another advantage of this approach is a relatively small footprint, and the most serious drawback is, as it is the case with all grating-based devices, their intrinsically narrow bandwidth. The insertion loss is also not negligible, although it can be improved by adding back reflection mirrors beneath the device [18]. For edge coupled PIC, where an optical fiber is aligned to an optical waveguide at the PIC edge, both polarizations are simultaneously coupled to the PIC. In this case the polarizations need to be split and the quasi-TM component needs to be rotated by $90°$. The quasi-TE and quasi-TM modes can be split by exploiting their different effective refractive indices and multimode-interference (MMI) effects [72]. An MMI-based PBS consists of a single-mode input waveguide carrying quasi-TE and quasi-TM modes. This single-mode waveguide is attached to a multi-mode waveguide section. In this section, both quasi-TE and quasi-TM higher-order modes are excited, and due to different effective refractive indices, there are two different MMI patterns for two polarizations. After a certain propagation length (beat length) through the multi-mode waveguide, the two polarizations are spatially separated, and by placing two single-mode waveguides at these two positions (where the two polarizations are separated), polarization splitting is achieved. A similar effect can be obtained by using directional couplers [73]. The difference is that the input waveguide is not connected to a multi-mode section, but another waveguide is placed in close vicinity of the input waveguide, such that mode coupling between the waveguides occurs. Since the quasi-TE and the quasi-TM fundamental modes have different effective refractive indices, the coupling coefficients and therefore the beat lengths of the modes are different. By optimizing the directional coupler it can be achieved that after a certain coupling length one of the two modes (quasi-TE and quasi-TM) remains in the original waveguide, while the other mode is coupled to the other waveguide.

MMI and directional coupler based PBS are fairly simple, however they suffer from a limited bandwidth and are sensitive to fabrication tolerances. In addition, for these two PBS types, an additional polarization rotator for rotating the quasi-TM mode is needed. Another approach for realizing a PBS with a polarization rotation function is a PBS based on mode conversion. In this approach, both quasi-TE and quasi-TM modes pass through a mode converter that converts the fundamental quasi-TM mode into the next higher order quasi-TE mode, while the fundamental quasi-TE mode goes through the mode converter unchanged. Subsequently, the TE_0 and the TE_1 modes are separated either using an MMI or a directional coupler approach, and finally the TE_1 mode is converted to TE_0 [20, 74]. This approach typically requires a complex design, suffers from a low bandwidth and has a fairly large footprint, which is especially an issue in InP [74], where the index contrast is smaller, and the footprint is by far more expensive than in the case of silicon based PIC.

A PBS can be also realized by using a mode-evolution approach. In this approach, the optical waveguide that carries the quasi-TE and the quasi-TM mode is split into two partial waveguides. The partial waveguides are designed such that for one of them, the quasi-TE mode is strongly guided, and the quasi-TM mode is weakly guided — for the other waveguide, it is the other way round. Then each of the two modes follows the partial waveguide for which it is strongly guided [21, 22]. This approach, although conceptually simple, suffers from the technological complexity, and includes multiple lithography steps with high precision mask alignment involved, and typically only very simplified structures can be made. Another issue related to this approach is the asymmetry of the split modes. This is a consequence of the technological limitations — because of the 2D lithography, it is practically impossible to realize a geometrically symmetrical PBS based on the mode-evolution approach. Consequently, the mode splitting is asymmetrical (different transmission spectra and PER at the two PBS outputs).

Finally, PBS structures designed by inverse-design method have been reported. This method involves an optimization of a spatial 2D distribution of the refractive

index such that the desired effect (in this case polarization splitting) is achieved [19]. The optimization is typically done by performing a large number of simulations and iterating the refractive index distribution. With this approach ultra-compact PBS have been achieved, however, these devices are wavelength selective and sensitive to fabrication tolerances.

Polarization rotators

As already mentioned, polarization rotators in some cases can be integrated into the PBS design while in other cases they need to be realized as separate devices. Besides the mentioned approach with the conversion of TM_0 to TE_1, and subsequent conversion of TE_1 to TE_0, a conceptually simple approach of structural chirality can be exploited for realizing broadband polarization rotators [75, 76]. If the cross-section of a geometrically birefringent optical waveguide is twisted along the trajectory, the slow and the fast guided polarization will follow the rotation of the cross-section. Similar to mode-evolution based PBS, only simplified structures can be realized using several layer-by-layer lithography steps. Such twisted waveguides can be more precisely realized by 3D laser lithography as a complementary technology to CMOS processing.

Polarization filters

For removing the unwanted polarization components and/or increasing the PER, additional polarization filters can be used. The simplest way of doing this is by cascading the PBS devices such that the desired polarization component is guided to the desired output waveguide, while the other unwanted polarization is guided to another output waveguide that serves as a beam dump. An interesting concept of filtering an unwanted quasi-TM mode is based on so called *magic widths* [77, 78]. This concept is based on finding the width of an optical ridge waveguide for which the quasi-TM mode experiences much higher propagation losses than the quasi-TE mode — such a waveguide width is called a magic width. This happens because for certain ridge widths phase matching is achieved between the TE slab field

component generated by the quasi-TM propagating mode at the ridge boundary, and a laterally propagating TE slab mode [77]. This approach is, however, very much wavelength selective, since the magic width depends on the wavelength, and it is applicable only to ridge waveguides. Other approaches such as selective mode absorption have been proposed [79], however, practical realization of such devices involves complicated technological steps.

3 Transformation-optics modeling of 3D-printed freeform waveguides

This chapter reports on transformation-optics based modeling of optical waveguides for the purpose of speeding-up time-domain simulations. The chapter is based on a manuscript [J1], that has been submitted for a publication in Optics Express, and it has been formatted in accordance to the formatting of this thesis. Supplementary information related to this chapter is provided in Appendix A, which is also based on the manuscript [J1].

The scope of the manuscript was developed by the author of this thesis together with C. Koos, and further discussed with P. Kraft, M. Sukhova, C. Rockstuhl, and W. Dörfler. The author developed transformation optics (TO) algorithms and implemented them in MATLAB code, with the support of E. Orlandini and T. Olariu. M. Blaicher provided 3D models of 3D waveguides. The author did all TO-based and reference simulations in CST Microwave Studio. M. Paszkiewicz and F. Negredo developed the fundamental mode approximation (FMA) method, and did the FMA simulations, supervised by C. Rockstuhl. M. Blaicher fabricated all 3D waveguides and performed experimental measurements. A. Hoffman did the overcladding of the fabricated 3D waveguides. The author made all figures and wrote the manuscript, supported by W. Freude and C. Koos. The work was supervised by W. Freude and C. Koos.

[start of the content based on the main part of manuscript [J1]]

Transformation-optics modeling of 3D-printed freeform waveguides

Submitted for publication to Optics Express

Aleksandar Nesic,[1] Matthias Blaicher,[1,2] Emilio Orlandini,[1] Tudor Olariu,[1] Maria Paszkiewicz,[3] Fernando Negredo,[3] Pascal Kraft,[4] Mariia Sukhova,[4] Andreas Hofmann,[5] Willy Dörfler,[4] Carsten Rockstuhl,[3,6] Wolfgang Freude,[1] and Christian Koos[1,2]

[1]*Karlsruhe Institute of Technology (KIT), Institute of Photonics and Quantum Electronics (IPQ), Engesserstrasse 5, 76131 Karlsruhe, Germany*
[2]*Karlsruhe Institute of Technology (KIT), Institute of Microstructure Technology (IMT), Hermann-von-Helmholtz-Platz 1, 76344 Eggenstein-Leopoldshafen, Germany*
[3]*Karlsruhe Institute of Technology (KIT), Institute of Theoretical Solid State Physics (TFP), Wolfgang-Gaede-Strasse 1, 76131 Karlsruhe Germany*
[4]*Karlsruhe Institute of Technology (KIT), Institute for Applied and Numerical Mathematics (IANA), Englerstrasse 2, 76131 Karlsruhe Germany*
[5]*Karlsruhe Institute of Technology (KIT), Institute for Automation and Applied Informatics (IAI), Hermann-von-Helmholtz-Platz 1, 76344 Eggenstein-Leopoldshafen, Germany*
[6]*Karlsruhe Institute of Technology (KIT), Institute of Nanotechnology (INT), Hermann-von-Helmholtz-Platz 1, 76344 Eggenstein-Leopoldshafen, Germany*

Freeform optical waveguides are key components for hybrid 2D/3D photonic integration based on the photonic wire bonding technique, which includes die-level packaging of photonic chips and fabrication of on-chip waveguide interconnects. For achieving the best device performance, the trajectories and the shapes of freeform waveguides must be optimized. However, accurate theoretical models of freeform waveguides are missing, and the computational effort of conventional

time-domain differential equation solvers is prohibitive due to large freeform waveguide simulation volumes. We present a transformation-optics (TO) modeling method to reduce freeform waveguide simulation volumes, and we set up time-domain simulations that can be completed in a significantly reduced time compared to standard methods. We checked our method by computing and fabricating a series of freeform waveguides with plane trajectories, bridging the gap between two in-line silicon-photonic waveguides, and we simulate and measure the freeform waveguide losses at $\lambda = 1550$ nm. We find an excellent agreement between the measured loss figures and those predicted by the simulations. Our TO modeling method is applicable to a wide range of waveguide-based photonic devices.

3.1 Introduction

Photonic integration has evolved into a key technology for a wide variety of applications that range from high-speed communications [80], ultra-fast signal processing [81, 82] and artificial intelligence [9] to optical metrology and sensing [4, 83–85] and to biophotonics and life sciences [10, 86]. On the technological level, photonic integrated circuits (PIC) predominantly rely on planar structures that can be fabricated with well-established microfabrication techniques based on layer deposition and 2D patterning using electron-beam or deep-UV lithography. More recently, these techniques have been complemented by multi-photon lithography that allows for in-situ fabrication of functional 3D freeform structures that can greatly enhance the functionality and versatility of planar PIC. Examples are 3D-printed chip-chip connections, so-called photonic wire bonds [12, 34] that open an attractive path towards high-performance hybrid multi-chip modules [13], 3D-printed waveguide overpasses [87], reconfigurable photonic circuits [88, 89], 3D-printed power splitters [90], or 3D-printed polarization splitters and rotators [J1]. However, while simulation tools for planar lightwave structures are available through commercial software packages [91–94], efficient modeling and design of 3D freeform waveguides still represents a challenge. This applies in particular to numerical solvers that rely on rectilinear grids within cuboid-shaped computational

29

domains, which is, e.g., the case for most time-domain techniques. Applying such solvers to 3D freeform waveguides with strongly curved non-plane trajectories requires comparatively large computational volumes, within which the structure of interest only occupies a small fraction and thus leads to poor computational efficiency.

Here, we present a transformation-optics (TO) method for reducing the computational domain of freeform waveguide simulations. We employ rigorous time-domain Maxwell's equations solvers defined on a rectilinear grid by transforming a curved freeform waveguide in the original 3D space into a straight waveguide in a virtual 3D space. In this way, the transformed waveguide in the virtual space can be confined in a rectangular simulation box, whose volume is comparable to the actual freeform waveguide volume. The rigorous simulations are performed in the virtual space at a much higher speed, and the obtained field distributions are then spatially back transformed to the original space. We investigate our method using a commercially available time-domain solver of CST Microwave Studio® (CST MWS), which is based on the finite integration technique (FIT) [95, 96]. We simulate in the virtual space a series of freeform waveguides with plane trajectories and with a rectangular cross section in a significantly shorter time compared to the corresponding reference freeform waveguide simulations in the original space. In addition, we fabricate the simulated freeform waveguides on a silicon photonic (SiP) chip and measure the transmission losses at a vacuum wavelength of $\lambda = 1550\,\text{nm}$. We get an excellent agreement between the reference and TO based simulations, and the simulated transmission losses exhibit a good qualitative match to the experimentally measured values. Although primarily aimed for use with time-domain solvers on a rectilinear grid, our method is a general technique of transforming freeform waveguide-based devices into straight structures, and it is independent of the solver.

3.2 TO based concept of freeform waveguide modeling

The TO concept relies on the fact that Maxwell's equations are form-invariant with respect to coordinate transformations. In particular, if we map an *original* domain from an (x, y, z) coordinate system, to a *virtual* domain in a (u, v, s) coordinate system, we only need to adapt the material properties in the virtual domain, while the form of Maxwell's equations remains unchanged [57–60]. In case of a coordinate transformation described by a differentiable function $(u, v, s)^{\mathrm{T}} = \mathbf{f}(x, y, z)$, where $(x, y, z), (u, v, s) \in \mathbb{R}^3$, the relationship between the material properties in the original and in the virtual space reads:

$$
\begin{aligned}
\boldsymbol{\varepsilon}'(u, v, s) &= \frac{\mathbf{J}(x, y, z) \cdot \boldsymbol{\varepsilon}(x, y, z) \cdot \mathbf{J}^{\mathrm{T}}(x, y, z)}{\det(\mathbf{J}(x, y, z))}, \\
\boldsymbol{\mu}'(u, v, s) &= \frac{\mathbf{J}(x, y, z) \cdot \boldsymbol{\mu}(x, y, z) \cdot \mathbf{J}^{\mathrm{T}}(x, y, z)}{\det(\mathbf{J}(x, y, z))}.
\end{aligned}
\tag{3.1}
$$

In these relations, the quantities $\boldsymbol{\varepsilon}$ and $\boldsymbol{\varepsilon}'$ denote the dielectric permittivity tensors, $\boldsymbol{\mu}$ and $\boldsymbol{\mu}'$ are the magnetic permeability tensors, and $\mathbf{J}$ is the Jacobian matrix of the coordinate transformation function $\mathbf{f}$,

$$
\mathbf{J} = \begin{bmatrix} \partial u/\partial x & \partial u/\partial y & \partial u/\partial z \\ \partial v/\partial x & \partial v/\partial y & \partial v/\partial z \\ \partial s/\partial x & \partial s/\partial y & \partial s/\partial z \end{bmatrix}.
\tag{3.2}
$$

Note that the transformed media in virtual space are generally anisotropic and magnetic, even if the structure in real space is made from isotropic material. The TO concept has previously been used for analysis and design of various devices, such as electromagnetic cloaks for hiding of objects [97, 98] or for reshaping the perception of cloaked objects [99], as well as for beam deflectors and expanders [100], polarization splitters and rotators [101], flat lenses [102], or multimode waveguide bends [103], to name just a few.

In our approach, we exploit transformation optics for efficient numerical modeling

of 3D freeform waveguides using well-established time-domain solvers, see Fig. 3.1 for an illustration of the concept. Generally, time-domain solvers relying, e.g., on finite-difference-time-domain (FDTD) techniques, are perfectly suited for large-scale simulations, offering a numerical complexity that scales linearly with problem size while being amenable for efficient parallelization. Moreover, time-domain techniques are robust, lend themselves to broadband or transient simulations, and even offer a natural path to handling of nonlinear behavior [104]. On the other hand, time-domain techniques usually rely on rather inflexible rectilinear grids and cuboid-shaped computational domains, which severely limits the performance when applied to 3D freeform waveguides. Specifically, the rectilinear grid does not allow for efficient representation of curved surfaces, while the cuboid-shaped computational domain leads to poor computational efficiency with comparatively large computational volumes within which the structure of interest only occupies a small fraction, see Fig. 3.1a.

To overcome these problems, we use transformation optics to map the freeform waveguide with a curved trajectory in the original (x, y, z)-space to an equivalent waveguide with a straight trajectory and modified permittivity and permeability tensors in a virtual (u, v, s)-space, see Fig. 3.1b. In the virtual space, we may then use a rectangular computational domain that only encompasses the straight waveguide and its direct vicinity, along with a rectilinear grid that is oriented along the direction of the waveguide. The virtual waveguide can thus be efficiently modeled by a conventional time-domain solver, and the results are then transformed back to the (x, y, z) coordinate system to obtain the field distributions in real space. To implement the technique, we need to define a function $(u, v, s)^{\mathrm{T}} = \mathbf{f}(x, y, z)$ that transforms the curved waveguide in real space into a straight path in virtual space. It is actually easier and more intuitive to analytically express the inverse function $(x, y, z)^{\mathrm{T}} = \mathbf{f}^{-1}(u, v, s)$ that maps a point (u, v, s) in transformed space back to real space. To arrive at a mathematical formulation of $\mathbf{f}^{-1}$, we assign the coordinate s to the arc length of the waveguide trajectory in real space, while u and
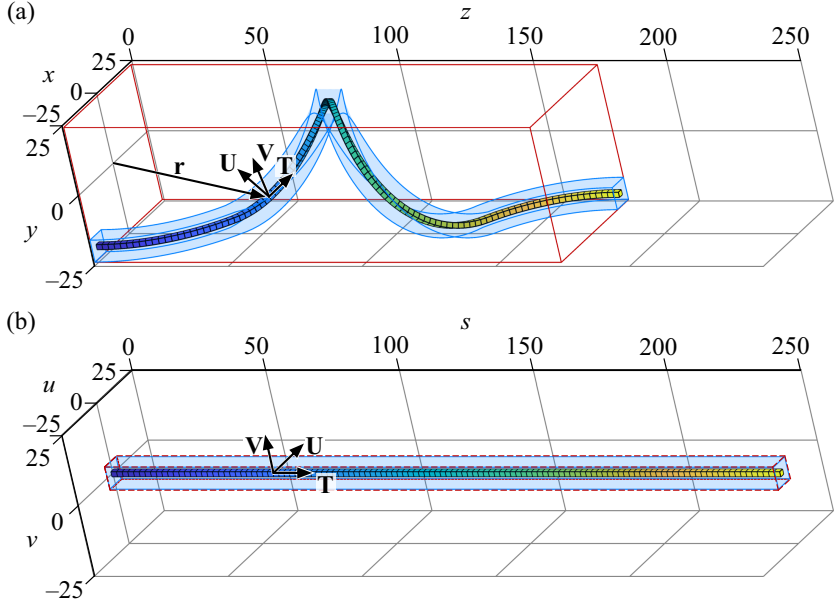
Figure 3.1: Transformation of a freeform optical waveguide from the original (x, y, z)-space to a virtual (u, v, s)-space. (a) Sample freeform waveguide in the original (x, y, z)-space. The computational domain necessary to simulate this freeform waveguide with a time-domain solver on a rectilinear grid is determined by the rectangular red box. The region of interest, i.e., the relevant part of the computational domain is in the close vicinity of the freeform waveguide – this part and its edges are depicted in blue. The rest of the computational domain is unimportant and unnecessarily consumes computing resources. Moreover, a fine discretization would be needed to correctly represent the curved surfaces of the freeform waveguide by a rectilinear computational grid. The coordinate transformation described in Eq. (3.3) is defined by the unit vectors **U**, **V**, and **T**, where **T** is the local tangent unit vector $\mathrm{d}\mathbf{r}/\mathrm{d}s$ of the trajectory, while **U** and **V** span the transverse plane in the respective trajectory point. The vectors are chosen such that $(\mathbf{U}, \mathbf{V}, \mathbf{T})$ is a right-handed trihedron. (b) Transformed waveguide in virtual (u, v, s)-space. The freeform waveguide trajectory in real space has been mapped to a straight line, and the relevant part of the computational domain that was "twisted" in the original (x, y, z)-space is now represented by a rectangular blue box. The computational domain can now be reduced to the region of interest, see red dashed rectangular box. The coordinate transformation significantly reduces the computational domain at the cost of pre-calculating the spatial distributions of tensors of dielectric permittivity and magnetic permeability in (u, v, s)-space. Moreover, the rectilinear computational grid may be better adapted to the shape of the waveguide, in particular for rectangular cross sections.

v are associated with the transverse position relative to the waveguide trajectory, where the direction is defined by unit vectors **U** and **V**. This leads to the relation

$$\mathbf{f}^{-1}(u, v, s) = \begin{bmatrix} x(u, v, s) \\ y(u, v, s) \\ z(u, v, s) \end{bmatrix} = \begin{bmatrix} x_0(s) \\ y_0(s) \\ z_0(s) \end{bmatrix} + u\mathbf{U}(s) + v\mathbf{V}(s). \qquad (3.3)$$

The s-coordinate, i.e., the arc length of the waveguide trajectory is defined such that $s = 0$ in its starting point, and the unit vectors $\mathbf{U}$ and $\mathbf{V}$ are chosen such that they form a right-handed trihedron $(\mathbf{U}, \mathbf{V}, \mathbf{T})$ with the tangent vector $\mathbf{T} = \dfrac{\mathrm{d}\mathbf{r}}{\mathrm{d}s}$, where $\mathbf{r} = (x, y, z)$. Note that the trajectory is generally not parametrized with respect to its arc length s, but with respect to some other parameter t, with $\mathbf{r}(t) = (x(t), y(t), z(t))$. The two parameterizations are connected by the relation $s = \int_0^\tau \left| \frac{\mathrm{d}\mathbf{r}}{\mathrm{d}t} \right| \mathrm{d}t$.

Equation (3.3) still leaves the freedom of choosing the orientation of the unit vectors $\mathbf{U}$ and $\mathbf{V}$ within the transverse plane in the respective trajectory point. One obvious choice for the $(\mathbf{U}, \mathbf{V}, \mathbf{T})$ frame could be the natural Frenet-Serret frame, where $\mathbf{U}$ could be chosen as the binormal vector, and $\mathbf{V}$ could be chosen as the normal vector of the trajectory $\mathbf{r}(t)$. However, the Frenet-Serret frame is not the best choice because the binormal and the normal vectors are neither defined in points where the trajectory is straight, nor in its inflection points. Furthermore, the frames immediately before and immediately after an inflection point are rotated against each other by 180° about the tangent vector. We therefore use the *rotation minimizing frame* (RMF) [35, 36], which minimizes the frame spinning along the trajectory, and which is commonly used in computer graphics and 3D modeling [37]. To calculate the RMF, we use a simple and fast approximation method called *double reflection method* [105]. This method requires the trajectory sample points, the tangent vectors $\mathbf{T}$ in all sample points, and a coordinate frame in the first sample point $(\mathbf{U}_1, \mathbf{V}_1, \mathbf{T}_1)$ as an input. The coordinate frames in the remaining sample points along the trajectory are calculated recursively [105]. The coordinate frame $(\mathbf{U}_1, \mathbf{V}_1, \mathbf{T}_1)$ in the first sample point is chosen such that $\mathbf{T}_1$ is the tangent, and the two remaining mutually perpendicular vectors $\mathbf{U}_1$ and $\mathbf{V}_1$ we can choose arbitrarily in the plane that is perpendicular to $\mathbf{T}_1$.

Note that the coordinate transformation described in Eq. 3.3 is generally not bijective. A trivial example is the case of self-intersecting trajectories, which must be excluded. Another obvious problem might arise if two waveguide segments pass by each other or overpass each other within a close distance, e. g., in spirals, helices, and loops. In this case, care must be taken to avoid mapping the same sub-domain of the (x, y, z)-space being in the vicinity of both waveguide segments twice into two distinct sub-domains of the (u, v, s)-space. Finally, bijectivity might be violated if the local curvature of the trajectory is too strong, such that the center of curvature falls into the transformed domain. Specifically, for a given trajectory point, the ranges for u and v, $u \in [u_{min}, u_{max}]$ and $v \in [v_{min}, u_{max}]$ should be chosen not to include the center of curvature for this specific trajectory point. In other words: If in this trajectory point, the center of the curvature in transformed space would be represented by (u_c, v_c), then the range of u and v for this trajectory point must be limited not to include the center of curvature, which is ensured by the condition $(u_c, v_c) \notin \{(u, v) \mid u_{min} \leq u \leq u_{max} \text{ and } v_{min} \leq v \leq v_{max}\}$. For more details, see Appendix A.1.

3.3 Implementation of TO modeling of freeform waveguides

As a proof of principle, we implemented the TO concept for simulating freeform waveguides with an invariant rectangular cross section of the core. For the coordinate transform, we use MATLAB®, and the resulting waveguide in virtual space is then treated with CST MWS, which relies on a time-domain finite-integration technique (FIT). We restricted the implementation to freeform waveguides that are made from isotropic material and that feature plane trajectories, such that the tensors $\boldsymbol{\varepsilon}'$ and $\boldsymbol{\mu}'$ are diagonal in the transformed space (see Appendix A.2). Anisotropic materials and/or non-plane trajectory would have lead to non-diagonal tensors $\boldsymbol{\varepsilon}'$ and $\boldsymbol{\mu}'$, which cannot be treated by the FIT solver of CST MWS (CST Studio Suite version 2019).

The input data for our MATLAB® code consist of the trajectory samples (x_0, y_0, z_0) in the original (x, y, z)-space, the orientation of the RMF in the initial point, and the cross-sectional shape of the waveguide along with the material properties of the core and the cladding ($\varepsilon_{\text{core}}$, μ_{core}, $\varepsilon_{\text{cladding}}$, and μ_{cladding}), and the ranges of u- and v-coordinates that define the space to be transformed. For simplicity, we chose the right-handed RMF $(\mathbf{U}, \mathbf{V}, \mathbf{T})$ in the first trajectory point such that $\mathbf{U}$ is parallel to the x-axis and $\mathbf{V}$ is perpendicular to $\mathbf{U}$ and to the tangent vector $\mathbf{T}$. We further assume a rectangular waveguide cross section with width w and height h, measured along the $\mathbf{U}$- and $\mathbf{V}$-direction of the RMF. Without loss of generality, we can assume that the plane trajectory lies in the (y, z)-plane, i.e., that the x-coordinates of all trajectory points are equal to zero. In a first step of the transformation, we numerically calculate the s-coordinate samples from the trajectory samples. The RMF in the remaining trajectory points is then calculated numerically by the aforementioned double reflection method [105]. In the special case of a plane trajectory in the (y, z)-plane, $\mathbf{U}(s)$ will always be parallel to the x-axis. Having calculated the s-coordinates with given u- and v-coordinate ranges, we have the rectangular box defining the computational domain in (u, v, s)-space. The ranges of u and v determine how much space around the trajectory will be taken into account for the TO-based simulations. These ranges should be large enough to include a sufficient portion of the cladding material around the core, but not too large, to ensure bijectivity of the function $(u, v, s)^{\mathrm{T}} = \mathbf{f}(x, y, z)$, see Appendix A.1.

In the next step, the transformed material properties in virtual space need to be calculated and fed to the numerical solver. Generally, this can be done by adapting $\boldsymbol{\varepsilon}'$ and $\boldsymbol{\mu}'$ in each point is space according to Eq. (3.1). For commercially available simulation programs with CAD-type user interfaces, however, setting the spatial variations of the materials properties on the level of individual mesh cells is not very efficient. We therefore approximate transformed structure with continuously varying material properties by a multitude of small *bricks* with constant material properties, which can be fed to the solver by a standard scripting interface. We
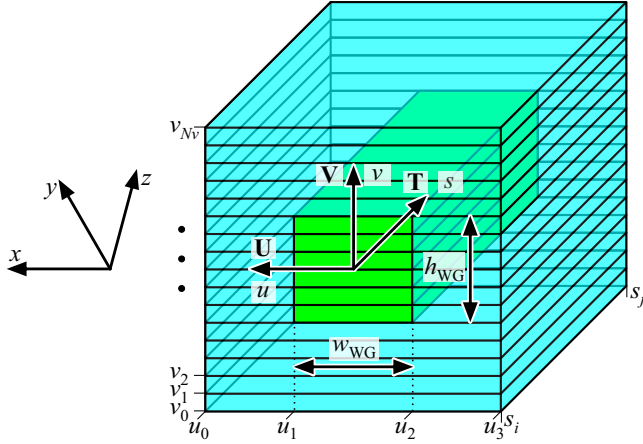
Figure 3.2: Representation of a waveguide section with a trajectory lying in the (y, z)-plane by rectangular *bricks* with constant material properties in virtual (u, v, s)-space. The freeform waveguide is discretized into sections with approximately constant curvature of the waveguide trajectory (*slices*) along s, defined by coordinates s_i and s_j . Green: Core region of the transformed freeform waveguide. Blue: Cladding region of the transformed freeform waveguide. For a freeform waveguide with a plane trajectory in the (y, z)-plane, the axis **U** of the RMF is parallel to the x-axis in all trajectory samples, which allows us to completely omit the discretization along u above and below the freeform waveguide core and to reduce the representation along u to three segments in the region of the waveguide core. The illustrated freeform waveguide slice may hence be represented by an overall of 28 bricks – 5 above and below the core, 6 on the each right and the left of the core, and 6 within the core, see Eq. 3.6.

partition the range of u-coordinates into N_u steps, the range of v-coordinates into N_v steps, and the range of s-coordinates into N_s steps. Then the total number of bricks is given by

$$N_{\mathrm{bricks}} = N_u N_v N_s .\tag{3.4}$$

Regarding the choice of the brick size, there is obviously a trade-off – too fine a discretization will require more time to calculate the material properties and more memory to store them, while too coarse a discretization might cause inaccurate simulation results. For better orientation, we provide a few rules of thumb that might help to select appropriate brick sizes. Note that these rules of thumb cannot replace a systematic convergence study for the respective waveguide cross section and for the curvature range of interest. In the following, we refer to the

discretization along *s* as *slicing*. Slicing the freeform waveguide in each sample point of the trajectory would result in a large number of *slices* N_s. We can reduce this number by exploiting the fact that each slice represents a section of the original waveguide having a constant bend radius. In a first step, we therefore calculate the bend radii in each trajectory sample $R(s)$, which is done numerically. We then step through the trajectory points and calculate the change ΔR of the radius of curvature with respect to the first trajectory point. When the relative change $\Delta R/R$ exceeds a given threshold of, e.g., 0.1, we merge all preceding points into the first slice. We then repeat the procedure by using the last sample of the first slice as a new reference for calculating the relative change $\Delta R/R$. The last slice is terminated by the last trajectory point of the waveguide. For proper choice of the brick size δu and δv along the transverse u and v direction, we need to make sure that the associated discretization of the dielectric and magnetic material properties does not introduce excessive perturbations of the optical wavefronts. As a rule of thumb we may require that, within the core and within the cladding, the difference $\delta \varepsilon'_{ij}$ and $\delta \mu'_{ij}$ of any two corresponding transformed $\boldsymbol{\varepsilon}'$- and $\boldsymbol{\mu}'$-tensor elements in any two neighboring bricks along u and v should be small compared to the difference of $\Delta \varepsilon$ between the core and the cladding of the original waveguide,

$$\left(\delta \varepsilon'_{ij} \ll \Delta \varepsilon \qquad \wedge \qquad \delta \mu'_{ij} \ll \Delta \varepsilon \right) \qquad \forall \qquad i, j \in \{1, 2, 3\}. \qquad (3.5)$$

Note that, for waveguides with strong variations of the curvature along the trajectory, it might be difficult to fulfill the inequality according to Eq. 3.5 in all grid points that are contained in a rectangular bounding box in transformed space. It should the be ensured that Eq. 3.5 applies at least to the regions that bear significant electric fields. A systematic convergence study for the respective case of interest might be unavoidable to ensure proper representation of the waveguide structure. Our proof-of-principle demonstration of the TO concept relies on a simplified waveguide structure with a plane trajectory that entirely lies in the (y, z)-plane, which allows to greatly simplify the Jacobian according to Eq. (3.2), see Eq. (A.1) of Appendix B. In this case, regions for which the material properties of the

original waveguide in real space do not change along x do not need to be subdivided into bricks along u. Since we consider a waveguide with homogeneous core and cladding region, we may reduce the transformed structure to $N_{\mathrm{u}}^{\mathrm{core}} = 3$ bricks along u in the core and $N_{\mathrm{u}}^{\mathrm{cladding}} = 1$ brick along u in the cladding region, see Fig. 3.2. The range of v-coordinates is divided into $N_{\mathrm{v}} = N_{\mathrm{v}}^{\mathrm{core}} + N_{\mathrm{v}}^{\mathrm{cladding}}$ steps, which comprises $N_{\mathrm{v}}^{\mathrm{core}}$ steps in the core region, and $N_{\mathrm{v}}^{\mathrm{cladding}}$ steps in the cladding region below and above the core. Therefore, the number of bricks per slice in this case is $N_{\mathrm{u}}^{\mathrm{core}} N_{\mathrm{v}}^{\mathrm{core}} + N_{\mathrm{u}}^{\mathrm{cladding}} N_{\mathrm{v}}^{\mathrm{cladding}}$, and Eq. 3.4 becomes

$$N_{\mathrm{bricks}} = \left(N_{\mathrm{u}}^{\mathrm{core}} N_{\mathrm{v}}^{\mathrm{core}} + N_{\mathrm{u}}^{\mathrm{cladding}} N_{\mathrm{v}}^{\mathrm{cladding}} \right) N_{\mathrm{s}} . \tag{3.6}$$

The example shown in Fig. 3.2 corresponds to the discretization that we did to perform simulations in the (u, v, s)-space and it features $N_{\mathrm{u}} = 3$, $N_{\mathrm{v}}^{\mathrm{core}} = 6$, and $N_{\mathrm{v}}^{\mathrm{cladding}} = 5 + 5 = 10$ steps. This corresponds to $3 \cdot 6 + 1 \cdot 10 = 28$ bricks per slice. The total number of bricks is therefore $28 N_{\mathrm{s}}$.

Finally, to calculate material properties of the various bricks, we first find the center point of each brick in (u, v, s)-space. We then determine the corresponding point in the original (x, y, z)-space by using Eq. 3.3, from which we derive the material properties in the original space as well as the associated Jacobian matrix given by Eq. 3.2. The material properties for the brick in the virtual (u, v, s)-space is then calculated by Eqs. 3.1. After calculating the material properties of all bricks, the MATLAB® code then generates a simulation script, which is loaded and run in the time-domain solver of CST MWS. After the simulation is done, S-parameters of the freeform waveguide can be read directly, while the field distribution must additionally undergo the inverse coordinate transformation given by Eq. 3.3, in order to be represented in the original (x, y, z)-space. This is done by exporting the field distribution from the CST MWS simulation, and performing the inverse transformation by an additional MATLAB® script.

3.4   Freeform waveguide simulations, fabrication and experimental benchmarking

To verify our TO approach, we apply it to a series of freeform waveguide structures that connect two silicon photonic waveguides, see Fig. 3.3(a). We calculate the transmission of these structures at a wavelength of $\lambda = 1550$ nm using the TO concept with CST MWS as a FIT time-domain solver for the waveguide in the virtual (u, v, s)-space, and we compare the results to a full simulation of the original structure in (x, y, z)-space. Moreover, we experimentally realized and characterized the structures, and we calculated the transmission with our previously reported fundamental mode approximation (FMA) method [56]. The FMA is based on a look-up table of pre-calculated eigenmodes (propagation constants and modal field distributions) of waveguide segments with constant radii of curvature, on their tabulated bending losses and on transition losses due to modal field mismatch between two adjacent segments with different radii of curvature. The FMA subdivides FOW in segments with constant radii of curvature and calculates the transmission losses based on the look-up table. While exceptionally fast (optimization times of the order of ms with pre-calculation done), this method disregards the existence of higher-order modes. Figure 3.3 shows the experimental setup, some freeform waveguide illustrations, scanning electron microscopy (SEM) pictures of the fabricated structures, as well as a comparison of the simulated and measured transmission for different waveguide trajectories, that are described by the height h of the apex above the substrate.

For the experimental benchmark, the freeform waveguides were 3D-printed on a SiP chip that was fabricated through a commercial foundry using standard CMOS process and 248 nm deep-UV lithography. The waveguides are normally covered by a SiO_2 top cladding layer, which was removed to make the SiP waveguides accessible to the 3D printing system. For fabrication of the 3D freeform waveguides, a negative-tone photoresist is deposited on the chip and structures are then 3D-printed by two-photon polymerization [106]. Subsequently, the unexposed resist is
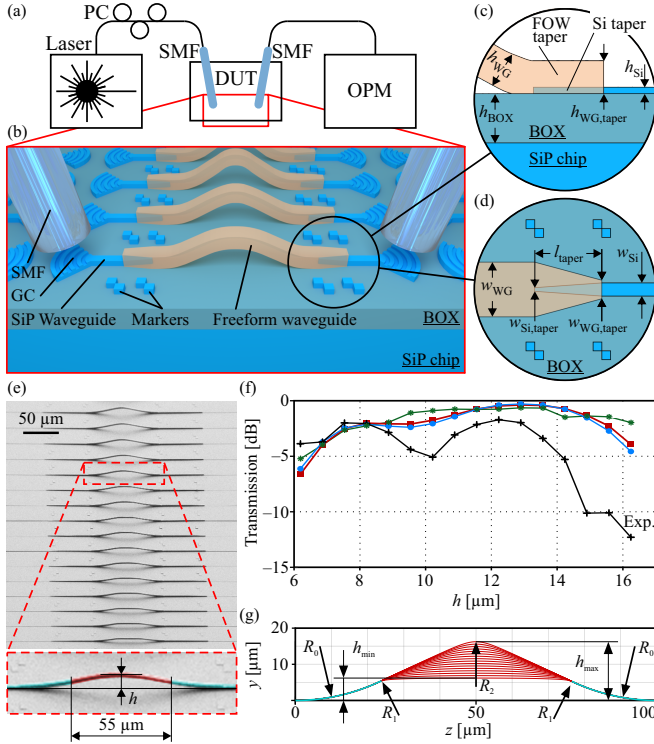
Figure 3.3: Benchmarking of the TO approach with respect to different simulation techniques and measurements. (a) Experimental setup: Continuous wave (CW) light emitted by a laser source at a wavelength of $\lambda = 1550$ nm is launched to test structures consisting of 3D freeform waveguides that are connected to on-chip access waveguides. The light is coupled to the chip by single-mode fibers (SMF) and grating couplers. The power of the transmitted signal is measured by an optical power meter (OPM). The 3D freeform waveguides feature trajectories, leading to different apex heights h. (b) Artist's impression of the test structures on silicon photonic (SiP) chip: Light from an SMF enters a freeform waveguide via a grating coupler (GC) and an SiP waveguide. (c) Side view and (d) top view of the tapered transition between a freeform waveguide and an SiP waveguide. (e) Scanning electron microscopy (SEM) image of a series of freeform waveguides fabricated on an SiP chip. The apex height $h_{min} \leq h \leq h_{max}$ of the trajectory is swept between $h_{min} = 6.2$ μm and $h_{max} = 16.2$ μm. Bottom inset: Close-up of a freeform waveguide. The central part is 55 μm long (red) and has a variable apex height h. Coupling and the adjacent sections (blue) are kept the same for all freeform waveguides. (f) Simulated and measured freeform waveguide transmission vs. its trajectory height h. Methods: TO transformation optics, FMA fundamental mode approximation, Ref. reference simulation in original space, Exp. experimental. (g) Freeform waveguide trajectories with indicated various curvature radii.

41

removed in a separate development step, and the freeform waveguides are covered by a low-index polymer (not shown in Fig. 3.3) that serves as a cladding and a protection against environmental influences. The refractive index of the freeform waveguide core at $\lambda = 1550\,\text{nm}$ amounts to $n_{\text{core}} \approx 1.53$, and the cladding refractive index is $n_{\text{cladding}} \approx 1.36$. Both materials are assumed to be lossless dielectrics (relative magnetic permeability $\mu_r = 1$ in the original (x, y, z)-space), and the corresponding values of the dielectric permittivity are calculated by squaring the refractive indices. Each freeform waveguide has a $w_{\text{WG}} \times h_{\text{WG}} = 2\,\mu\text{m} \times 1.8\,\mu\text{m}$ rectangular cross-section and bridges a $l_{\text{g}} = 100\,\mu\text{m}$ gap between a pair of SiP strip waveguides (width $w_{\text{Si}} = 500\,\text{nm}$, height $h_{\text{Si}} = 220\,\text{nm}$) that lie on a buried oxide (BOX) SiO_2 layer with a height of $h_{\text{BOX}} = 3\,\mu\text{m}$. Each SiP waveguide is connected to a grating coupler (GC) on one side and to a freeform waveguide on the other side. The connections between SiP waveguides and freeform waveguides are made through linear inverse tapers with a length of $l_{\text{taper}} = 60\,\mu\text{m}$ on both connected waveguides. The chosen length ensures an adiabatic transition between the different modes fields in the two waveguides and thus improves the coupling (see Fig. 3.3(b)–(d)). On the SiP waveguide side, the linear taper converts the initial $w_{\text{Si}} \times h_{\text{Si}} = 500\,\text{nm} \times 220\,\text{nm}$ cross section to a $w_{\text{Si,taper}} \times h_{\text{Si}} = 130\,\text{nm} \times 220\,\text{nm}$ cross section at the taper tip, see Fig. 3.3(c) and (d). On the freeform waveguide side, the initial $w_{\text{WG}} \times h_{\text{WG}} = 2\,\mu\text{m} \times 1.8\,\mu\text{m}$ cross section is linearly tapered to a $w_{\text{WG,taper}} \times h_{\text{WG,taper}} = 0.76\,\mu\text{m} \times 1.8\,\mu\text{m}$ cross section. All freeform waveguide trajectories are plane curves with an apex height h swept between $h_{\text{min}} = 6.2\,\mu\text{m}$ and $h_{\text{max}} = 16.2\,\mu\text{m}$ with a step of about $670\,\text{nm}$. For these experiments, we designed the beginning and the ending of each freeform waveguide trajectory (length of $22.5\,\mu\text{m}$ on each side) as a circular arc, bending upwards with a radius of $R_0 = 55\,\mu\text{m}$, while the central freeform waveguide trajectory part ($55\,\mu\text{m}$ length) is variable, generated by a parameterized B-spline, see Fig. 3.3(e) and (g). For small values of h, there are two sharp bends with radius R_1 at the two connections between the central freeform waveguide section and the two parts with the constant bend radius, see Fig. 3.3(g). This bend radius R_1 becomes larger with increasing height h, such that the loss contribution of these bends decreases. For large values

of h, there is a sharp bend with a radius R_2 at the trajectory apex, which again increases the overall loss. It is therefore expected that the transmission increases with h near $h_{\min}$ and decreases with h near $h_{\max}$, with a maximum between the two extreme values of h.

The experimental setup is illustrated in Figs. 3.3(a)–(d). To measure the transmission loss of a 3D printed freeform waveguide, continuous-wave (CW) light from a laser source at a vacuum wavelength of $\lambda = 1550$ nm is launched to the SiP input waveguides through a standard single-mode fiber (SMF) and a GC, Fig. 3.3(b). The light propagates through the 3D-printed freeform waveguide, and is finally coupled out through another SiP waveguide and probed by another SMF through the corresponding GC. The transmitted optical power is measured by an optical power meter (OPM). In order to exclude the coupling losses between the chip and the fibers, we measure the transmission loss of a reference structure (not shown) comprising two GC connected by a short SiP waveguide, and we refer all other transmission measurements to this value. The corresponding result is plotted on a logarithmic scale in Fig. 3.3(f) (marked Exp., black). The small variations in transmissions for adjacent heights demonstrate the precision of the 3D printing system and the reproducibility of the overall fabrication process. Note that the cross section of 3D-printed freeform waveguide ($2\,\mu m \times 1.8\,\mu m$) in combination with the index difference between the core ($n_{\text{core}} \approx 1.53$) and the cladding ($n_{\text{cladding}} \approx 1.36$) permits propagation not only of the fundamental mode, but also some higher-order modes. The local transmission minimum at an apex height of $h \approx 10\,\mu m$, see Fig. 3.3(f), stems from the excitation of higher-order modes in the 3D freeform waveguide and from the resulting multimode interference at the transition to the single-mode SiP waveguide, see also Fig. 3.4.

We then simulate the freeform waveguide transmission losses with the FIT time domain solver of CST MWS using the TO approach (in the virtual (u, v, s)-space as described in Section 3.3), and with the conventional approach (in the original (x, y, z)-space) as a reference. We set up the ranges of u and v as $u \in [-2.5\,\mu m, 2.5\,\mu m]$ and $v \in [-4\,\mu m, 4\,\mu m]$ in the TO-based simulations, while
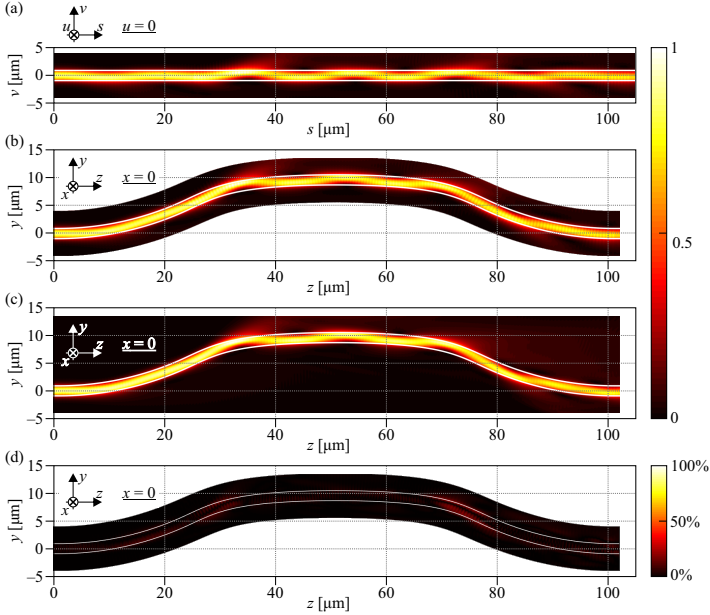
Figure 3.4: Simulated normalized magnitude $|\underline{\mathbf{E}}|$ of the complex electric-field vectors $\underline{\mathbf{E}}$ for the freeform waveguide with $h = 9.54\,\mu\text{m}$. The complex electric field $\underline{\mathbf{E}}$ is obtained from the time-domain simulation results through a Fourier transform at the target frequency, corresponding to a vacuum wavelength of $\lambda = 1550\,\text{nm}$. We compare results in the virtual (u, v, s)-space and in the original (x, y, z)-space for a TE polarized light, having a dominant electric-field oriented along x in (x, y, z)-space and along u in (u, v, s)-space. The freeform waveguide has a plane trajectory in the (y, z)-plane $(x = 0)$. The white contour lines in (a)–(d) are added for a better visualization of the freeform waveguide core. **(a)** Field distribution in (u, v, s)-space in plane $u = 0$, which corresponds to plane $x = 0$ in (x, y, z)-space. The freeform waveguide in (u, v, s)-space is straight, which enables a minimum-size rectangular computational volume. **(b)** Field distribution in (x, y, z)-space in the plane $x = 0$ obtained by applying the inverse space transformation $f^{-1}(u, v, s) = (x, y, z)$ to the distribution shown in (a). **(c)** Field distribution in (x, y, z)-space in plane $x = 0$, as obtained from a direct simulation in (x, y, z)-space. The rectangular simulation volume in (x, y, z)-space is not optimal since it encompasses much space far away from the freeform waveguide, where the field is close to zero. The field distribution shows a good match to the distribution from (b). **(d)** Relative deviation between the field distributions obtained from the TO simulation in (b) and the direct simulation in (c), obtained by calculating the magnitude of the difference of the respective electric-field magnitudes and by normalizing it to the maximum of the field found for the direct simulation. Referring to Fig. 3.3(f) and the field in (a)–(c), we see that a multimode interference could explain the experimentally observed minimum transmission for apex heights around $10\,\mu\text{m}$.

in the reference simulations these ranges correspond to $x \in [-2.5\,\mu\text{m}, 2.5\,\mu\text{m}]$ and $y \in [-4\,\mu\text{m}, h+4\,\mu\text{m}]$. Since we are predominantly interested in the impact of the waveguide trajectory on the transmission behaviour, these simulations do not take into account the coupling of the SiP waveguide to the 3D-printed freeform waveguide as detailed in Fig. 3.3(c). Instead, we assume to freeform waveguide to be embedded into a homogeneous cladding material, and we cut it at the end of linear taper of the SiP waveguide, as indicated by a dotted red line in Fig. 3.3(c). The tapered structure to the right of this line is then replaced by a straight waveguide section of length $l_\text{s} = 1\,\mu\text{m-long}$, in which we define the ports for the CST MWS simulation. Since a straight waveguide in (x, y, z)-space maps to an identical straight waveguide in (u, v, s)-space without any change of material properties, the modes of the straight waveguides in both spaces are identical. The length of the computational domain in the virtual (u, v, s)-space is thus $s_\text{tot} + 2l_\text{s}$, where s_tot denotes the total length of the freeform waveguide trajectory. For the simulation in the real (x, y, z)-space, we choose a computational domain of length it is only $(l_\text{g} + 2l_\text{s})$. All simulations were done with the same settings and on the same simulation machine. The discretization of the freeform waveguide into bricks for performing the TO simulations was done as explained in Section 3.3, with 28 bricks per slice as illustrated in Fig. 3.2. The total number of bricks for different freeform waveguides ranges from 1 288 to 3 080. We also simulate the transmission losses using the FMA method [56], which subdivides the waveguide into sections of constant curvature and calculates the transmission losses based on the propagation of the fundamental modes in these waveguide segments. TO-simulated transmission values in Fig. 3.3(f) are displayed in red, the results of the reference simulations by the conventional approach are displayed in blue, and the values obtained by the FMA algorithm are displayed in green. The curves obtained by TO and the reference simulations are nearly identical, with minimal differences that can be explained by the discretization of the freeform waveguide model into finite bricks with constant material properties. Both curves, similarly to the experimentally obtained curve, exhibit a local minimum near $h = 10\,\mu\text{m}$, and agree qualitatively very well with the measurement. The deviations

45

between measurements and simulations can be explained by the fact that the latter do not account for the coupling of the SiP waveguide to the 3D-printed freeform waveguide as detailed in Fig. 3(c). In addition, the higher measured transmission for $h \approx 6\,\mu m$ can be explained by a possible shrinking of the freeform waveguides during the development process, which smoothens the two sharp bends designed to have a curvature radius $R_1 \approx 4.3\,\mu m$, at the connections of the center freeform waveguide section to the initial and the final sections having a constant bend radius $R_0 = 55\,\mu m$, see Fig 3.3(f). The transmission obtained by the FMA method, does not show this local minimum. This is because the FMA method only considers the fundamental mode and disregards possible excitation of higher-order modes, such that it cannot take into account any multi-mode interference effects. Still, the optimum configurations with the least losses around a height of $13\,\mu m$ are well reproduced. Within certain limits, the FMA can therefore be used for a real-time trajectory optimization, which is important for, e. g., photonic wire bonds [12, 13, 34, 88] or waveguide overpass fabrication [87] in an industrial setting.

For comparing the electric-field distribution obtained by the TO and by the conventional approach, we plot the magnitude of the complex electric-field vectors in the plane $u = 0$ of the virtual (u, v, s)-space, Fig. 3.4(a), and in the corresponding plane $x = 0$ of the real (x, y, z)-space after back-transformation, Fig. 3.4(b). The apex height of the depicted waveguide amounts to $h = 9.54\,\mu m$, which corresponds to the local minimum of the simulated transmission as a consequence of multi-mode excitation. Figure 3.4(c) depicts the results of a direct CST MWS simulation in (x, y, z)-space, and Figure 3.4(d) displays the magnitude of the relative deviation between the field distributions obtained from the TO simulation, Fig. 3.4(b) and the direct simulation, Fig. 3.4(c), normalized to the maximum of the field found for the direct simulation. It can be seen that the two field distributions match well, with a maximum difference of 22.6 %. The biggest differences occur in the regions with a small bend radius — these differences are contributed to the discretization of the waveguide into bricks in the transformed space, see Section 3.3.

From the field plots shown in Fig. 3.4(a)–(c), we can can confirm the notion that

the dip in transmission of apex heights of approximately $10\,\mu m$, see Fig. 3(f), is caused by excitation of higher-order modes and by the resulting multi-mode interference.
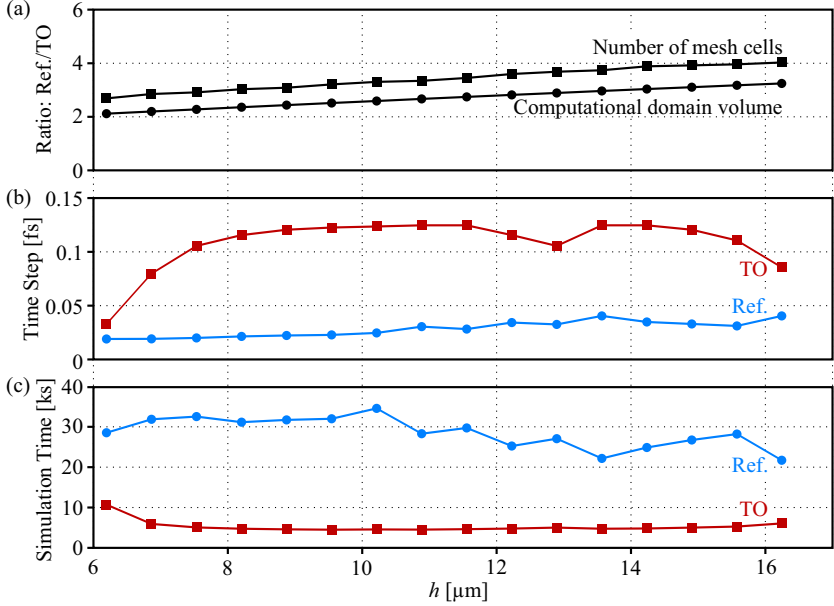

Figure 3.5: Simulations of freeform waveguides with different apex heights h of the trajectories. Comparison of number of mesh cells, computational volume, time steps and simulation times for the direct reference simulation in (x, y, z)-space (Ref.) and the TO simulation (TO). (a) Mesh cells (ratio mesh) and computational domain volumes (ratio compvol.) of the reference simulation related to the corresponding values for the TO simulation. Both curves follow a (nearly) straight line when h and therefore the computational volume is linearly increased. (b) Comparison of time steps, determined by the smallest mesh cell size and by the material properties. The smaller mesh cells in reference simulations needed to represent fine features cause smaller time steps. Large differences in TO-based simulations originate from different material properties. In case of freeform waveguides with sharp bends the tensors of material properties in the virtual (u, v, s)-space have entries with values close to zero, which cause a large maximum phase velocity in the TO-based model – see Appendix A.3. (c) Comparison of total simulation times. Both different numbers of mesh cells (different computational domain volumes) and different time steps contribute to different simulation times.

3.5 Computational complexity

To quantify the advantages of the TO approach, we compare the associated computational effort to that of the conventional approach. The results are displayed in Fig 3.5. Figure 3.5(a) shows the ratios of the volumes of the computational domains for different apex heights h of the freeform waveguide, see Fig. 3.3(b), as well as ratio of the numbers of mesh cells. Both ratios indicate a reduction of the computational effort by more than a factor of two when using the TO technique. This ratio increases nearly linearly with the apex height h, because the computational volume of the conventional approach increases more strongly with h than the one of the TO approach. Note that, for the TO-based simulations, the volume depends predominantly on the total arc length s_{tot} of the freeform waveguide, which increases only slightly with h as long as $h \ll s_{\text{tot}}$. The ratio of the number of mesh cells for the reference simulation and the TO-simulation follows about the same proportionality as the ratio of the volumes of the computational domains.

Another parameter that influences the total simulation time is the *time step* used in the FIT simulation, for which the Courant-Friedrichs-Lewy stability criterion for solving partial differential equations [96, 107] dictates an upper limit,

$$\Delta t_{xyz} \leq \left(c_{xyz} \sqrt{\frac{1}{\Delta x^2} + \frac{1}{\Delta y^2} + \frac{1}{\Delta z^2}} \right)^{-1}, \quad \Delta t_{uvs} \leq \left(c_{uvs} \sqrt{\frac{1}{\Delta u^2} + \frac{1}{\Delta v^2} + \frac{1}{\Delta s^2}} \right)^{-1}.$$

$$(3.7)$$

In these relations, Δt_{xyz} is the maximal time step and c_{xyz} the maximum phase velocity in any direction in (x, y, z)-space, which is discretized by spatial step sizes Δx, Δy, and Δz. For the TO approach, Δt_{uvs}, c_{uvs} and Δu, Δv, Δs are the equivalent quantities in (u, v, s)-space. Since Eq. (3.7) must hold for all mesh cells in the computational domain, the maximum time step is eventually dictated by the smallest mesh cell. In this context, the TO technique offers the additional advantage that the geometrically straight waveguide in the transformed (u, v, s)-space can be well represented by a rather simple rectilinear grid. In

contrast to that, correct representation of the surfaces of the freeform waveguide in the original (x, y, z)-space may require local refinements of the mesh sizes Δx, Δy, and Δz, and thus leads to smaller time steps according to Eq. (3.7). For most cases of practical interest, this advantage of the TO approach overcompensates the impact of the transformed material tensors, see Fig. 3.5(b). Note, however, that the transformed material tensors μ' and ϵ' in (u, v, s)-space can have elements with values close to zero, which strongly increases the associated maximum phase velocity c_{uvs} and thus reduces the maximum permitted time step Δt_{uvs} in the TO simulation. This effect occurs, e.g., towards the inner sides of strong waveguide bends, where the boundary of the computational domain may be close to a local center of curvature; see Appendix C for details. This effect can be indirectly observed from Fig. 3.5(b), where the shortest time step was required for the freeform waveguide with the smallest height and thus the smallest radius of curvature $R_1 \approx 4.3\,\mu m$ at the transitions between the fixed and the variable part of the trajectory, see Fig. 3.3(g). In this simulation, the range of v-coordinates in all simulations was $v \in [-4\,\mu m, 4\,\mu m]$, and the boundary of the computational domain was thus just $0.3\,\mu m$ away from the center of curvature associated with the most strongly curved waveguide section. This effect could be mitigated by limiting the values of the entries of the tensors to a chosen lower bound, which will not have significant impact on the simulation results — the field is always dragged to the outer side of the bend such that the magnitude at the inner side is small. Finally, we compare the total simulation times for the TO approach and the reference simulation, see Fig. 3.5(c). Both results are influenced by the total number of mesh cells and the time step. In all cases, the TO-based simulations were completed significantly faster than the conventional reference simulations. It should be mentioned that the additional computational overhead of the TO-based simulations, given by the time necessary to discretize the freeform waveguides into bricks, to calculate the material properties, to generate the required CST scripts, and to perform the spatial back transform after the simulation, was around $100\,s$, which is negligible compared to the total simulation time of several thousand seconds and was therefore not included in the results shown in Fig. 3.5(c). Overall, for the

structures simulated here, the TO approach is 3–6 times more efficient than the conventional simulation, with significant potential for further improvement. The

waveguide trajectories in the presented examples are still rather simple, consisting of plane curves in the (y, z)-plane that start and end at the same height in y. For waveguides with non-plane trajectories, see, e.g., Fig. 3.1, the reduction of the computational volume through the TO approach will be even more pronounced, but the numerical treatment also becomes more complicated. Specifically, for plane waveguide trajectories, the tensors $\boldsymbol{\varepsilon}'$ and $\boldsymbol{\mu}'$ maintain their diagonal shape in (u, v, s)-space, see Appendix B, while waveguides with non-plane trajectories require the consideration of off-diagonal elements in the transformed material tensors $\boldsymbol{\varepsilon}'$ and $\boldsymbol{\mu}'$. For commonly used leap-frog schemes, the FDTD update equations for the electric and the magnetic field in generally anisotropic media can be written as

$$
\begin{aligned}
\underline{\mathbf{H}}'(t_{n+1}) &= \underline{\mathbf{H}}'(t_n) - \Delta t \cdot (\boldsymbol{\mu}'(u, v, s))^{-1} \cdot \left(\underline{\mathbf{E}}'(t_n)\right), \\
\underline{\mathbf{E}}'(t_{n+1}) &= \underline{\mathbf{E}}'(t_n) + \Delta t \cdot (\boldsymbol{\varepsilon}'(u, v, s))^{-1} \cdot \left(\underline{\mathbf{H}}'(t_n)\right).
\end{aligned}
\tag{3.8}
$$

In this relation, t_n and t_{n+1}, $n = 0, 1, 2, ...$, denote the staggered discrete time steps at which the electric and the magnetic field are calculated by the leapfrog scheme. For isotropic materials or media with diagonal $\boldsymbol{\varepsilon}'$- and $\boldsymbol{\mu}'$-tensors in (u, v, s)-space, the evaluation of each of these constitutive relations simply involves multiplication of a (3,1)-vector with a scalar. Taking into account off-diagonal elements would require a multiplication of a (3,3)-matrix with a (3,1)-vector and thus increase the computational effort for the evaluation of each constitutive relation by approximately a factor of three, considering only the number of multiplications. In addition, FDTD modeling of materials with non-diagonal $\boldsymbol{\varepsilon}'$ and $\boldsymbol{\mu}'$-tensors is complicated by the coupling of non-parallel components of $\underline{\mathbf{H}}'$ and $\underline{\mathbf{E}}'$ and of $\underline{\mathbf{E}}'$ and $\underline{\mathbf{H}}'$, which are not collocated on the standard Yee grid [108]. Numerical modeling of such materials thus requires spatial interpolation [108, 109], or alternative approaches based on Lebedev grids [110, 111]. Still, the TO approach should

offer significant performance advantages also for non-plane trajectories, for which an even more significant reduction of the computational volume can be expected.

Note that the simulations shown in the previous sections refer to waveguides with rectangular cross sections that are invariant along the waveguide trajectory, which can be accurately represented by a rather simple rectilinear grid. In case of arbitrary cross sections that vary along the waveguide trajectory, this advantage of the TO approach might be maintained by adapting the transformation to not only map the curve trajectory into a straight one, but to also map an arbitrary waveguide cross section into a rectangular one [112] that is invariant along the propagation direction.

3.6 Summary

We introduced a transformation optics (TO) based concept for simulating freeform optical waveguides applicable to commercially available time-domain Maxwell's equations solvers. The method reduces the freeform waveguide simulation volume by transforming the freeform waveguide into a number of connected rectangular boxes through a spatial transformation that is related to the local coordinate system of the freeform waveguide trajectory. The price to pay is that fictitious material properties in the transformed space have to be calculated. Our time-domain simulations of freeform waveguides with plane trajectories show a significant reduction in the simulation time compared to a conventional approach, while the simulation results agree very well with the outcome of conventional simulators. For benchmarking our TO concept experimentally, we realized a series of freeform waveguides and measured their transmission losses. The measured and the simulated results show a very good qualitative agreement. We believe that our approach has the potential to facilitate the design and the prototyping of waveguide-based optical devices.

[end of the content based on the main part of manuscript [J1]]

4 Photonic-integrated circuits with non-planar topologies realized by 3D-printed waveguide overpasses

This chapter reports on 3D-printed waveguide ovepasses on a silicon photonic integrated circuit, that may overcome the challenges of highly non-planar PIC with a large number of waveguide crossings. The chapter was taken from publication [J3], and the format of the publication was adapted to fit the structure of this thesis. Supplementary information related to this chapter can be found in Appendix B, which is also taken from the publication [J3].

The scope of this publication was developed by the author of the thesis together with C. Koos. The graph-theoretical analysis described in this chapter and in Appendix B was developed by the author, supervised by C. Koos and verified by M. Nöllenburg. The photonic integrated circuit design was done by the author and supervised and verified by M. Lauermann. M. Blaicher and T. Hoose fabricated 3D printed waveguide overpasses, and A. Hofmann and Y. Kutuvantavida applied selective overcladding to the fabricated waveguide overpasses. The experiments were conceived by the author and C. Koos. The author conducted the experiments and analyzed experimental results. All figures were composed and the publication was written by the author, supported by W. Freude and C. Koos. The work was jointly supervised by S. Randel, W. Freude, and C. Koos.

[start of publication [J3]]

Photonic-integrated circuits with non-planar topologies realized by 3D-printed waveguide overpasses

Aleksandar Nesic,[1,6] Matthias Blaicher,[1,2] Tobias Hoose,[1,2] Andreas Hofmann,[3] Matthias Lauermann,[1,4] Yasar Kutuvantavida,[1,2] Martin Nöllenburg,[5] Sebastian Randel,[1] Wolfgang Freude,[1] and Christian Koos[1,2,4,*]

[1]*Karlsruhe Institute of Technology (KIT), Institute of Photonics and Quantum Electronics (IPQ), Engesserstrasse 5, 76131 Karlsruhe, Germany*
[2]*Karlsruhe Institute of Technology (KIT), Institute of Microstructure Technology (IMT), Hermann-von-Helmholz-Platz 1, 76344 Eggenstein-Leopoldshafen, Germany*
[3]*Karlsruhe Institute of Technology (KIT), Institute of Automation and Applied Informatics (IAI), Hermann-von-Helmholz-Platz 1, 76344 Eggenstein-Leopoldshafen, Germany*
[4]*Vanguard Photonics GmbH, Gablonzer Strasse 10, 76185 Karlsruhe, Germany*
[5]*TU Wien, Institute of Logic and Computation, Algorithms and Complexity Group, Favoritenstrasse 9–11, 1040 Vienna, Austria*

Complex photonic-integrated circuits (PIC) may have strongly non-planar topologies that require waveguide crossings (WGX) when realized in single-layer integration platforms. The number of WGX increases rapidly with the complexity of the circuit, in particular when it comes to highly interconnected optical switch topologies. Here, we present a concept for WGX-free PIC that relies on 3D-printed freeform waveguide overpasses (WOP). We experimentally demonstrate the viability of our approach using the example of a 4×4 switch-and-select (SAS) circuit

realized on the silicon photonic platform. We further present a comprehensive graph-theoretical analysis of different $n \times n$ SAS circuit topologies. We find that for increasing port counts n of the SAS circuit, the number of WGX increases with n^4, whereas the number of WOP increases only in proportion to n^2.

4.1 Introduction

Photonic integrated circuits (PIC) are becoming increasingly complex, incorporating thousands of photonic devices on a single chip [16, 84]. The silicon photonic (SiP) platform, in particular, stands out to high integration density and offers high-yield fabrication on large-area substrates using mature CMOS processes [113, 114]. However, as the complexity of PIC increases, non-planar circuit topologies with hundreds or even thousands of waveguide crossings (WGX) are unavoidable, and the number of WGX often increases in a strongly nonlinear way with the complexity of the circuit. As a consequence, compact WGX have evolved into key building blocks, and substantial research effort has been dedicated to optimizing their performance. This has led to remarkably low insertion loss (IL) of $0.017\,\mathrm{dB}$ and crosstalk as small as $-55\,\mathrm{dB}$ at $\lambda = 1550\,\mathrm{nm}$, demonstrated for partially etched multi-mode interference (MMI) structures that feature a relatively large footprint of approximately $30 \times 30\,\mathrm{\mu m}^2$ [16]. Fully etched MMI structures allow to reduce the footprint to, e.g., $9 \times 9\,\mathrm{\mu m}^2$, but losses and crosstalk increase to, e.g., $0.028\,\mathrm{dB}$ and $-37\,\mathrm{dB}$, respectively [14]. Arrays of WGX can be compactly realized by exploiting Bloch modes in multi-mode waveguides: For SiP structures fabricated by electron-beam lithography, values of $\mathrm{IL} = 0.019\,\mathrm{dB}$ and crosstalk of less than $-40\,\mathrm{dB}$ per WGX were demonstrated for a 101×101 WGX array with a $3\,\mathrm{\mu m}$ waveguide pitch [15]. For optical lithography, the best reported values for Bloch mode WGX are $\mathrm{IL} = 0.04\,\mathrm{dB}$ and crosstalk less than $-35\,\mathrm{dB}$ for a 1×10 array of crossings with a $3.25\,\mathrm{\mu m}$ waveguide pitch [115].

However, while these demonstrations are impressive, even IL of the order of a few hundredths of dB and crosstalk of the order of $-40\,\mathrm{dB}$ per WGX may have

a substantial impact on the performance of large-scale PIC that may comprise tens of thousands of crossings. A prime example in this context are high-radix switches that rely on the so-called switch-and-select (SAS) architecture [17]. The SAS scheme offers low crosstalk and simple control but requires a complex and highly non-planar interconnect network that provides a dedicated waveguide from each input to each output port. In fact, finding a layout that gives the minimum number $\eta_{n,n}$ of WGX in an $n \times n$ SAS circuit, and generally in any circuit, is an NP-complete problem [116], and $\eta_{n,n}$ scales with $n^4/16$ according to a still unproven conjecture [65, 66]. This leads to tens of thousands of WGX for $n = 32$ and to approximately one million WGX for $n = 64$. To illustrate the associated performance penalty by WGX crosstalk, let us consider an example of a waveguide that crosses an array of 100 other waveguides with a crosstalk of -40 dB in each of the crossings. Assuming incoherent superposition of the various crosstalk contributions and interpreting them as random noise that deteriorates the signal, the signal-to-noise power ratio (SNR) would amount to 20 dB. For a 32QAM signals, this would lead to a bit-error ratio (BER) of 6×10^{-4} [117], which is only slightly below the 4.5×10^{-3} limit for hard-decision forward-error correction (HD-FEC) with 7% overhead [118]. This represents a significant deterioration of the signal quality. For 64QAM, which is envisaged for high-speed transmission systems with data rates beyond 500 Gbit/s per wavelength, an SNR of 20 dB would even be insuffcient to reach the HD-FEC limit. Such crosstalk levels hence represent a significant deterioration of the signal quality. The situation may become even worse in case the crosstalk signals are superimposed coherently. Moreover, a few hundredths dB of IL per WGX would result in several dB of overall IL that is accumulated over the 100 crossings. This example illustrates that large-scale PIC with highly non-planar topologies may face performance limitations when realized by WGX in single-layer integration platforms.

To overcome the limitations of conventional WGX, multi-layer PIC have been proposed exploiting multiple stacked waveguide layers, realized from silicon [119, 120], silicon nitride (Si_3N_4) [121, 122] or as a combination of both waveguide

technologies [123–128]. The deposition of the upper layers is typically done by chemical vapor deposition (CVD) and involves chemical mechanical planarization (CMP) of intermediate SiO_2 cladding layers that separate the waveguide layers. While simple two-layer implementations offer decent performance [125, 127], three-layer structures have been shown to greatly reduce inter-layer crosstalk while maintaining effcient interlayer coupling [120, 126, 128]. This allows to reduce the crosstalk to less than -56 dB with remarkably low interlayer coupling losses of less than 0.15 dB from the bottom to the top layer using a pair of vertical directional couplers of approximately $190\,\mu m$ length per side [126, 128]. However, while this approach offers utmost scalability and the ability to cross entire groups of waveguides, the integration of silicon or silicon nitride waveguides into back-end metal layer stacks introduces additional technological complexity and is not yet established as part of the technology portfolios offered by silicon photonic foundries. In addition, all multi-layer PIC demonstrations so far are limited to silicon photonics.

In this chapter we demonstrate hybrid 2D/3D photonic integration based on direct-write laser lithography as an alternative approach for realizing non-planar circuit topologies. Our approach is based on 3D-printed freeform polymer structures [129], which we refer to as optical waveguide overpasses (WOP). WOP are realized in situ by two-photon polymerization [106], which has previously been used for fabrication of so-called photonic wire bonds that enable low-loss single-mode connections across chip boundaries [11, 12, 34, 130]. The devices offer low crosstalk of less than -75 dB and allow to bridge series of parallel waveguides, thereby replacing a multitude of WGX. We demonstrate the viability of our approach by realizing a 4×4 SAS circuit. Based on a graph-theoretical analysis, we estimate that the number of WOP needed to realize a WGX-free $n \times n$ SAS PIC scales in proportion to $n^2/2$. A 64×64 SAS circuit would hence require only approximately 2000 WOP as opposed to the estimated one million conventional WGX. Fabrication of WOP may be effciently combined with 3D-printing for die-level packaging [11, 12, 34, 130], and offers the opportunity to locally incorporate

multi-layer elements into standard SiP circuits, fabricated through readily available foundry services. The concept of 3D-printed WOP is not limited only to silicon photonics but may be transferred to a wide range of alternative photonic integration platforms.

The paper is structured as follows: In Section 4.2 we introduce the concept of 3D-printed WOP. A graph-theoretical analysis of the number of necessary WOP and WGX for realizing surface-coupled $n \times n$ SAS devices is provided in Section 4.3. Design and experimental testing of the demonstrator device are explained in Section 4.4. Appendix A provides definitions of graph theory terms. Appendix B.2 gives further details of the graph-theoretical approach used for the analysis in Section 4.3. Appendix C gives a detailed graph-theoretical analysis of the number of necessary WOP and WGX for realizing facet-coupled SAS devices.
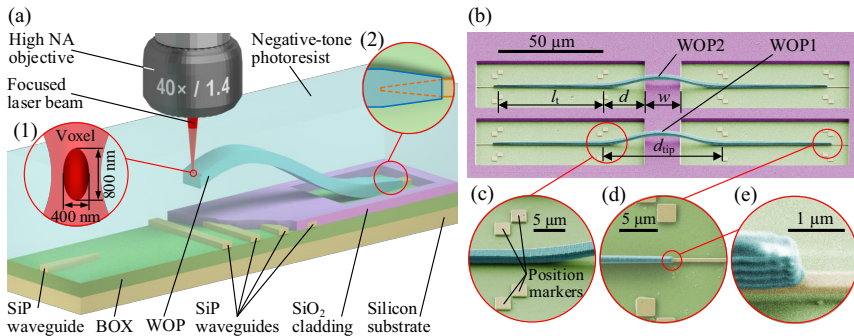

Figure 4.1: Concept and implementation of waveguide overpasses (WOP) on the silicon photonic (SiP) platform. (a) The WOP is written into a liquid negative-tone photoresist that is deposited onto the PIC. For better coupling to the SiP on-chip waveguides, the SiO$_2$ cladding is locally removed down to the buried oxide (BOX) layer. Inset (1): The spatial resolution of the two-photon lithography is determined by the size of the volumetric pixel (voxel) that results from two-photon polymerization. Inset (2): Tapers in the WOP and in the SiP waveguide improve the coupling effciency. (b) Scanning electron microscope (SEM) image of the WOP (colors were added by image processing). (c)–(e) Close-ups of different parts of the WOP. Position markers indicate the positions of the SiP waveguide ends that need to be interconnected. During fabrication of our chip, the SiO$_2$ cladding layer has been unintentionally over-etched, and part of the BOX has been unintentionally removed, see Subfigure (e).

4.2 Concept of waveguide overpasses (WOP)

The concept of a 3D-printed freeform optical WOP is illustrated in Fig. 4.1 for the example of a SiP circuit. The PIC may be fabricated through standard processes offered by a commercial SiP foundry, including selective removal of SiO_2 cladding layer to access the tapers of the SiP waveguides that need to be interconnected [131]. For fabrication of the WOP, a negative-tone photoresist is locally deposited onto the chip, and the WOP is then 3D-printed into the resist by direct laser writing based on two-photon polymerization. After exposure, the resist is removed, and the free-standing WOP structures are clad by a low-index polymer that acts as cladding and humidity protection (not shown in Fig. 4.1). Depending on the length, WOP may bridge tens or even hundreds of planar waveguides in the SiP device layer. Figure 4.1(b) displays scanning electron microscope (SEM) images of the two WOP on our demonstrator device before the cladding was applied, with colors added by image processing for better visualization. Figures 4.1(c)–4.1(e) show close-ups of different parts of the lower WOP and demonstrate the accuracy of the direct laser writing method. The two-photon lithography system uses CMOS patterned silicon markers for automated detection of the SiP waveguides that need to be interconnected. The 3D-printing time of one WOP is about $30\,\mathrm{s}$ with a significant potential for further reduction. The refractive index of the WOP core material amounts to $n_{\mathrm{WOP}} \approx 1.53$, and the cladding has a refractive index of $n_{\mathrm{cladding}} \approx 1.36$ at $1550\,\mathrm{nm}$. Note that the concept has been illustrated for the SiP platform here but can generally be applied to a wide range of PIC technologies. As an example, 3D-printed photonic wire bonds can be efficiently coupled to surface-coupled [34] and edge-coupled InP-waveguides [130].

4.3 Theoretical analysis of non-planar switch-and-select (SAS) circuit topologies

To experimentally demonstrate the viability of our approach, we use an $m \times n$ SAS circuit as an example of a PIC requiring many WGX. In the $m \times n$ SAS

architecture, each of the m input ports feeds a $1 \times n$ switch distributing the light to one of the n output ports, and each of the n output ports is fed by an $m \times 1$ switch, which selects light from one of the m input ports. An illustration of a basic non-optimized implementation of a 4×4 SAS architecture is shown in Fig. 4.2(a), featuring a total number of 36 WGX in the depicted case, which would scale up to a total number of

$$\eta_{n,n}^{\text{(basic)}} = \left(\frac{n\,(n-1)}{2} \right)^2 \tag{4.1}$$

for the case of an $n \times n$ SAS circuit. In the following, we show that these circuits can be realized with a significantly smaller number of WOP than the number of WGX, even if the layout of the circuit is optimized to reduce the number of WGX. To this end, we exploit graph theory to investigate the scaling of WGX and WOP number for increasing port counts n. For the remainder of this section, we consider the case where input and output ports are accessible from the top surface of the PIC and can hence be positioned anywhere on the chip. This case is referred to as *surface coupling*. Surface-coupled PIC may, e.g., rely on grating couplers, SiP waveguides that are bent upwards by ion implantation [30], or on 3D-printed lensed couplers [31]. We only give a summary of the results here; mathematical details can be found in Appendix B.2. In Appendix B.3, we also discuss the case of *facet coupling*, for which light is coupled to and from the PIC via waveguide facets along the chip boundary.

As a first step of the layout optimization, we exploit the fact that surface coupling allows to route waveguides around the couplers. This is illustrated in Fig. 4.2(b) for the example of a 4×4 SAS. In this implementation, we consider the $1 \times n$ and $m \times 1$ switches at the input and output ports as discrete entities that cannot be subdivided and that may hence be considered as lumped elements (LE). This leads to representation of the SAS circuit by a *complete bipartite graph $K_{m,n}$* having two sets M and N of m and n *vertices*, respectively. Each vertex of set M represents an input port of the SAS and its corresponding $1 \times n$ switch, and each vertex of set N represents an output port and the associated $m \times 1$ switch. Each vertex of
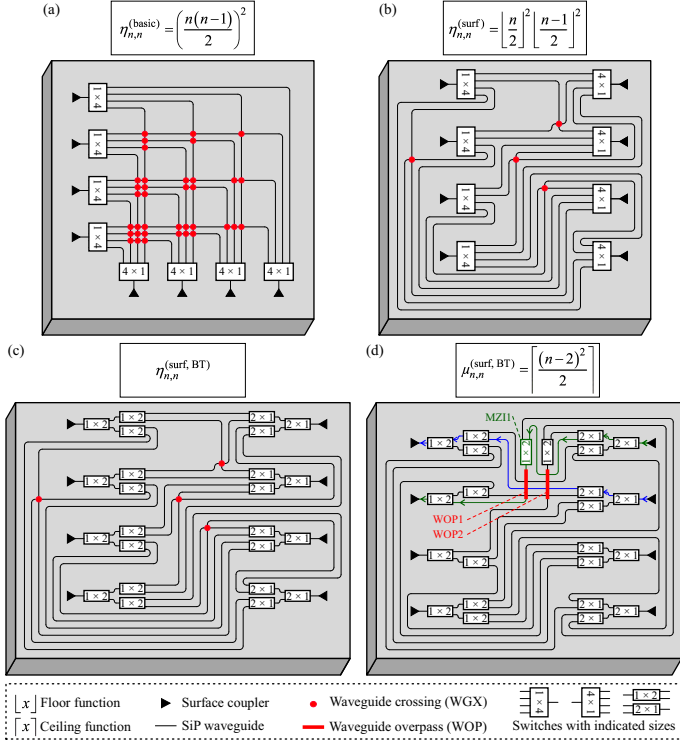
Figure 4.2: Comparison of layouts of a 4×4 optical switch-and-select (SAS) circuit for surface coupling. (a) Basic layout for single-layer waveguide technology without any optimization for reduced numbers of waveguide crossings (WGX). (b) Optimal layout for single-layer waveguide technology, minimizing the number of WGX by routing of waveguides around the coupling elements. The formula for $\eta_{n,n}^{(\mathrm{surf})}$ is a conjecture for the minimum possible number of WGX for an $n \times n$ SAS, if the $1 \times n$ and $n \times 1$ switches at the input and output ports are lumped elements (LE) [65, 66]. For large port counts n, the number of WGX is conjectured to scale with $n^4/16$. (c) Best found, but not necessarily optimal layout for a single-layer 4×4 SAS circuit, in which the 1×4 and 4×1 switches have been realized as binary trees (BT) of 1×2 and 2×1 switches. A general analysis of this circuit topology for arbitrary n is subject to ongoing investigations. (d) Best found, but not necessarily optimal WGX-free layout for hybrid 2D/3D circuits, minimizing the number of WOP. The switches are realized as BT in the same way as in (c). The formula for $\mu_{n,n}^{(\mathrm{surf,\ BT})}$ is an upper bound for the minimum number of WOP. The optical paths that were used for the crosstalk measurement in Section 4.4 are marked in green (Path 1) and in blue (Path 2). The arrows indicate the direction of light propagation for the crosstalk measurement. The drive current of MZI1 is modulated by a sinusoidal signal for highly sensitive lock-in detection of the weak crosstalk signals.

61

one set is connected to each vertex of the other set by a total of *mn edges* that represent optical waveguides. In the following, we restrict our consideration to the particularly relevant cases of $K_{n,n}$, for which the number *m* of input ports equals the number *n* of output ports. A generalization to the case of $K_{m,n}$ can be found in Appendix B.2.

For conventional SAS implementations in single-layer waveguide technology, a layout with the smallest possible number of WGX can be achieved by optimizing the drawing of the corresponding graph model for finding the minimum number of *edge crossings* (or just *crossings*), which is an NP-complete problem [116]. Up to now [65], there is only a conjectured formula for the minimum possible number of crossings (*crossing number*), based on a straightforward graph drawing algorithm, only proven to give an upper bound [66],

$$\eta_{n,n}^{(\text{surf})} = \left\lfloor \frac{n}{2} \right\rfloor^2 \left\lfloor \frac{n-1}{2} \right\rfloor^2 \tag{4.2}$$

In this relation, $\lfloor x \rfloor$ denotes the floor function. For large *n*, the conjectured crossing number scales with $n^4/16$, thereby reducing the number of WGX by a factor of 4 compared to the simplistic non-optimized waveguide routing shown in Fig. 4.2(a). Note that the best published result for the lower bound of the crossing number in complete bipartite graphs $K_{n,n}$ states that for large *n* the crossing number scales at least with $0.83 \cdot n^4/16 \approx n^4/19.28$ [132]. However, this is a theoretical result for the case of large *n*, which has not been supported by drawings of the corresponding graphs. In fact, for complete bipartite graphs, no drawings are known that lead to lower number of crossings than conjectured by Eq. (4.2). We therefore use the conjectured formula and its corresponding drawing as a basis for our analysis of the scaling of WGX for increasing port counts *n*. For an $n \times n$ SAS circuit with $n = 16$, this would lead to a total number of 3136 WGX.

Regarding hybrid 2D/3D SAS circuit implementations based on WOP, we again start from the complete bipartite graph $K_{n,n}$ and determine the number of WOP by subtracting the maximum number of edges that can be realized without crossings

(the number of edges in the *spanning maximum planar subgraph*) from the total number of edges. The total number of edges in $K_{n,n}$ is n^2, and $4n - 4$ edges can be realized without crossings [133]. The number of missing edges hence amounts to

$$\mu_{n,n}^{(\text{surf, BT})} = n^2 - (4n - 4) = (n - 2)^2 \tag{4.3}$$

and equals the number of WOP necessary to complete the SAS circuit, assuming that each WOP can cross an arbitrary number of planar waveguides, and that crossings of 3D WOP can be avoided, see Appendix B.2 for more details. Note that the length of a WOP is only limited by the write field size of the two-photon lithography system, which currently amounts to approximately $500\,\mu\text{m} \times 500\,\mu\text{m}$. In the future, these limitations may be overcome by high-precision stitching of structures that extend across several write fields. Using Eq. (4.3), we calculate a total number of 196 WOP for an SAS circuit with $n = 16$, which is considerably smaller than the corresponding number of WGX. A comparison of the scaling of WGX and WOP numbers for increasing port count n is given in the second and third column of Table 4.1.

Table 4.1: Quantitative comparison of surface-coupled $n \times n$ switch-and-select (SAS) circuit implementations based on WGX in single-layer circuits and on WOP in hybrid 2D/3D photonic integration. The total number of WGX increases approximately in proportion to $n^4/16$, whereas the number of WOP scales with n^2 for the case of lumped-element (LE) switches, and with $n^2/2$ in case the switches are decomposed into binary trees (BT) of 1×2 and 2×1 switches. The maximum number of WGX along any optical path increases approximately in proportion to $n^2/4$ for the case of LE switches, whereas the maximum number of WOP along any optical path amounts to 1 in both cases of LE and BT switches.

SAS ($n \times n$)	Total number			Maximum number along any optical path	
	WGX (LE)	WOP (LE)	WOP (BT)	WGX (LE)	WOP (LE & BT)
4×4	4	4	2	1	1
8×8	144	36	18	9	1
16×16	3 136	196	98	49	1
32×32	57 600	900	450	225	1
64×64	984 064	3 844	1 922	961	1

As a further step of the circuit layout optimization, we may split up the $1 \times n$ and the $n \times 1$ switches at the input and the output into binary trees (BT) of 1×2 and 2×1 switches, see Fig. 4.2(d). This allows to reduce the number of WOP to

$$\mu_{n,n}^{(\text{surf, BT})} = \left\lceil \frac{(n-2)^2}{2} \right\rceil, \tag{4.4}$$

see Appendix B.2 for an explanation. In the last relation, $\lceil x \rceil$ denotes the ceiling function. The associated WOP numbers for increasing port counts n are indicated in the fourth column of Table 4.1. Note that the same technique with BT switches may also be applied to the single-layer SAS circuit architecture as illustrated in Fig. 4.2(c). For $n = 4$, we could not find a layout that reduces the number of WGX as compared to the implementation with LE switches. Note that the SAS circuit with BT switches is not any more a complete bipartite graph $K_{n,n}$ — an analysis of such circuit topologies has recently been published in [64]. Note further that for increasing port counts n of the SAS circuit with LE switches, the number of WGX increases with $n^4/16$, whereas the number of WOP of the SAS circuit with BT switches increases only in proportion to $n^2/2$. As a consequence, the number of WOP in a 16×16 SAS circuit with BT switches is nearly two orders of magnitude smaller than the number of WGX with LE switches, and for a 64×64 SAS, the numbers differ by nearly four orders of magnitude, see Table 4.1.

Besides the total number of WGX or WOP in the circuit, the maximum number of such elements along any optical path through the circuit is an important figure of merit. For the single-layer implementation of the SAS circuit with LE switches, the biggest number of WGX along an optical path amounts to

$$\xi_{n,n}^{(\text{surf})} = \left(\left\lceil \frac{n}{2} \right\rceil - 1 \right)^2, \tag{4.5}$$

which scales with $n^2/4$ for large n, see Appendix B.2 for details. The corresponding numbers for increasing port counts n are given in the fifth column of Table 4.1. For an SAS circuit with $n = 16$, this leads to up to 49 WGX along a single optical

path. In contrast to that, the number of WOP can be kept to at most one along each path, see last column of Table 4.1.

Note that these discussions are independent of 3D-printed structures as a specific way to realize waveguide overpasses, and that the findings can be broadly applied to other kinds of overpasses, e.g., in multilayer circuits [120, 126, 128]. 3D-printed WOP are particularly attractive for use cases in which the number of devices and/or the number of WOP per device are limited, while ultra-low cross-talk and/or the inherent flexibility of 3D printing are important. In contrast to that, the technique might suffer from limited throughput when applied to very complex circuits with thousands of WOP required on a single chip. In this case, monolithically integrated multi-layer circuits [120, 126, 128], might offer better scalability.

4.4 Device design, fabrication and experimental characterization

To demonstrate the viability of the WOP concept, we realized a 4×4 SAS device, similar to the one illustrated in Fig. 4.2(d), featuring two WOP. The device was realized on a silicon-on-insulator (SOI) wafer having a 220 nm-thick device and a 2 μm-thick buried oxide layer. All waveguides are realized as oxide-covered strip waveguides with standard width of 500 nm. The SAS circuit consists of four 1×4 switches at the input and four 4×1 switches at the output. Each of the 1×4 switches is realized as a BT of three 1×2 switches, and the same technique is applied to the 4×1 switches. In general, for realizing a $1 \times n$ switch as a BT, we need $(n - 1)$ 1×2 switches, each of which consists of a Mach-Zehnder interferometer (MZI) comprising two multi-mode interference (MMI) couplers and a pair of thermal phase shifters in the MZI arms. In total, there are $2n(n - 1) = 24$ MZI and $24 \cdot 2 = 48$ phase shifters, leading to 48 signal pads and a common ground for the electrical control signals. Note that activating one of the two phase shifters of each MZI is suffcient for switching — the second phase shifter has only been implemented for better balancing of the MZI arms. We use surface coupling by

grating couplers (GC). One of the WOP bridges three, and the other bridges four SiP waveguides spaced by $3.5\,\mu m$, see Figs. 4.2(d) and 4.3(c). The footprint of a single WOP amounts to approximately $15 \times 160\,\mu m^2$, including two $50\,\mu m$-long tapers for coupling the WOP to the SiP waveguides. This is more than an order of magnitude smaller than previously demonstrated overpasses realized by direct laser inscription of low-index contrast 3D-waveguides into glass matrices [134].

For switching, each of the possible input-output connections can be established by activating four phase shifters: Two phase shifters at the BT at the input are used to switch to the targeted output, and another two phase shifters are needed at the BT at the output to select the input. For an $n \times n$ SAS circuit with $n = 4$, accessing the full set of $n! = 24$ switch states would require to operate one phase shifter in each of the 24 MZI. To establish a specific switch state, i.e., a specific set of connections between input and output ports, it is suffcient to simultaneously operate a maximum of $2n\lceil \log_2 n \rceil = 16$ phase shifters, while the remaining phase shifters along unused optical paths are idle. In the experiment, we use a multi-channel current source that we can flexibly connect to the 16 relevant pads out of the overall set of 48 phase shifters. The electrical connection to the chip is established through two multi-contact probe wedges (MCW), see Figs. 4.3(a) and 4.3(b), each one with 15 DC probes. For each of these wedges, twelve probes connect to the phase shifters, two probes are used for the common ground connection pads on the chip, and one probe is left idle. From the $n^2 = 16$ optical paths connecting the various inputs and outputs of the switch, four paths contain one of the two WOP, see Fig. 4.2(d).

To characterize the performance of our SAS PIC, we measured the transmission spectra of all 16 optical paths, see Fig. 4.3(d). To eliminate the fiber-chip coupling losses, we use a reference structure composed of two GC that are connected by a short on-chip waveguide. The GC are not optimized and show maximum transmission at a wavelength of $1560\,nm$ with a fiber-chip coupling loss of approximately $6.3\,dB$ per coupling interface. For each path, we measure the transmission as a function of wavelength, and we correct the data to eliminate the fiber-chip coupling losses. In Fig. 4.3(d), the transmission spectra of the 12 optical

paths without WOP is displayed in pale blue, and the bright blue trace corresponds to the average insertion loss of the 12 paths. At 1550 nm, the average on-chip loss of the paths without WOP amounts to approximately 7 dB and originates from 8 MMI splitters, 4 phase shifters and up to 6.2 mm of on-chip SiP waveguide for each optical path. Using optimized devices on the SiP platform, namely MZI with insertion loss of 0.33 dB [17], waveguides with propagation losses of 0.2 dB/mm, and waveguide lengths of up to only 3 mm, the losses can be reduced to below 2 dB. We also measure the remaining two sets of two paths, each set containing the same WOP — the results are depicted in pale red, and the average for each set is given by a bright red solid line. The insertion losses of the two WOP, indicated as **black** curves in Fig. 4.3(d), are extracted from the difference of the bright blue and the two bright red curves by additionally taking into account the different lengths of the on-chip SiP waveguides along the various optical paths. At a wavelength of 1550 nm, we measured insertion losses of 1.6 dB and 1.9 dB for the two WOP. These comparatively high losses are mainly caused by a non-optimum design of the on-chip coupling structures for the WOP and may be reduced to well below 1 dB by optimizing the design of the PIC and of the freeform WOP. This expectation is supported by [34], in which 3D-printed waveguides with a minimum curvature radius of 40 μm and with losses of (0.4 ± 0.3) dB have been demonstrated. These numbers are comparable to the loss of 0.3 dB that has been reported for a three-layer evanescently coupled photonic circuit overpass [126, 128]. Note that surface roughness of the 3D-printed WOP, visible in Figs. 4.1(c) and 4.1(e), has only minor impact on the insertion loss. This is mainly due to the relatively small refractive index contrast of the overclad WOP ($n_\mathrm{core} = 1.53$, $n_\mathrm{cladding} = 1.36$), which reduces the roughness-induced scattering compared to high-index-contrast silicon-photonic waveguides. Moreover, the roughness is mainly induced by horizontal slicing of the 3D structure during the writing process, which makes the horizontal WOP sections essentially invariant along the propagation direction.

The high losses in the current structures arise from the fact that the WOP bridges
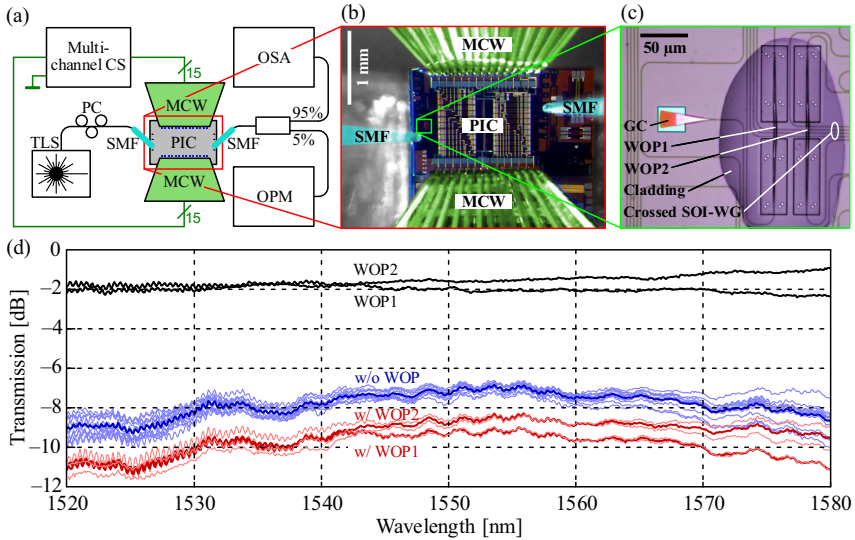
Figure 4.3: Experimental demonstration of the 4×4 SAS with WOP. The layout of the SAS circuit is similar to the one depicted in Fig. 4.2(d). (a) Experimental setup. A multi-channel current source (CS) is used to drive different subsets of 16 out of the overall 24 optical 1×2 and 2×1 MZI switches via two multi-contact probe wedges (MCW). This allows testing of all 16 possible optical paths that connect the various input and output ports of the 4×4 SAS PIC. A tunable laser source (TLS) and a polarization controller (PC) are used to generate continuous-wave (CW) test signals that are launched to the various ports of the SAS PIC via a single-mode fiber (SMF) and grating couplers (GC). Each of the four optical outputs can be probed by another SMF, and the output signal is analyzed with an optical power meter (OPM) and an optical spectrum analyzer (OSA) that allows to perform a wavelength sweep that is synchronized with the TLS. (b) Microscope image of the SAS PIC with electrical and optical connections. (c) Microscope image of two waveguide overpasses (WOP), which bridge three and four SiP strip waveguides, respectively. A low-index cladding material is locally deposited with high precision to cover the printed WOP without blocking the nearby grating couplers. (d) Transmission spectra of various optical paths through the switch. **Pale blue:** Transmission spectra of 12 optical paths through the SAS PIC that do not contain any WOP (w/o WOP). **Bright blue:** Average transmission of the 12 paths w/oWOP. **Pale red:** Transmission spectra of two sets of two optical paths each, each set containing the same WOP (w/WOP1; w/WOP2). **Bright red:** Average transmission of each of the two sets w/WOP. **Black:** Transmission spectra of WOP1 and WOP2.

only four or less SiP waveguides, leading to a small width $w = 17\,\mu\text{m}$ of the oxide-overcladding rib underneath the WOP, see Fig. 4.1(b). Moreover, the distance of $d = 20\,\mu\text{m}$ between the tips of the tapered on-chip SiP waveguides and the edge of the oxide opening was rather small. In combination, these efects resulted in a

trajectory with a relatively strong curvature with local bending radii r down to 20 µm along the WOP trajectory to maintain a distance of at least 2 µm between the WOP and the 2.3 µm-high oxide-overcladding rib. This problem can be avoided by either bridging more SiP waveguides or by choosing a slightly larger distance d in case only a few waveguides are to be bridged. Specifically, for seven or more SiP waveguides with spacings of 3.5 µm, the width of the overcladding-oxide rib increases to $w \geq 25$ µm, which allows to maintain a radius of curvature of more than 40 µm along the WOP trajectory even for $d = 20$ µm. Taking into account the tapered transition between the SiP on-chip waveguide ($l_t = 50$ µm) and the WOP, the overall space occupied to each side of the overcladding-oxide rib amounts to $d + l_t = 70$ µm. This compares favorably to the 190 µm-long transitions between the bottom and the top layer of a SiN-based multilayer photonic circuit [126, 128]. When bridging less than seven in-plane SiP waveguides, we should still maintain a minimum spacing of $d_{tip} \approx 65$ µm between the tips of the coupling structures to avoid a strongly bent WOP trajectory. In this case, the space occupied by the WOP to either side of the bridged waveguides is still less than $l_t + d_{tip}/2 \approx 83$ µm. Note that WOP can also be coupled to vertical waveguide facets [130], e.g., in deep-etched trenches, thereby greatly reducing the footprint by omitting the 50 µm-long tapered transitions.

Regarding scalability of the WOP to large numbers of crossed waveguides, we have performed simulations of 3D polymer waveguides comparable to WOP in our previous work [34], finding that for an optimized waveguide trajectory the insertion loss is dominated by the coupling to the SiP waveguide rather than by the length of the polymer waveguide section. Therefore, assuming an optimized WOP trajectory, increasing the WOP length should not lead to significantly higher losses. Each additionally crossed SiP waveguide increases the WOP length by approximately 3.5 µm, which is dictated by the minimum spacing between the SiP waveguides that is needed to avoid crosstalk between them. Further reduction of the spacing can be achieved by using different SiP waveguide widths to avoid crosstalk [135]. Regarding very complex circuit topologies, the WOP footprint

may hence scale very well. The overall footprint of our current SAS circuit amounts to approximately $1.8 \times 1.4\,\text{mm}^2$, mainly dictated by the rather bulky $500\,\mu\text{m}$-long thermo-optic phase shifters and the associated electric contact pads. This footprint can be reduced by using MZI switch modules based on ultra-compact liquid-crystal phase shifters, which can provide phase shifts in excess of π for a length of less than $500\,\mu\text{m}$ [136, 137].

We also measured the crosstalk from a WOP to one of the SiP waveguides underneath. To this end, we first maximized the optical transmission of two paths through the SAS PIC, where the first path ("Path 1") contains the WOP while the second path ("Path 2") contains one of the SiP waveguides underneath. We then launch a strong CW signal into the input of Path 1, and we connect highly sensitive power detectors to the output of both Path 1 and Path 2. Path 1 and Path 2 are marked in green and in blue, respectively, in Fig. 4.2(d), and the arrows indicate the direction of light propagation for the crosstalk measurement. To isolate the crosstalk contribution of spurious substrate modes excited at the input grating coupler from the impact of the WOP, we modulated the drive current of MZI right before the WOP ("MZI1", marked in green) with a sinusoidal signal at a distinct lock-in frequency of $f_{\text{LI}} = 10\,\text{kHz}$. We then used a lock-in amplifier to measure the RMS values of the optical power fluctuations at this modulation frequency both at the output of Path 1 and at the output of Path 2. The crosstalk is obtained by calculating the ratio of the two lock-in signals and amounts to $-75\,\text{dB}$ at a wavelength of $1550\,\text{nm}$. This number compares favorably with the crosstalk of $-56\,\text{dB}$ reported for SiN-based multi-layer circuits [126, 128]. Note that our crosstalk figure does not account for differences in on-chip loss between the point where the crosstalk is generated and the output GC of Path 1 and Path 2. Also note that this value very likely represents an upper limit for the WOP crosstalk, since it also contains contributions of other on-chip elements such as waveguide bends and lossy MMI couplers that follow MZI1.

4.5 **Summary**

We introduced a concept for realizing PIC with non-planar topologies. Planar waveguide crossings (WGX) are replaced by 3D-printed freeform waveguide overpasses (WOP). We demonstrate the viability of the approach using a silicon photonic 4×4 switch-and-select (SAS) structure. Our theoretical analysis shows that the number of crossings for an $n \times n$ SAS device realized using surface couplers scales with $n^4/16$, while the number of required WOP scales with $n^2/2$. We believe that the results may offer an attractive path towards highly complex PIC with non-planar topologies.

[end of main part of publication [J3]]

5 Polarization beam splitter and rotator based on photonic wire bonds

This chapter reports on a design and experimental realization of a 3D-printed polarization beam splitter / polarization rotator assembly. The chapter is based on the manuscript [J2], that will be submitted for publication to Light: Science & Application, and it has been formatted in accordance to the formatting of this document. Methods and Supplementary Information related to this chapter, that are also based on the aforementioned manuscript, can be found in Appendix C.

Note that the author of this thesis and M. Blaicher contributed equally to this manuscript. The author proposed the polarization beam splitter (PBS) concept, and developed the PBS design. M. Blaicher developed the design of polarization rotators, mode-field adapters, connecting waveguides, the fanout, and the structures for mechanical support. M. Blaicher developed and built the 3D printing system and fabricated all structures. The experiments were jointly conceived by the author, M. Blaicher, and C. Koos. The author and M. Blaicher jointly characterized the fabricated devices. The author and P. Marin-Palomo performed the data transmission experiment with support of C. Füllner and S. Randel, who conceived and implemented the signal processing tools. P. Marin-Palomo analyzed the results of the data-transmission experiment. The figures were jointly made, and the manuscript was jointly written by the author and M. Blaicher, supported by C. Koos. The work was jointly supervised by W. Freude and C. Koos.

[start of the content based on the main part of manuscript [J2]]

Ultra-broadband polarization beam splitter and rotator based on 3D-printed waveguides

To be submitted for publication to Light: Science & Applications

Aleksandar Nesic,[1†] Matthias Blaicher,[1,2†] Pablo Marin-Palomo,[1] Christoph Füllner,[1] Sebastian Randel,[1] Wolfgang Freude,[1] and Christian Koos[1,2]

[1]*Karlsruhe Institute of Technology (KIT), Institute of Photonics and Quantum Electronics (IPQ), Engesserstrasse 5, 76131 Karlsruhe, Germany*
[2]*Karlsruhe Institute of Technology (KIT), Institute of Microstructure Technology (IMT), Hermann-von-Helmholtz-Platz 1, 76344 Eggenstein-Leopoldshafen, Germany*
[†]These authors contributed equally to this work.

Multi-photon lithography has emerged as a powerful tool for photonic integration, allowing to complement planar photonic circuits by 3D freeform structures such as waveguides or micro-optical elements. These structures facilitate light transport and can be fabricated with high precision on the facets of optical devices. However, plain light transport is far from exploiting the full geometrical design freedom that is offered by 3D laser lithography. Here, we extend the functionality of 3D-printed optical structures towards manipulation of optical polarization states. We demonstrate compact and ultra-broadband polarization beam splitters (PBS) combined with polarization rotators (PR) and mode-field adapters into a monolithic structure that can be directly printed on facets of optical devices. Our first-generation devices exhibit measured polarization extinction ratios beyond 11 dB over a 360 nm wavelength range. We demonstrate a 640 Gb/s dual-polarization data-transmission at a wavelength of $\lambda = 1550$ nm using 16-state quadrature amplitude modulation (16QAM) at a symbol rate of 80 GBd, without optical signal-to-noise ratio (OSNR) penalty compared to a commercial PBS.

5.1   Introduction

Polarization manipulation is of great importance for integrated optical systems, in particular when it comes to interfacing rotationally symmetric optical fibers with degenerate polarization states to highly polarization-sensitive on-chip waveguides. In conventional optical systems, polarization manipulation usually relies on discrete optical elements such as polarization beam splitters (PBS) or waveplates made from birefringent materials. These devices offer high polarization purity and low insertion loss over a large spectral range. When used in integrated photonic systems, however, the viability of discrete polarization-manipulating elements is limited, e.g., by the required footprint or by the need for high-precision alignment of these elements with respect to on-chip optical circuits [138]. Alternatively, polarization-manipulating functionalities can be integrated into waveguide-based planar photonic circuits, exploiting, e.g., mode-selective directional or multimode interference couplers [72, 73, 139–142], polarization mode converters [20, 74], waveguide gratings [143], waveguide structures with multi-layer cores [21, 22], or more complicated structures obtained by inverse design techniques [19]. These devices can be efficiently realized in large quantities, but often require special fabrication steps [21, 22] and are subject to limitations of the device geometry, dictated by conventional layer-by-layer microstructuring through 2D lithography and dry etching. Moreover, polarization manipulation in on-chip structures often relies on efficient coupling of light to the associated waveguides in the first place. In silicon photonics, grating-based polarization beam splitters can be directly integrated into the fiber-chip interface [18]. However, these structures are subject to limited bandwidth and still rely on high-precision active alignment of the single-mode fiber with respect to the on-chip grating coupler. A PBS based on a prism and a diffraction grating 3D printed on the facet of a single-mode fiber (SMF) has been recently reported [144]. However, the device is intrinsically narrow-banded, and the split polarizations are coupled into free space and unsuitable for photonic integration with other components.

In this chapter, we demonstrate ultra-broadband 3D-printed waveguide-based polarization beam splitters and rotators, as an alternative to conventional polarization-manipulating elements in integrated optics. In our structures, polarization splitting is accomplished through adiabatic Y-branches of geometrically birefringent polymer waveguides with high-aspect-ratio cross sections and complemented by polarization rotation in waveguides that are twisted along the propagation direction. The structures can be directly incorporated into freeform chip-chip and fiber-chip connections [13, 34], so-called photonic wire bonds. In our proof-of-concept experiments, we show monolithic structures that are 3D-printed on facets of SMF comprising ultra-broadband polarization beam splitters, polarization rotators, and mode-field adapters. Our prototypes feature more than 11 dB polarization extinction ratios in a wavelength range (1260–1620) nm, with vast potential for further improvement. We demonstrate the viability of the structures by deploying them in a dual-polarization data-transmission experiment and benchmarking their performance with a commercially available fiber-based PBS as a reference. By using 16-state quadrature amplitude modulation (16QAM) at a symbol rate of 80 GBd, we transmit data at an aggregate data rate of 640 Gb/s at a wavelength of $\lambda = 1550$ nm, with virtually the same optical signal-to-noise ratio as with the reference PBS. We believe that 3D-printed optical structures for polarization manipulation can replace costly assemblies of discrete micro-optical elements, thereby paving the path towards optical systems with unprecedented compactness and scalability.

5.2 Device concept and design

The concept of a 3D-printed PBS and polarization rotator (PR) in an integrated optical assembly is illustrated in Fig. 5.1. The device connects a rotationally symmetric single-mode fiber (SMF) with degenerate polarization states to highly polarization-sensitive photonic integrated circuit (PIC). The illustrated assembly acts as a dual-polarization receiver for coherent communications, in which data signals in orthogonal polarization states are split and independently detected using

a pair of coherent optical receivers (Coh. Rx) fed by a joint local oscillator (LO). The PBS/PR can be merged with additional 3D freeform waveguide elements such as mode-field adapters into a single monolithic structure. This structure can be fabricated in a single exposure step by high-resolution 3D-laser lithography that exploits multi-photon polymerization in the focus of a pulsed femtosecond laser beam [106]. This offers the freedom to adapt the geometry of the 3D-printed structure to the positions of the adjacent optical device facets, thereby overcoming the need for high-precision mechanical alignment [13, 34]. Note that the assembly illustrated in Fig. 5.1 represents only one example of 3D-printed polarization-manipulating elements. In general, the structures can be printed on a wide range of optical devices, covering applications from optical communications and signal processing [80, 145] to optical metrology [4, 84], imaging [7], and quantum optics [146, 147].

The working principle of our 3D freeform waveguide-based PBS is illustrated in Fig. 5.2. Figure 5.2(a) depicts a 3D rendering of the three-port device, comprising an input waveguide port with a circular cross section and a pair of output waveguide ports with rectangular cross sections of high aspect ratio. In the following, the input port is denoted by a superscript (I), whereas superscripts (H) and (V) refer to the output ports with horizontally and vertically oriented rectangular cross section, see Fig. 5.2(a). Note that the device is fully bidirectional and can also be used as a polarization beam combiner, where the two rectangular waveguide ports H and V are used as inputs, whereas the circular port I acts as output.

The PBS consists of three segments denoted by A, B, and C, where Segment A is directly adjacent to the input port. Due to its circular cross section, the input port has two degenerate fundamental modes of orthogonal polarizations with identical effective refractive indices n_{eff}. We select the two basis modes at the input with the dominant transverse component of electric field aligned in the vertical and horizontal direction as defined by the two output ports, and we denote them by $E_H^{(I)}$ and $E_V^{(I)}$ respectively, see first row of Fig. 5.2(b) for the associated mode-field distributions. Within Segment A, the circular cross section at the input
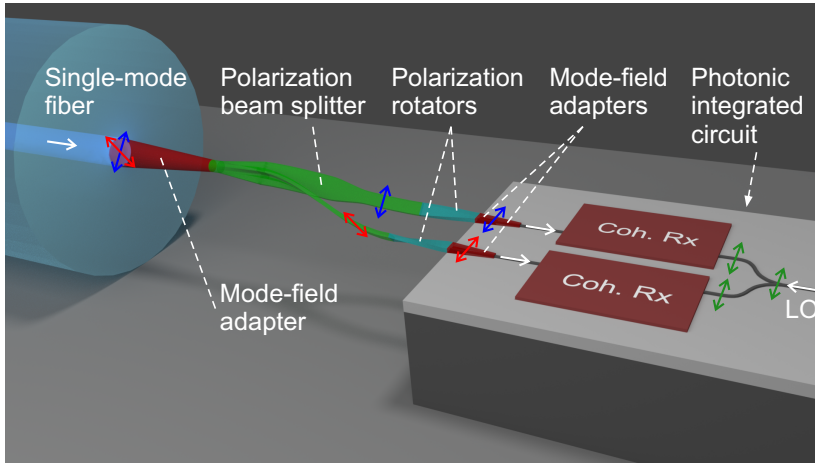
Figure 5.1: Vision of a 3D-printed polarization beam splitter and rotator in an integrated optical assembly (not drawn to scale). The device connects a rotationally symmetric single-mode fiber (SMF) with degenerate polarization states (red and blue arrows) to a photonic integrated circuit (PIC) with highly polarization-sensitive waveguides. As an example of high practical interest, we illustrate a dual-polarization receiver for coherent communications, in which data signals in orthogonal polarization states are split and independently detected using a pair of coherent optical receivers (Coh. Rx) which are fed by a joint local oscillator (LO). The polarization beam splitter (PBS) and the polarization rotator (PR) can be merged with additional 3D freeform waveguide elements such as mode-field adapters into a single monolithic structure. This structure can be fabricated in a single exposure step by high-resolution 3D-laser lithography, thereby offering the freedom to adapt the geometry of the 3D-printed structure to the positions of various optical device facets.

port is adiabatically morphed into a cross-shaped cross section at the transition to Segment B. At the transition between Section A and Section B the waveguide can be represented by two spatially overlapping partial waveguides WG$_H$ and WG$_V$ with high-aspect-ratio rectangular cross-sections. Due to the adiabatic transition from a circular cross section to a cross-shaped one in Section A, the degenerate basis modes denoted as $E_H^{(I)}$ and $E_V^{(I)}$ are transformed to the strongly guided modes of these rectangular partial waveguides. In this context, the term strongly guided denotes a mode of a rectangular waveguide which is polarized along the long side of the rectangle with a homogeneous cladding. This mode exhibits a higher effective refractive index than its weakly guided counterpart that is polarized along

the short side of the rectangle. In Section B, the partial waveguides WG_H and WG_V are gradually separated, thereby dragging the corresponding strongly guided eigenmodes into the two distinct waveguides at the input of Segment C.

Within Segment C, the two distinct output waveguides can be adiabatically tapered and bent to suppress unwanted higher-order modes and to route the waveguides to the two output ports V and H. Further 3D-printed freeform waveguide structures can be directly connected to these output ports, e.g., for polarization rotation, see Fig. 5.1. The second and the third row of Fig. 5.2(b) show the various mode-field profiles at the output, where $E_H^{(V)}$ refers to the horizontally and $E_V^{(V)}$ to the vertically polarized mode at the vertical output V, whereas $E_V^{(H)}$ denotes the vertically and $E_H^{(H)}$ the horizontally polarized mode at horizontal output H. In an ideal device, the power of the degenerate $E_H^{(I)}$ and $E_V^{(I)}$ is completely coupled to the strongly guided modes $E_H^{(H)}$ and $E_V^{(V)}$, whereas the weakly guided modes $E_H^{(V)}$ and $E_V^{(H)}$ are not excited.

To estimate the performance of the proposed PBS, we perform numerical simulations of the full 3D structure, see Appendix C.1 for details. For good performance, the aspect ratio of the rectangular waveguide cross sections should be as high as possible while staying compatible with the resolution of the 3D printing system. In the simulated structure, the short side of the rectangle was chosen to $w_{sh} = 400\,nm$, whereas the long side varied in the range $w_{lo} = (1.2\text{–}2.2)\,\mu m$. The length of the structure amounts to $L = 21\,\mu m$. The PBS features full geometrical symmetry, see Inset 1 of Fig. 5.2(a), which results in symmetrical relationships between the port modes. Fig. 5.2(a), we illustrate the magnitude of the E-field plot at a wavelength of 1550 nm for the horizontal input polarization — the E-field distribution for vertical input polarization is obtained by reflection about the symmetry plane. To describe the coupling between the various modes at the input and the output ports, we use scattering parameters (S-parameters) $\underline{S}_{AB}$. In this description, $\underline{S}_{AB}$ refers to the transmission from B to A where $A, B \in \left\{ E_H^{(I)}, E_V^{(I)}, E_H^{(H)}, E_V^{(H)}, E_H^{(V)}, E_V^{(V)} \right\}$ denote the various modes at the ports of the device. The results for the various simulated coupling coefficients are shown in Fig. 5.2(c). Evaluating the transmission
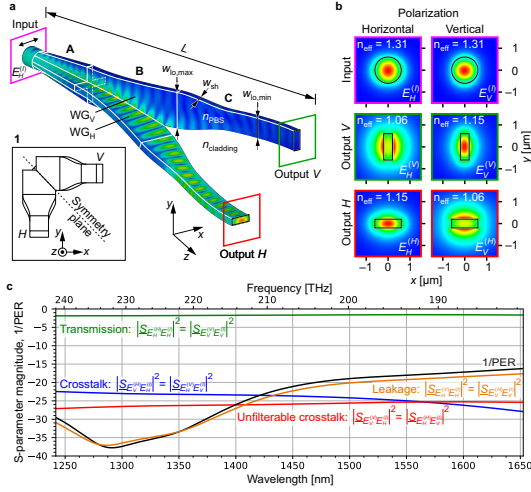
Figure 5.2: Concept and design of 3D-printed waveguide-based PBS. (a) 3D model of the PBS, comprising an input waveguide port with a circular cross section and a pair of output waveguide ports with rectangular cross sections of high aspect ratio. The two orthogonally polarized modes at the input port are denoted by $E_H^{(I)}$ and $E_V^{(I)}$, whereas $E_H^{(V)}$ refers to the horizontally and $E_V^{(V)}$ to the vertically polarized mode at the vertical output V, while $E_V^{(H)}$ denotes the vertically and $E_H^{(H)}$ the horizontally polarized mode at the horizontal output H. The PBS consists of three segments denoted by A, B, and C. Within Segment A, the circular cross section at the input port is adiabatically morphed into a cross-shaped cross-section. Within Segment B, the structure can be represented by two spatially overlapping partial waveguides WG_H and WG_V with high-aspect-ratio rectangular cross-sections, which are gradually separated to drag the strongly guided eigenmodes into the two distinct waveguides at the input of Segment C. The 3D rendering of the structure also depicts the simulated electric field distribution for a horizontally polarized excitation $E_H^{(I)}$ at the input port. The PBS exhibits full geometrical symmetry, see Inset 1, i.e., a vertically polarized excitation at the input would cause a symmetrical response with respect to the symmetry plane. The refractive index of the PBS is equal to $n_{PBS} = 1.53$, and the cladding material is air, $n_{cladding} = 1$. (b) Electric field plots of the fundamental modes for both polarizations at all ports. The strongly guided target modes $E_H^{(H)}$ and $E_V^{(V)}$ at the horizontal and vertical output exhibit a higher effective index and a stronger confinement to the rectangular core than the undesired modes $E_V^{(H)}$ and $E_H^{(V)}$. (c) Simulated wavelength dependence of the squared magnitudes of complex scattering parameters (S-parameters) and the reciprocal of the polarization extinction ratio (PER) of the PBS on a logarithmic scale. The transmission is better than $-2.0\,$dB with a maximum of approximately $-1.6\,$dB near $\lambda = 1550\,$nm. The reciprocal of the polarization extinction ratio (PER), and spurious coupling between input and output modes are below $-16\,$dB over the 400 nm wide wavelength range. These parameters can be further reduced for smaller wavelength ranges. Details on extracting the PER can be found in Appendix C.2.

$\underline{S}_{E_H^{(H)} E_H^{(I)}} = \underline{S}_{E_V^{(V)} E_V^{(I)}}$ from the input to the desired mode of the respective output port, we find an insertion loss of less than 2 dB over the entire wavelength range between 1250 nm and 1650 nm, with a minimum of 1.6 dB near 1550 nm, see green line in Fig. 5.2(c). For each polarization at the input port, we further extract the power that is coupled to the undesired mode at the corresponding "correct" output port, which is quantified by the crosstalk $\underline{S}_{E_V^{(H)} E_H^{(I)}} = \underline{S}_{E_H^{(V)} E_V^{(I)}}$, and which is below -22 dB throughout the simulated wavelength range, see blue line in Fig. 5.2(c). Note that this crosstalk can be suppressed by subsequent polarization filtering. We further calculate the power that is coupled to the desired output modes $E_H^{(H)}$ and $E_V^{(V)}$, from the "wrong" input modes $E_V^{(I)}$ and $E_H^{(I)}$, respectively, and that cannot be suppressed by subsequent polarization filters. This unfilterable crosstalk $\underline{S}_{E_H^{(H)} E_V^{(I)}} = \underline{S}_{E_V^{(V)} E_H^{(I)}}$ is represented by the red line in Fig. 5.2(c) and is below -25 dB throughout the 400 nm-wide wavelength range of interest. We also extract the polarization leakage $\underline{S}_{E_H^{(V)} E_H^{(I)}} = \underline{S}_{E_V^{(H)} E_V^{(I)}}$, which, for a given polarization at the input port quantifies the power coupled to undesired polarization at the "wrong" output port, thereby maintain its polarization. For our structure, the polarization leakage is below -17 dB throughout the simulated wavelength range, see orange line in Fig. 5.2(c), and can be further suppressed by subsequent polarization filters. Finally, we extract the polarization extinction ratio (PER), i.e., the ratio of the maximum and the minimum power observed in both modes of an output port when varying the excitation at the input over all possible polarization states. For each of the output ports, the PER can be obtained from a singular-value decomposition of the corresponding Jones matrix, see Appendix C.2 for details. We find that the PER is better than 16 dB within the investigated wavelength range and shows a strong increase towards longer wavelengths. Note that PER and polarization leakage are better than 30 dB over the wavelength range between 1250 nm and 1365 nm, and that this wavelength range of high performance can be shifted by adapting the design of the structure.

5.3 Experimental verification

To experimentally prove the viability of our concept, we fabricate a series of 3D-printed PBS that are directly connected to the cores of single-mode fibers (SMF). We characterize the performance of these devices and finally use them as part of a receiver in polarization-division multiplexing (PDM) data transmission experiment.

5.3.1 Characterization of basic performance parameters

In a first experiment, we fabricate a series of freestanding PBS on the facets of an SMF array and measure the performance through an infra-red-sensitive microscope (IR microscope), see Fig. 3a. To ensure low-loss coupling to the SMF core, the structures are equipped with adiabatic mode-field adapters that are attached to Section A of the PBS. A scanning-electron microscope (SEM) image of the PBS and the mode-field adapter are shown in Fig. 5.3(b). Light is fed to the SMF by a laser emitting at a wavelength of $\lambda = 1550\,\text{nm}$, and subsequent polarization controller. At the two PBS outputs, the light is radiated into free space and picked up by the IR microscope. The centers of the white circles in the images of Fig. 5.3(c) match the centers of corresponding PBS output ports, and the areas of the circles denote the areas that have been considered in calculating the corresponding power levels.

In a first set of measurements we show that radiated light can be switched between the two output ports of the PBS by varying the polarization at the input, see Column 1 of Fig. 5.3(c). Specifically, Subfigures 1.1 and 2.1 refer to the cases where the polarization controller was adjusted for maximum radiation from output Port V and H, having vertically and horizontally oriented waveguide cross-sections, respectively. In both cases, we measure the ratio Γ of the optical power at the targeted output port to the residual power emitted at the respective other port, which amounts to 9.8 dB and 9.7 dB, respectively. We also adjust the input polarization to yield equal power at both ports, see Subfigure 3.1 in Fig. 5.3(c). In order to
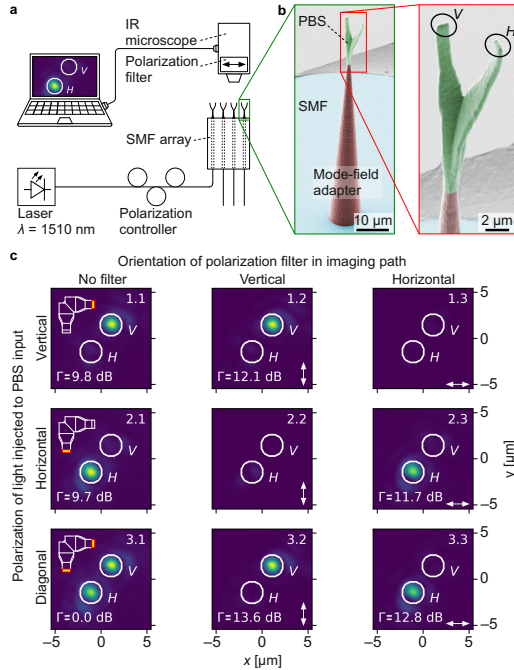
Figure 5.3: Characterization of 3D-printed PBS using an infra-red-sensitive (IR) microscope. (a) Experimental setup: As test structures, we use a series of PBS that are 3D-printed on the facets of a single-mode fiber (SMF) array. Light at a wavelength of 1550 nm is fed to the device by a laser and a subsequent polarization controller. Light emitted from the PBS is characterized by an IR microscope equipped with polarization filter (PF). (b) Scanning-electron microscopy (SEM) images of a fabricated structure on the fiber array. A linear taper structure, shaded in red, is used at the input of the PBS to adapt the mode-field diameter of the SMF to the one of the PBS input. Within the PBS, which is illustrated in green, the light is split into two orthogonal polarizations and emitted from the outputs (*V* and *H*) towards the IR microscope. Colors were added by image processing. (c) Recordings on the IR microscope for different combinations of input polarization states, indicated by the different rows: Row 1 – vertical input polarization only, Row 2 – horizontal input polarization only, and Row 3 – both vertical and horizontal input polarizations. The columns correspond to the measurement of the radiated power without (Column 1) and with vertically and horizontally oriented polarization filter (Columns 2 and 3, respectively) in the imaging path of the IR microscope. The output power of each port is estimated by integrating the measured intensity over the areas within the white circles, and a power ratio Γ in dB is calculated by dividing the larger by the smaller power. A top view of the PBS structure and the respective "active" output port for each row is additionally illustrated in Column 1. The orientation of the polarization axis of the PF is illustrated by the double arrows in the lower right-hand corner of the displays in Columns 2 and 3.

check the polarization states of the light radiated from the two outputs, we repeat the experiment with a vertically and horizontally oriented polarization filter (PF) between the microscope objective and the IR camera, see Columns 2 and 3 of Fig. 5.3(c). The PF has an extinction ratio of more than 34 dB. Assuming an excitation with pure vertical polarization in Row 1 of Fig. 5.3(c), the vertically oriented PF in Subfigure 1.2 suppresses the spurious horizontal polarization at Port V, which corresponds to the crosstalk $\underline{S}_{E_V^{(V)} E_V^{(I)}}$, as well the spurious horizontal polarization at Port H, which represents the unfilterable crosstalk $\underline{S}_{E_H^{(H)} E_V^{(I)}}$. The measured power ratio Γ of the emitted light after the PF amounts to 12.1 dB and corresponds to the ratio $\left| \underline{S}_{E_V^{(V)} E_V^{(I)}} \right|^2$ of the power transmission at Port V and the leakage at Port H. The measured ratio is smaller than the approximately 18 dB that would be expected from the simulation results, see Fig. 5.2(c). We attribute the deviations to geometrical inaccuracies of the fabricated structure. In Subfigure 2.2, the PF is oriented horizontally, such that only spurious horizontal polarizations at both outputs, $\left| \underline{S}_{E_H^{(H)} E_V^{(I)}} \right|^2$ and $\left| \underline{S}_{E_H^{(V)} E_V^{(I)}} \right|^2$ can be seen on the IR camera. As expected, the camera image does not show any significant power. In Subfigure 3.2, where light exits both output arms of the PBS, the light radiated from Port H is completely suppressed by the vertically oriented PF, whereas the light radiated from Port V does not experience a significant attenuation. The same experiment is repeated with a horizontally oriented PF, see Column 3 of Fig. 5.3(c), thereby essentially reproducing the findings described for the data in the second column. This simple experiment demonstrates that the device qualitatively works as expected.

5.3.2 Measurement of polarization extinction ratio (PER)

We further test our PBS structures by measuring the PER over a broad range of wavelengths. To this end, the polarization at the input of the structure is varied randomly by a polarization scrambler, while the Stokes vector and the power at the device output are continuously recorded by a polarimeter, see Fig. 5.4(a) for a sketch of the associated setup. The measurement is repeated for each of the output

ports, thereby revealing the output polarization state of maximum and minimum transmission as well as the associated PER. The PBS test structure used in this experiment is again 3D-printed on the facet of an SMF array which is connected to the polarization scrambler. At the output, the structure is equipped with a pair of polarization rotators (PR), realized by rectangular waveguides that are twisted by 45° along the propagation direction [75, 76], thus providing identical polarizations at both ports, see Fig. 5.4(b). For better probing of the output, the structure is equipped with adiabatic mode-field adapters that are held by a table-like mechanical support structure and that can be individually probed by moving an SMF to the respective port. Note that, due to the unknown polarization rotation in the SMF, our measurement only allows to determine the exact polarization state at the input of the polarimeter, but not at the output ports of the PBS/PR. This needs to be considered when evaluating the measurement data, see Appendix C.3 for details. Note also that the two output ports of our structure are only separated by 25 µm, and we may hence assume that the polarization rotation in the SMF does not change significantly when moving the SMF between the ports. For an ideal device, the two ports should thus exhibit transmission at identical output polarization states.

The measurement results obtained from our test structure at wavelength of $\lambda =$ 1460 nm are depicted in Fig. 5.4(c). For this measurement, the input polarization state was scanned across 20 000 points uniformly distributed on the Poincaré sphere. The plot shows the measured Stokes states on the Poincaré sphere in Mollweide projection, colored by normalized transmitted power. For each of the two device outputs, we find a predominant polarization state, which we mark by $s_{out,pass,1}$ and $s_{out,pass,2}$ in Fig. 5.4(c). These states correspond to the polarization that would be transmitted to the respective output of a perfect PBS. For a real device with finite PER, the output polarization states $s_{out,pass,1}$ and $s_{out,pass,2}$ exhibit the highest power transmission. At the same time, the measured output polarization states are concentrated around $s_{out,pass,1}$ and $s_{out,pass,2}$ in case the input polarization is randomly varied. Note that, for simplicity, we rotated all measured Stokes vectors
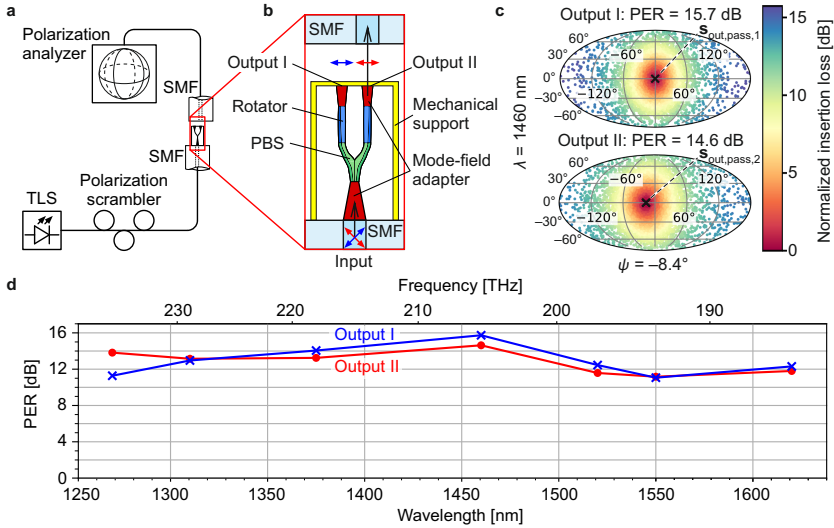
Figure 5.4: Measurement of the polarization extinction ratio (PER) of the PBS with attached polarization rotators (PR). (a) Experimental setup: The PBS is 3D-printed on the facet of an SMF through which light is coupled-in from a polarization scrambler. The two output ports are probed by a movable SMF, which is attached to a polarization analyzer. The polarization at the input is scrambled randomly, and the Stokes vector of the output polarization state is measured for both outputs. (b) Schematic rendering of the PBS with attached PR and mode-field adapters, which are attached to a table-like mechanical support structure. Orthogonal polarization states (blue, red) at the input port are separated to identical polarization states at the output of the structure. (c) Measured output Stokes states on the Poincaré sphere in Mollweide projection, colored by normalized transmitted power. For simplicity, we rotate all measured Stokes vectors such that the predominant polarization state at Output I, $s_{out,pass,1}$, is oriented along the s_1-direction of the Poincaré sphere (0° longitude and 0° latitude in Mollweide projection), which corresponds to a linear polarization in horizontal direction, while the predominant polarization state at Output II, $s_{out,pass,2}$, is on the equator of the Poincaré sphere, corresponding to a linear polarization at a certain angle ψ with respect to the horizontal direction. We extract only a slight angle deviation of $\psi = -8.4°$ of the two equivalent linear polarization states, indicating correct operation of the PR. (d) Measurement of the PER for both outputs showing very broadband operation over 360 nm with PER in excess of 11 dB.

such that $s_{out,pass,1}$ is oriented along the s_1-direction (latitude 0° and longitude 0°), which corresponds to a linear polarization in horizontal direction, while $s_{out,pass,2}$ is on the equator of the Poincaré sphere, corresponding to a linear polarization at a certain angle ψ with respect to the horizontal direction. Note also that the transformation of the measured output polarizations to linear polarization states

is somewhat arbitrary since the true polarization transformation in the output fiber is unknown. Still, we extract only a slight angle deviation of $\psi = -8.4°$ of the two equivalent linear polarization states, indicating correct operation of the polarization rotators.

For each of the output ports, we then extract the polarization extinction ratio (PER), which is here defined as the ratio of the maximum transmitted power at the target output polarization state to the minimum power at the antipodal point on the Poincaré sphere. For better reliability of the extracted results, we implemented a PER evaluation technique that considers all power levels recorded for the various input polarization states rather than just the maximum and the minimum power, see Appendix C.3 for details. The experiment was repeated for different wavelengths over a broad range from 1260 nm to 1620 nm, see Fig. 5.4(d) for a plot of the extracted PER, which is better than 11 dB over the whole wavelength range. This is slightly worse than the performance expected by simulations, see Fig. 5.2(c). We also measured the insertion loss of the device using the polarization state of maximum transmission at each output port. At a wavelength of 1500 nm, we find losses of 4.4 dB and 3.8 dB for Output I and Output II, respectively. Note that these values include the loss of the PBS, of the subsequent PR, and of the adiabatic mode-size converters at the input and the output of the device. Still, there is room for improvement considering the sub-2 dB losses expected from simulations of the PBS structure only, see Fig. 5.2(c). We attribute the deviations between measurements and simulations to imperfections of the 3D-printed structure, caused by limited resolution and shrinkage of the resist structure upon development. Exploiting super-resolution 3D-lithography inspired by the concept of stimulated-emission-depletion (STED) [148] microscopy might allow to better resolve fine details of the PBS structure and to further enhance the performance of the devices in the future.

5.3.3 Data transmission experiment

Finally, in order to demonstrate the technical viability of 3D-printed PBS, we perform a polarization division multiplexing (PDM) data-transmission experiment that emulates the application scenario displayed in Fig. 5.1. The experimental setup and the results are shown in Fig. 5.5. The experiment relies on a PBS/PR combination as used in the previous experiments, complemented by an additional fan-out structure. This fan-out structure is 3D-printed on a second fiber array and allows to simultaneously couple both PBS outputs to a pair of outgoing SMF with a standard pitch of 127 µm, see Fig. 5.5(a). The fan-out structure is equipped with two lenses with a pitch of 25 µm that pick up light from the two PBS outputs, followed by a pair of total-internal-reflection (TIR) mirrors in each path to adjust the lateral offset of the beams at the output. At $\lambda = 1550$ nm, the measured insertion losses of the two channels of the fan-out are 1.2 dB and 1.9 dB, with a crosstalk between channels below -46 dB.

In the transmission experiment, we launch a 16QAM PDM signal at a symbol rate of 80 GBd and a center wavelength of $\lambda = 1550$ nm to the PBS, and we feed the two output signals of the PBS/PR assembly to a pair of coherent receivers, see Appendix C.4 for details. We perform the experiment with our 3D-printed PBS assembly and with a commercially available fiber-based PBS having a PER in excess of 30 dB. In both cases, we sweep the optical signal-to-noise ratio (OSNR) at the input of the PBS and we record the constellation diagrams along with the bit error ratios (BER), see Figs. 5.5(b) and 5.5(c). At a BER of 1×10^{-2}, our transmission setup exhibits an OSNR penalty of approximately 3 dB, see Fig. 5.5(c), which is in accordance with values in literature for similar modulation formats and symbol rates [149]. We find that the 3D-printed PBS/PR assembly does not introduce any additional OSNR penalty with respect to the commercial PBS, although the PER differ vastly. We attribute this to the fact that the polarization-sensitive mixing of the data signals with the local oscillator of the coherent optical receiver in combination with the digital polarization demultiplexing can easily compensate for the finite PER of our 3D-printed PBS. Hence, even though there is still room
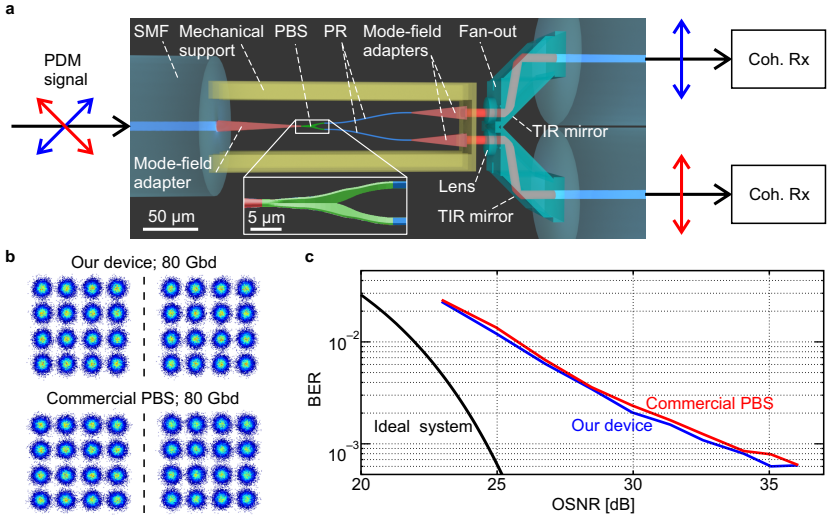
Figure 5.5: Experimental setup and results of proof-of-concept data transmission experiment. (a) Simplified experimental setup: The polarization-division-multiplexed (PDM) 16QAM signal is fed to an SMF having a 3D-printed polarization beam splitter (PBS) on its facet. The PBS is additionally equipped with 3D-printed polarization rotators in the form of twisted waveguides, which rotate both polarizations to an identical direction, similar to the structure in Fig. 5.4(b). We simultaneously probe the two output signals by a fan-out structure that is 3D-printed on a single-mode fiber array. The fan-out adapts the 25 μm pitch of the PBS/PR outputs to the 127 μm pitch of the fibers in the fiber array and features two lenses and two pairs of total-internal-reflection (TIR) mirrors. The signals are subsequently decoded by a pair of commercial coherent receivers (Coh. Rx). To benchmark our device, we repeat the experiment by replacing the PBS/PR assembly and the fan-out by a commercial fiber-based PBS. (b) Constellation diagrams of received 80 GBd 16QAM signals. Upper row: experiment with our device. Lower row: experiment with the commercial PBS. (c) Bit-error-ratio (BER) vs. optical signal-to-noise ratio (OSNR). **Black:** Theoretical curve for an ideal transmission system. **Blue:** Experiment with our 3D-printed PBS/PR assembly. **Red:** Experiment with the commercial PBS. Our device does not introduce an OSNR penalty with respect to the commercial PBS.

for improving the performance of our 3D-printed PBS/PR assemblies, the current devices already offer an attractive route towards highly scalable ultra-compact dual-polarization receivers as shown in Fig. 5.1.

5.4 **Summary**

We demonstrate 3D-printed waveguide-based polarization beam splitters (PBS) that can be efficiently integrated into chip-chip and fiber-chip interfaces of optical assemblies. The devices rely on adiabatic Y-branches of geometrically birefringent waveguides with high-aspect-ratio cross sections and can be complemented by polarization rotators (PR) that exploit twisted 3D freeform waveguides. The PBS/PR can be efficiently fabricated by direct-write two-photon lithography together with other 3D-printed elements such as photonic wire bonds [13, 34], 3D-printed microlenses [33], or 3D-printed waveguide overpasses [87]. In our proof-of-concept experiments, we demonstrate broadband operation in the range between (1260–1620) nm, limited only by the available equipment. We further prove the practical viability of the concept in a high-speed data transmission experiment, where our 3D-printed PBS/PR assemblies are used for separating polarization-multiplexed data signals at the receiver. We find that the quality of the received signals is on par with that obtained by a conventional high-performance fiber-based PBS. While the concept leaves room for further optimization, we believe that 3D-printed PBS/PR can pave the path towards efficient polarization manipulation in integrated optical systems with unprecedented compactness and scalability.

[end of the content based on the main part of manuscript [J2]]

6   Summary and Outlook

6.1   Summary

3D-printing through direct laser lithography is a promising technology for photonic integration. The range of optical devices that can be 3D-printed spans from freeform lenses and freeform waveguides for light transport and optical coupling, to photonic devices with advanced functionalities such as polarization beam splitters and to advanced circuits with non-planar topologies. In this work the following results were presented:

Transformation-optics based modeling of freeform waveguides: A method of accelerating time-domain simulations of 3D waveguides has been demonstrated by exploiting the concept of transformation optics. This concept enables mapping of bent waveguides from the original (x, y, z)-space into straight ones in a transformed (u, v, s)-space. A series of freeform waveguides with plane trajectories has been modeled using transformation optics, such that the trajectories of the waveguides were straightened in the transformed space. This enabled reduction of the simulation volume and reduction of the simulation time at a cost of calculating material properties of the waveguide in the transformed space. The net gain of using the transformation optics concept was 3–6 times shorter simulation times compared to reference simulations in the original space. The simulated transmission obtained by reference simulations in the original space show an excellent match to the transformation-optics based simulations. Experimentally measured transmission of 3D printed waveguides show a good qualitative match to simulated values.

Demonstration of a PIC with a non-planar topology realized without planar waveguide crossings with the help of 3D-printed waveguide overpasses: A

4×4 switch-and-select (SAS) PIC has been realized on a silicon photonic chip. The topology of the PIC requires at least four waveguide crossings when realizing the PIC in one plane. The required waveguide crossings were replaced by two 3D-printed waveguide overpasses (WOP). A graph theory analysis and a WOP minimizing PIC layout design algorithm for SAS circuits has been provided. It has been shown that the number of required WOP scales with the square root of the number of required waveguide crossing when realizing the PIC in one plane. The 3D-printed WOP bring flexibility in designing PIC layouts, and demonstrate superb crosstalk figures.

Demonstration of a 3D-printed waveguide based ultra broadband polarization beam splitter/polarization rotator assembly: A compact and ultra-broadband waveguide-based polarization beam splitter has been designed and simulated. The PBS is based on spatially overlapping geometrically birefringent waveguides that are adiabatically separated, thereby separating the two orthogonal polarization modes. The PBS has been experimentally realized on the facet of a single-mode fiber and complemented by two polarization rotators based on twisted waveguides. The PBS/PR assembly has been successfully used in a dual-polarization data transmission experiment with no optical signal-to-noise power ratio (OSNR) penalty compared to a commercially available PBS. *Note that the achievements related to the polarization beam splitter and rotator resulted from equal contributions of the author of the thesis and M. Blaicher. The author's work was focused on design and optimization of the polarization beam splitter, while the work of M. Blaicher was mainly focused on fabrication. The experimental characterization was done jointly by the author and M. Blaicher. For more details about individual contributions, see the introductory part of Chapter 5.*

6.2 Outlook and future work

The results presented in this thesis represent to a great extent proof-of-concept demonstrations. Therefore, there is potential for further improvements, for possible derivation of new concepts, and for an expansion of the application scenarios.

Transformation-optics based modeling of freeform waveguides: The results presented in Chapter 3 are obtained by applying the TO modeling principle to a commercially available FIT numerical solver of CST Microwave Studio. Due to limitations of the used solver, certain compromises needed to be done, such as using plane waveguide trajectories, and discretization of the waveguide model into *bricks* with constant material properties, rather than directly modifying the material properties on the mesh-cell level. To overcome these limitations, and to fully unlock the potential of the method, a dedicated numerical solver may be implemented. In addition, since the material properties (dielectric permittivity and magnetic permeability) in the transformed space are in general described not by two scalars but by two 3×3 tensors, the number of multiplications and additions in the constitutive relations that are performed in in each time-step is consequently increased. Therefore, a comprehensive computational complexity study is needed to classify the cases in which it is beneficial to use the TO modeling for simulating waveguide based structures.

3D-printed waveguide overpasses: The demonstrator PIC presented in Chapter 4 is a simple example with a small number of required planar waveguide crossings that were replaced by two WOP. The full potential of the approach can become prominent only in PIC with a higher topological complexity requiring much higher number of planar waveguide crossings. Next, the demonstrated WOP exhibited a relatively high insertion loss as a consequence of a non-optimum PIC layout design, which needs to be improved as explained in Section 4.4. Finally, the presented layout design algorithm for minimizing the WOP has been made for SAS circuits whose graph model is a complete bipartite graph, and there is no proof that this approach results in the minimum possible number of WOP. It would be interesting

to further expand the algorithm to account for more general PIC topologies, and to perform an additional graph-theory analysis for finding the minimum possible WOP number for realizing the corresponding PIC layouts.

3D-printed polarization manipulating devices The PBS design presented in Chapter 5 is based on a manual optimization. Although the obtained results are satisfactory, there is still room for improvements through a systematic optimization, especially concerning the insertion loss. For the purpose of demonstration, the data transmission experiment was done with a 3D-printed PBS/PR assembly on a single mode-fiber, while the outcoupling of the separated polarizations was done with an additional fan-out structure. One of the goals of future work is to directly connect the outputs of the PBS/PR assembly to waveguides on a PIC, as illustrated in Fig. 5.1. Next, the PBS can be used as a building block for a whole new class of 3D printed polarization manipulating assemblies/devices. Examples include polarization analyzers, polarization swappers, polarization sensitive cameras, etc. — see also patent disclosure [P1]. Finally, the PBS requires a high index-contrast between the core and the cladding regions to work properly, while the 3D-printed waveguides generally require index-matching cladding material that at the same time serves as humidity protection. In order to reconcile both requirements, it is necessary to devise a way for selective overcladding of the assembly by e.g. 3D-printing of protective enclosures around the PBS — see also patent application [P2].

Appendices

A   Transformation optics and freeform waveguide trajectories

The content of Appendix A is based on Appendices of paper [J1], and it has been modified to fit the formatting rules of this thesis.

Aleksandar Nesic, Matthias Blaicher, Emilio Orlandini, Tudor Olariu, Maria Paszkiewicz, Fernando Negredo, Pascal Kraft, Mariia Sukhova, Andreas Hofmann, Willy Dörfler, Carsten Rockstuhl, Wolfgang Freude, and Christian Koos

[start of the content based on appendices of manuscript [J1]]

A.1   Necessary condition for bijectivity of $(x, y, z)^{\mathrm{T}} = \mathbf{f}(u, v, s)$

As mentioned at the end of Section 3.2, a necessary condition for the bijectivity of the coordinate transformation function is, that no local center of curvature of the freeform waveguide trajectory is within the computational domain. We can keep the local center of curvature out of the computational domain by appropriately choosing the ranges of u- and v-coordinates. As an illustrative example, and for the sake of simplicity, we may think of a freeform waveguide with a plane trajectory (in the (y, z)-plane) consisting of two straight sections connected by a 90° bend with a constant bend radius r. The local center of curvature is point
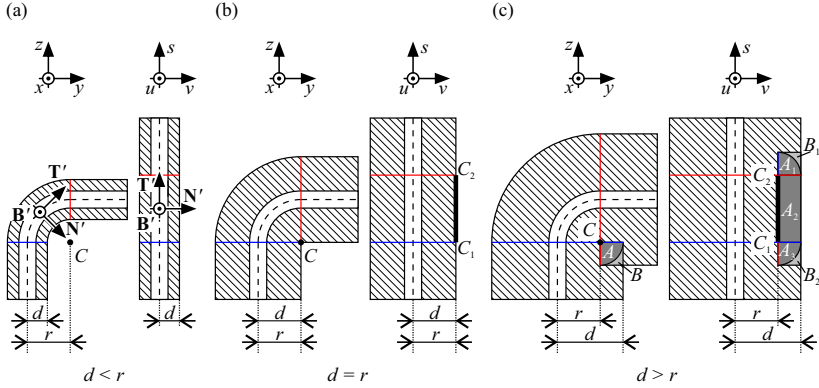
Figure A.1: Waveguide bends for illustrating of bijectivity condition for transfomation function $f(x, y, z) = (u, v, s)$. The different computational domains are limited by the outer boundaries of the hatched areas. We consider a plane freeform waveguide trajectory (dashed lines) in the (y, z)-plane. Two straight line segments are connected by a 90° circular bend with a bend radius r. Plane (y, z) in (x, y, z)-space (left drawings) corresponds to (u, v)-plane in (u, v, s)-space (right drawings). The local center of curvature is point C (the center of curvature of the 90° bend). The range of v-coordinates considered is $v \in [-d, +d]$. The RMF is shown only in case (a). (a) If $d < r$, the point C is outside the computational domain, and there is a bijective mapping between the two spaces. (b) If $d = r$, the point C is on the border of the computational domain. In this critical case, the space transformation function is not anymore a bijection, since the point C is mapped onto the line segment $C_1 C_2$ in (u, v, s)-space. (c) If $d > r$, the subdomains A and B from (x, y, z)-space are mapped to multiple sub-domains A_1, A_2, A_3 and B_1, B_2 in (u, v, s)-space, and the one-to-one correspondence between the two spaces is violated.

C in the (y, z)-plane, see Fig. A.1(a). As explained in Section 3.3, the RMF in all trajectory points is such that vector $\mathbf{B}'$ (pointing out of the drawing plane) is parallel to the x-axis and perpendicular to the (y, z)-plane. As a consequence, vector $\mathbf{N}'$ is always parallel to the (y, z)-plane. Since the vector $\mathbf{N}'$ is parallel to the v-axis in (u, v, s)-space, the range $v \in [-d, d]$ determines whether the point C is inside or outside the computational domain.

Without going into mathematical details (see the spatial transformation of 90° bends in Appendix A.3), we give a qualitative analysis of three cases: $d < r$, $d = r$, and $d > r$, Fig. A.1(a)–(c). Dashed lines represent waveguide trajectories, the white part in the middle represents the waveguide core, and the hatched parts

represent the cladding that is included in the computational domain. For all three cases we provide two drawings: One for the freeform waveguide in (y, z)-plane of (x, y, z)-space, and one for the same freeform waveguide in the (v, s)-plane of (u, v, s)-space. If $d < r$, the computational domain does not include point C, and the mapping between the two spaces is a bijection, see Fig. A.1(a). In case $d = r$, point C is on the border of the computational domain and is mapped to a line segment C_1C_2 in (u, v, s)-space, the length of which is equal to the arc-length of the 90° bend of the trajectory, $\overline{C_1C_2} = r\pi/2$, see Fig. A.1(b). This is the critical case when the spatial transformation function is not a bijection anymore. In case $d > r$, the one-to-one correspondence between the two spaces is further violated. Not only the point C is again mapped to the line segment C_1C_2, but also areas marked with A and B in the (y, z)-plane are mapped into multiple areas in the (v, s)-plane — see Fig. A.1(c). In particular, area A is mapped to areas A_1, A_2, and A_3, while area B is mapped to areas B_1 and B_2. It should be noted that in our example we took a symmetrical range of v-coordinates, which is not mandatory. A necessary condition is that C in Fig. A.1 is outside of the computational domain. For a physically correct description the essential part of the evanescent fields at the outside of the bend must be inside the computational domain.

This simple example is also very illustrative for the general case of freeform waveguides. Bends need not necessarily be 90° bends, and the bend radius can be continuously changing along the trajectory. In case of true 3D (non-plane) trajectories, the center of the bend radius lies in the oscullating plane, and the same reasoning provided in this Appendix can be applied. As a matter of fact, the oscullating plane for our example is the (y, z)-plane; the only difference to 3D trajectories would be that the vectors of the RMF are not necessarily perpendicular and parallel to the oscullating plane for each point on the trajectory.

A.2 Tensors of dielectric permittivity and magnetic permeability in (u, v, s)-space for freeform waveguides with plane trajectories

In case of freeform waveguides with plane trajectories and isotropic material properties ε and μ in the original (x, y, z)-space, the material properties $\boldsymbol{\varepsilon}'$ and $\boldsymbol{\mu}'$ in the virtual (u, v, s)-space are diagonal tensors. This can be shown by assuming that, without loss of generality, the plane trajectory lies in (y, z)-plane, as explained in Section 3.3 and Appendix A.1, such that the vector $\mathbf{U}$ of the RMF in each trajectory point is oriented parallel to the x-axis, while the remaining two vectors $\mathbf{V}$ and $\mathbf{T}$ of the RMF lie in the (y, z)-plane, with the vector $\mathbf{T}$ forming an angle θ with the positive z-axis, see Fig. (A.2). Since the vectors $\mathbf{V}$ and $\mathbf{T}$ are parallel to the v- and s-axes in the (u, v, s)-space, respectively, the axes of the 2D (v, s)-coordinate system are rotated by the same angle θ with respect to the axes of the 2D (y, z)-coordinate system. This allows us to simplify the calculation of the Jacobian matrix given by Eq. (3.2). Since the vector $\mathbf{U}$ and the x-axis are parallel to each other, it follows that $\partial u / \partial x = 1$. This also implies that the partial derivatives of u with respect to y and z must be zero, $\partial u / \partial y = 0$, and $\partial u / \partial z = 0$. Furthermore, the vectors $\mathbf{V}$ and $\mathbf{T}$ are perpendicular to the x-axis, which implies that the derivatives of v and s with respect to x must be zero, too: $\partial v / \partial x = 0$ and $\partial s / \partial x = 0$. The Jacobian matrix of the coordinate transformation function thus reads

$$\mathbf{J} = \begin{bmatrix} 1 & 0 & 0 \\ 0 & \frac{\partial v}{\partial y} & \frac{\partial v}{\partial z} \\ 0 & \frac{\partial s}{\partial y} & \frac{\partial s}{\partial z} \end{bmatrix}. \tag{A.1}$$

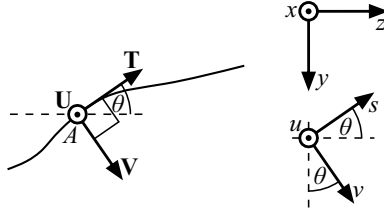**Figure A.2:** Relationship between coordinates in (x, y, z)- and (u, v, s)-space in a point A with
coordinates $(y_0(s), z_0(s))$ on the trajectory for the case of a freeform waveguide with a plane
trajectory. The trajectory lies in the (y, z)-plane, and the RMF is oriented such that the vector $\mathbf{U}$
and the associated u-axis are parallel to the x-axis in all points of the trajectory. The remaining
two axes $\mathbf{V}$ and $\mathbf{T}$ of the RMF define a 2D frame that lies in the (y, z)-plane. The axes of the local
(v, s)-coordinate system are parallel to the $(\mathbf{V}, \mathbf{T})$ frame and rotated by an angle θ with respect to the
axes of the (y, z)-coordinate system.

Assuming the material properties are isotropic in (x, y, z)-space, Eq. (3.1) can be
simplified,

$$
\begin{aligned}
\boldsymbol{\varepsilon}'(u, v, s) &= \varepsilon(x, y, z)\, \frac{\mathbf{J} \cdot \mathbf{J}^{\mathrm{T}}}{\det(\mathbf{J})}, \\
\boldsymbol{\mu}'(u, v, s) &= \mu(x, y, z)\, \frac{\mathbf{J} \cdot \mathbf{J}^{\mathrm{T}}}{\det(\mathbf{J})},
\end{aligned}
\tag{A.2}
$$

where the product of the Jacobian matrix and its transposed reads

$$
\mathbf{J} \cdot \mathbf{J}^{\mathrm{T}} =
\begin{bmatrix}
1 & 0 & 0 \\
0 & \left(\frac{\partial v}{\partial y}\right)^2 + \left(\frac{\partial v}{\partial z}\right)^2 & \left(\frac{\partial y}{\partial v}\frac{\partial y}{\partial s}\right)^{-1} + \left(\frac{\partial z}{\partial v}\frac{\partial z}{\partial s}\right)^{-1} \\
0 & \left(\frac{\partial y}{\partial v}\frac{\partial y}{\partial s}\right)^{-1} + \left(\frac{\partial z}{\partial v}\frac{\partial z}{\partial s}\right)^{-1} & \left(\frac{\partial s}{\partial y}\right)^2 + \left(\frac{\partial s}{\partial z}\right)^2
\end{bmatrix}.
\tag{A.3}
$$

Equation (A.3) is a diagonal matrix if its two off-diagonal elements are equal to
zero, which reduces to

$$
\frac{\partial y}{\partial v}\frac{\partial y}{\partial s} + \frac{\partial z}{\partial v}\frac{\partial z}{\partial s} = 0.
\tag{A.4}
$$

Since $\varepsilon(x, y, z)$, $\mu(x, y, z)$, and $\det(\mathbf{J})$ are scalars, it follows from Eqs. (A.2)
and (A.3) that Eq. (A.4) is a sufficient condition that ensures that $\boldsymbol{\varepsilon}'(u, v, s)$ and
$\boldsymbol{\mu}'(u, v, s)$ are diagonal tensors.

The coordinate transformation from the (v, s)-coordinate system to the (y, z)-coordinate system can be extracted from the sketches in Fig. (A.2),

$$\begin{bmatrix} y(s, v) \\ z(s, v) \end{bmatrix} = \begin{bmatrix} y_0(s) \\ z_0(s) \end{bmatrix} + \begin{bmatrix} v \cos \theta(s) \\ v \sin \theta(s) \end{bmatrix}, \tag{A.5}$$

where $(y_0(s), (z_0(s))$ are coordinates of the point A on the trajectory that is defined by arc-length coordinate s. Equation (A.4) can be expressed as a dot-product of two $(2, 1)$-vectors,

$$\frac{\partial}{\partial v} \begin{bmatrix} y(s, v) \\ z(s, v) \end{bmatrix} \cdot \frac{\partial}{\partial s} \begin{bmatrix} y(s, v) \\ z(s, v) \end{bmatrix} = 0. \tag{A.6}$$

Inserting Eq. (A.5) into Eq. (A.6), we obtain

$$\begin{bmatrix} \cos \theta(s) \\ \sin \theta(s) \end{bmatrix} \cdot \left(\mathbf{T}(s) + \begin{bmatrix} -v \sin \theta(s) \frac{\partial \theta(s)}{\partial s} \\ v \cos \theta(s) \frac{\partial \theta(s)}{\partial s} \end{bmatrix} \right) = \mathbf{N}(s) \cdot \mathbf{T}(s) \left(1 + v \frac{\partial \theta(s)}{\partial s} \right) = 0, \tag{A.7}$$

where $\mathbf{N}(s)$ denotes the unit normal vector in point A on the trajectory, which in case of plane trajectories is parallel to vector $\mathbf{V}(s)$. Since the dot product of the normal and the tangent vector is always equal to zero, Eq. (A.7) is always fulfilled, and $\boldsymbol{\mu}'(u, v, s)$ are thus diagonal tensors.

A.3 Time-stepping

We have already shown in Appendix A.1 that no local center of curvature of the trajectory is allowed to be in the computational domain in order to maintain the bijectivity of the space transformation defined by Eq. 3.3 — this is ensured by limiting the ranges of u- and v-coordinates. In addition, if the computational domain border is too close to a local center of curvature, another problem might arise because some entries of the material property tensors can get values close to zero. This results in small time steps of the corresponding time-domain simulation

and extends the overall simulation time greatly. For illustration and similarly to Appendix A.1, we discuss a $90°$-bend in the (y, z)-plane, see Fig. A.3. The trajectory with a bend radius r is given by

$$x_0 = 0, \quad y_0 = r \cos(t), \quad z_0 = r \sin(t), \quad t \in [0, \pi/2]. \tag{A.8}$$

The coordinate $s = rt$ is the arc-length of the trajectory. Since the u-axis is parallel to the x-axis and the v-axis is always in the plane of the trajectory, we can write the one-to-one correspondence between the (x, y, z)- and (u, v, s)-spaces, see Fig. A.3(b),

$$\begin{aligned}
x(u, v, s) &= u, \\
y(u, v, s) &= -(r - v) \cos(s/r), \\
z(u, v, s) &= (r - v) \sin(s/r).
\end{aligned} \tag{A.9}$$

The Jacobian $\mathbf{J}$ of the function $f(x, y, z) = (u, v, s)$ can be found as the inverse of the Jacobian of the function $f^{-1}(u, v, s) = (x, y, z)$,

$$\mathbf{J} = \begin{bmatrix} \partial x/\partial u & \partial x/\partial v & \partial x/\partial s \\ \partial y/\partial u & \partial y/\partial v & \partial y/\partial s \\ \partial z/\partial u & \partial z/\partial v & \partial z/\partial s \end{bmatrix}^{-1} = \begin{bmatrix} 1 & 0 & 0 \\ 0 & \cos\left(\frac{s}{r}\right) & -\sin\left(\frac{s}{r}\right) \\ 0 & \frac{r}{r-v}\sin\left(\frac{s}{r}\right) & \frac{r}{r-v}\cos\left(\frac{s}{r}\right) \end{bmatrix}^{-1} \tag{A.10}$$

$$= \begin{bmatrix} -1 & 0 & 0 \\ 0 & -\cos\left(\frac{s}{r}\right) & -\sin\left(\frac{s}{r}\right) \\ 0 & -\frac{r}{r-v}\sin\left(\frac{s}{r}\right) & \frac{r}{r-v}\cos\left(\frac{s}{r}\right) \end{bmatrix}. \tag{A.11}$$

Plugging-in the this result into Eq. A.2, we get

$$\boldsymbol{\varepsilon}'(u, v, s) = \boldsymbol{\varepsilon}(x, y, z) \begin{bmatrix} \frac{r-v}{r} & 0 & 0 \\ 0 & \frac{r-v}{r} & 0 \\ 0 & 0 & \frac{r}{r-v} \end{bmatrix} = \begin{bmatrix} \varepsilon_{1,1} & 0 & 0 \\ 0 & \varepsilon_{2,2} & 0 \\ 0 & 0 & \varepsilon_{3,3} \end{bmatrix}. \tag{A.12}$$
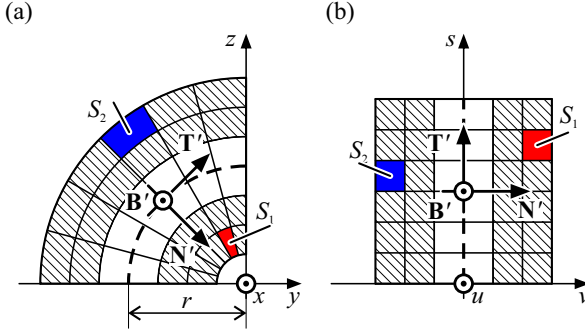
Figure A.3: Illustration of the space transformation for a 90°-bend. (a) The freeform waveguides in the (y, z)-plane of (x, y, z)-space. (b) The same freeform waveguide in the (v, s)-plane of (u, v, s)-space. In (u, v, s)-space, the 90°-bend is straightened. It is divided into squares by taking equidistant divisions along the s-axis (slicing) and along the v-axis. The squares in (u, v, s)-space correspond to sections bounded by two line segments and two concentric arcs in (x, y, z)-space. The areas of these sections differ along the radial coordinate and are smaller on the inner side and larger on the outer side of the bend. Areas close to the origin tend to zero, and mapping these sections to finite size squares in (u, v, s)-space causes two entries of tensors of material properties to tend to zero, see Eq. A.12. This leads to a small time step of the corresponding FDTD simulation and to a long simulation time. Areas of sections far from the origin tend to infinity, and mapping infinite sections to finite size squares in (u, v, s)-space also causes one of the tensor entries of material properties to tend to zero. These cases are however not critical, since the space far away from the trajectory is not of interest in the TO approach.

A similar result holds for $\boldsymbol{\mu}'$. When v approaches r, $\varepsilon_{1,1}$ and $\varepsilon_{2,2}$ ($\mu_{1,1}$ and $\mu_{2,2}$) tend to 0, causing the maximum phase velocity to tend to infinity. According to the Courant-Friedrichs-Lewy stability condition Eq. 3.7, the maximal time step tends to zero, and the total simulation time approaches infinity. On the outer side of the bend, for $v < 0$, tensor entries $\varepsilon_{3,3}$ and $\mu_{3,3}$ are more problematic. However, they only tend to zero if $|-v| \gg r$. This is, however, not of practical interest.

[end of the content based on appendices of manuscript [J1]]

B Graph theory and switch-and-select circuits

The content of Appendix B was taken from Appendices of paper [J3], and it has been modified to fit the formatting rules of this thesis.

Aleksandar Nesic, Matthias Blaicher, Tobias Hoose, Andreas Hofmann, Matthias Lauermann, Yasar Kutuvantavida, Martin Nöllenburg, Sebastian Randel, Wolfgang Freude, and Christian Koos

[start of appendices of publication [J3]]

B.1 Graph theory

In this section, we shortly summarize a few *definitions* from graph theory that are used in the graph-theoretical analysis of SAS circuits in Section 4.3 and Appendices B.2 and B.3.

1. A *graph $G\,(N, E)$* is defined as an ordered pair consisting of a set of *vertices N* and a set of *edges E*, which are two-element subsets of N (one edge connects two vertices). The number of vertices and edges is $|N|$ and $|E|$, respectively. The notation $|X|$ denotes the *cardinality* (number of elements) of a set X.

2. A *bipartite graph* $G(M, N, E)$ consists of two sets of vertices M and N and a set of edges E, such that there are no edges between two vertices that are in the same set.

3. In a *complete graph* $G(N, E)$, each vertex of set N is connected by an edge to all other vertices of the same set. The number of vertices is $|N| = n$, and the number of edges is $|E| = n(n-1)/2$. Such a graph is denoted by K_n.

4. In a complete bipartite graph $G(M, N, E)$, each vertex of set M is connected by an edge to each vertex of the second vertex set N. The number of vertices is $|M| + |N| = m + n$, and the number of edges is $|E| = mn$. Such a graph is denoted by $K_{m,n}$.

5. A *planar graph* can be drawn in a plane without *edge crossings*. From Kuratowski's theorem [150], it follows that a complete graph K_n is planar if $n \leq 4$, and a complete bipartite graph $K_{m,n}$ is planar if $m \leq 2$ or $n \leq 2$.

6. A *maximum planar graph* would become a *non-planar* graph by adding one additional edge.

7. A *plane embedding* is a drawing of a planar graph in a plane without edge crossings.

8. A plane embedding divides the plane into distinct regions called *faces*. All faces are bounded by edges except for the single *outer face* which extends to infinity. In a *maximum planar graph plane embedding*, each face is defined by three edges. In a *bipartite maximum planar graph plane embedding*, each face is defined by four edges.

9. The *crossing number* $\text{cr}(G)$ of a graph G counts the minimum number of edge crossings, taking into account all possible drawings of G in a plane. The crossing number of a planar graph is zero.

10. The *outerplanar crossing number* $\text{cr}^*(G)$ of a graph G counts the minimum number of edge crossings, taking into account all possible drawings of G in

a plane, such that all vertices of G lie on a closed boundary curve, and all edges of G are drawn inside the area bounded by the boundary curve.

11. The *local crossing number* lcr (G) of a graph G is the minimum of the maximum number of crossings along any edge of G, taking into account all possible drawings of G in a plane.

12. The *local crossing number of a graph drawing* counts the maximum number of edge crossings along any edge for that particular drawing.

13. A *subgraph* of a graph G is a graph consisting of sets of vertices and edges that are subsets of sets of vertices and edges of G.

14. A *spanning maximum planar subgraph* of a graph G is a *maximum planar subgraph* of G that contains all vertices of G.

For more information on general graph theory, please refer to [151]. Crossing number problems are discussed in more detail in [152].

B.2 Graph-theoretical analysis of surface-coupled $m \times n$ SAS circuits

As previously mentioned, a surface-coupled $m \times n$ circuit with $1 \times n$ and $m \times 1$ LE switches at the input and output ports can be represented by a complete bipartite graph $K_{m,n}$. The conjectured crossing number of $K_{m,n}$ is given by [66]

$$\mathrm{cr}_{\mathrm{conj.}}\left(K_{m,n}\right) = \eta_{m,n}^{(\mathrm{surf})} = \left\lfloor \frac{m}{2} \right\rfloor \left\lfloor \frac{n}{2} \right\rfloor \left\lfloor \frac{m-1}{2} \right\rfloor \left\lfloor \frac{n-1}{2} \right\rfloor, \tag{B.1}$$

which in case $m = n$ reduces to Eq. (4.2). For a complete bipartite graph $K_{m,n}$, the construction of a drawing that results in the conjectured minimum number of crossings given by Eq. B.1 is proposed in [66] and illustrated in Fig. B.1(a) for the case of $K_{5,5}$. In a first step, all vertices of set M are placed on the x-axis, whereas the vertices of set N are placed on the y-axis of the 2D Cartesian

coordinate system. This placement is done such that the number of vertices on both positive and negative parts of the x and y-axes is as much equal as possible. Achieving exactly equal numbers is possible only if m and n are even — if any of them is odd, we will put one vertex more on the positive side of the corresponding axis. Therefore, the x-coordinates of the vertices of set M are, $-\lfloor m/2 \rfloor, -\lfloor m/2 \rfloor + 1, ..., -1, 1, ..., \lceil m/2 \rceil$ and the corresponding vertices are labelled with $v_{M,-\lfloor m/2 \rfloor}, v_{M,-\lfloor m/2 \rfloor+1}, ..., v_{M,-1}, v_{M,1}, ..., v_{M,\lceil m/2 \rceil}$. Similarly, the y-coordinates of the vertices of set N are, $-\lfloor n/2 \rfloor, -\lfloor n/2 \rfloor + 1, ..., -1, 1, ..., \lceil n/2 \rceil$, and the corresponding vertices are labelled with $v_{N,-\lfloor n/2 \rfloor}, v_{N,-\lfloor n/2 \rfloor+1}, ..., v_{N,-1}, v_{N,1}, ..., v_{N,\lceil n/2 \rceil}$. Finally, all vertices of set M are connected by mn line segments to all vertices of set N.

In order to find the local crossing number of such drawing it is enough to analyze the 1st quadrant of the 2D Cartesian system, since it contains the largest number of vertices and edges, and since all edges are completely drawn in single quadrants. The two edges that cross the largest number of other edges, $\{v_{N,\lceil n/2 \rceil}, v_{M,1}\}$ and $\{v_{N,1}, v_{M,\lceil m/2 \rceil}\}$, are drawn in blue in Fig. B.1(a). It can be easily seen that edge $\{v_{N,\lceil n/2 \rceil}, v_{M,1}\}$ must cross all edges that connect $\lceil n/2 \rceil - 1$ vertices $v_{N,1}, ..., v_{N,\lceil n/2 \rceil-1}$ to $\lceil m/2 \rceil - 1$ vertices $v_{M,2}, ..., v_{M,\lceil m/2 \rceil}$. Similarly, edge $\{v_{N,1}, v_{M,\lceil m/2 \rceil}\}$ must cross all edges that connect $\lceil n/2 \rceil - 1$ vertices $v_{N,2}, ..., v_{N,\lceil n/2 \rceil}$ to $\lceil m/2 \rceil - 1$ vertices $v_{M,1}, ..., v_{M,\lceil m/2 \rceil-1}$ Therefore, the local crossing number of this drawing amounts to

$$\mathrm{lcr}_{\text{conj. drawing}}(K_{m,n}) = \xi_{m,n}^{(\text{surf})} = \left(\left\lceil \frac{m}{2} \right\rceil - 1 \right) \left(\left\lceil \frac{n}{2} \right\rceil - 1 \right). \tag{B.2}$$

For $m = n$, this reduces to Eq. (4.5).

To analyze the number of necessary WOP, we introduce a term 3D edge, which is an edge that is not restricted to the plane but can be routed in 3D, and we will use it to model a WOP. A WOP does not directly connect two optical devices on the PIC, but rather links two ends of two planar waveguides, each of which is connected to an optical device at its respective other end. The connections of
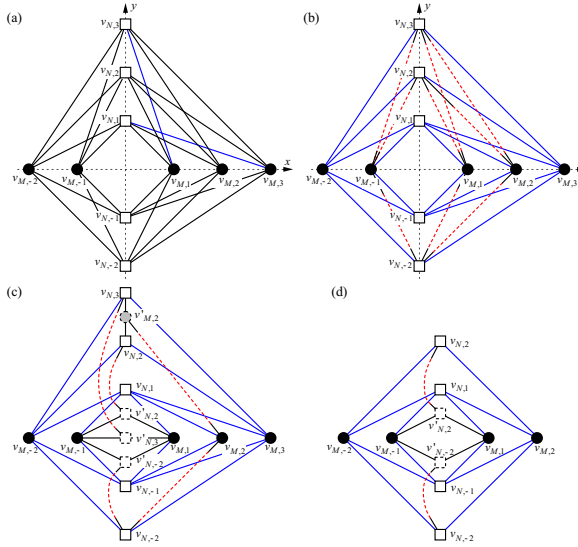
Figure B.1: Different graph drawings of a surface-coupled 5×5 and 4×4 SAS circuit: (a) Graph drawing of a 5×5 SAS circuit where 1×5 and 5×1 switches at the input and output ports are realized as LE. The circuit is modeled by a complete bipartite graph $K_{5,5}$, and the arrangement of vertices of sets M and N is such that the drawing results in the number of crossings equal to the conjectured crossing number given by Eq. (B.1). The two edges depicted in blue are the edges with the maximum number of crossings, which determine the local crossing number of this particular graph drawing, as given by Eq. (B.2). (b) Planar-edge-crossing-free graph representation of the same circuit. The edges depicted in blue represent a spanning maximum planar subgraph of $K_{5,5}$. The remaining edges are realized with help of 3D edges (representing WOP) depicted as dashed red lines, which are routed outside the plane of the drawing and avoid crossings with the planar edges. Each 3D edge connects to a pair of planar edges depicted in black, that are linked to vertices at the respective other end. (c) If the 1×5 and 5×1 switches at the input and output ports are realized as BT of 1×2 and 2×1 switches, the number of necessary 3D edges can be reduced by splitting the vertices of the original $K_{5,5}$ and placing them into appropriate faces of the spanning maximum planar subgraph depicted in blue. The white dashed squares represent 1×2 switches, while the dashed circle with gray filling represents a 2×1 switch. This approach allows to replace a pair of 3D edges by a single one. In case where both m and n are odd, the number of missing edges is also odd, and one missing edge (in this case $\{v_{N,-2}, v_{M,-2}\}$) must be realized with help of one single 3D edge. (d) Graph drawing of a 4×4 SAS circuit, analogous to the case described in (c). In case at least one of the numbers m or n is even, the number of 3D edges can be reduced by a factor of 2 compared to the case when $1 \times n$ and $m \times 1$ switches are realized as LE. For our experimental demonstration, we used the PIC layout displayed in Fig. 4.2(d), which was obtained in a similar way as Fig. B.1(d), with the difference that the auxiliary vertices (1×2 switches) in Fig. 4.2(d) were placed in the outer face of the spanning maximum planar subgraph rather than in its inner face, as displayed here.

WOP and planar waveguides are an analog to metallic vias that connect metallic wires in different layers of an electric printed circuits board (PCB). In the graph representation, a WOP is modelled by a 3D edge that does not directly connect to two vertices on the plane, but links two planar edges, each of which is connected to another vertex at its respective other end. In order to estimate the number of necessary 3D edges, we first construct a spanning maximum planar subgraph of $K_{m,n}$, which has $2m + 2n - 4$ edges [133]. We do it by connecting each of the vertices $v_{M,-\lfloor m/2 \rfloor}, v_{M,\lfloor m/2 \rfloor}, v_{N,-1}$, and $v_{N,1}$ to each vertex of the opposite set, see Fig. B.1(b). The remaining

$$\mu_{m,n}^{(\text{surf})} = mn - (2m + 2n - 4) = (m - 2)(n - 2) \tag{B.3}$$

edges can be realized using 3D edges. For $m = n$, Eq. (B.3) reduces to Eq. (4.3). The concept is illustrated in Fig. B.1(b) for the case of $K_{5,5}$. The edges of the spanning maximum planar subgraph are depicted in blue, the 3D edges in red (dashed), while the planar edges that connect the 3D edges to the vertices are depicted in black. The red dashed lines are, in fact, vertical projections of 3D edges on the 2D drawing plane.

Note that the planar projections of the 3D edges on the drawing plane may cross each other. This, however, does not mean that the two 3D edges cross in 3D space — two freeform WOP can always be 3D-printed such that one passes over the other, and the corresponding 3D edges can be routed analogously. Furthermore, by appropriate routing of the planar and 3D edges, the crossings of projections of 3D edges on the drawing plane can be avoided. Figure B.1(b) shows how a possible crossing of projections of two 3D edges between pairs of vertices $\{v_{N,2}, v_{M,2}\}$ and $\{v_{N,3}, v_{M,1}\}$ has been avoided by making the planar waveguide that connects $v_{N,2}$ to the corresponding 3D edge sufficiently long such that it passes underneath the 3D edge between the pair of vertices $\{v_{N,3}, v_{M,1}\}$. We believe that this approach might be generalized to avoid crossings of projections of 3D edges for general

complete bipartite graphs $K_{m,n}$ — a general proof would need further investigation and is beyond the scope of this paper.

If the $1 \times n$ and $m \times 1$ switches at the input and output ports are realized as BT of 1×2 and 2×1 switches rather than as LE, we can further reduce the number of 3D edges. We will split the analysis into two cases: when both m and n are odd, and when at least one of them is even. Furthermore, we will only analyze cases where both m and n are ≥ 3 since otherwise, according to Kuratowski's theorem [150], the complete bipartite graph $K_{m,n}$ is planar. If both m and n are odd, we do the following steps:

Step 1: Construct the spanning maximum planar subgraph of $K_{m,n}$ as described above. The edges of this subgraph are depicted in blue in Fig. B.1(c) for the case of $K_{5,5}$ ($m = n = 5$). This subgraph has all faces determined by four vertices (two from set M and two from set N) and four edges. There are $(m-3)$ vertices of set M whose x-coordinates lie between $-\lfloor m/2 \rfloor + 1$ and $\lceil m/2 \rceil - 2$ inclusive, and they can be divided into $(m-3)/2$ distinct two-element subsets of vertices (because $m-3$ is even, and therefore divisible by two): $\{v_{M,-\lfloor m/2 \rfloor+1}, v_{M,-\lfloor m/2 \rfloor+2}\}, \{v_{M,-\lfloor m/2 \rfloor+3}, v_{M,-\lfloor m/2 \rfloor+4}\}, ..., \{v_{M,\lceil m/2 \rceil-3}, v_{M,\lceil m/2 \rceil-2}\}$. Each of these $(m-3)/2$ pairs of vertices of set M together with the pair of vertices $v_{N,-1}, v_{N,1}$ of set N, define $(m-3)/2$ faces: $\{v_{M,-\lfloor m/2 \rfloor+1}, v_{N,-1}, v_{M,-\lfloor m/2 \rfloor+2}, v_{N,1}\}, \{v_{M,-\lfloor m/2 \rfloor+3}, v_{N,-1}, v_{M,-\lfloor m/2 \rfloor+4}, v_{N,1}\}, ..., \{v_{M,\lceil m/2 \rceil-3}, v_{N,-1}, v_{M,\lceil m/2 \rceil-2}, v_{N,1}\}$. For $m = 3$ there are no such faces. For $m = 5$, there is only one such face $\{v_{M,-\lfloor m/2 \rfloor+1}, v_{N,-1}, v_{M,\lceil m/2 \rceil-2}, v_{N,1}\} = \{v_{M,-1}, v_{N,-1}, v_{M,1}, v_{N,1}\}$, see Fig. B.1(c). Note that the results of the expressions $-\lfloor m/2 \rfloor + i$ and $-\lceil m/2 \rceil - j$ in the subscripts of labels of vertices of set M indicate the x-coordinates of the vertices. Since there is no vertex at $x = 0$, not a single expression is allowed to result in zero. Therefore, we restrict the values of integers i and j to $i = 1, 2, ..., \lfloor m/2 \rfloor - 1$ and $j = \lceil m/2 \rceil - 1, \lceil m/2 \rceil - 2, ..., 2$ (the expression $-\lfloor m/2 \rfloor + i$ is used for vertices on the negative side of the x-axis, while the expression $\lceil m/2 \rceil - j$ is used for vertices on the positive side of the x-axis).

Step 2: Let us put an auxiliary vertex $v'_{N,\lceil n/2 \rceil}$ inside the face defined by vertices $\{v_{M,-\lfloor m/2 \rfloor+1}, v_{N,-1}, v_{M,-\lfloor m/2 \rfloor+2}, v_{N,1}\}$. We can connect the auxiliary vertex $v'_{N,\lceil n/2 \rceil}$ to vertex $v_{N,\lceil n/2 \rceil}$ with a 3D edge, and the same auxiliary vertex to vertices $v_{M,-\lfloor m/2 \rfloor+1}$ and $v_{M,-\lfloor m/2 \rfloor+2}$ with two planar edges. The auxiliary vertex is the place where we put a 2×1 switch, which is a part of the BT $m \times 1$ switch at the vertex $v_{N,\lceil n/2 \rceil}$. In this way, we can replace two 3D edges that would otherwise separately connect vertex $v_{N,\lceil n/2 \rceil}$ to vertices $v_{M,-\lfloor m/2 \rfloor+1}$ and $v_{M,-\lfloor m/2 \rfloor+2}$. The auxiliary vertex $v'_{N,\lceil n/2 \rceil}$ and the two planar edges that connect it to vertices $v_{M,-\lfloor m/2 \rfloor+1}$ and $v_{M,-\lfloor m/2 \rfloor+2}$ split the original face $\{v_{M,-\lfloor m/2 \rfloor+1}, v_{N,-1}, v_{M,-\lfloor m/2 \rfloor+2}, v_{N,1}\}$ into two faces $\{v_{M,-\lfloor m/2 \rfloor+1}, v_{N,-1}, v_{M,-\lfloor m/2 \rfloor+2}, v'_{N,\lceil n/2 \rceil}\}$ and $\{v_{M,-\lfloor m/2 \rfloor+1}, v_{N,1}, v_{M,-\lfloor m/2 \rfloor+2}, v'_{N,\lceil n/2 \rceil}\}$. We put an additional auxiliary vertex $v'_{N,\lceil n/2 \rceil-1}$ to any of the two new faces, and we connect it to vertex $v_{N,\lceil n/2 \rceil-1}$ with a 3D edge and to vertices $v_{M,-\lfloor m/2 \rfloor+1}$ and $v_{M,-\lfloor m/2 \rfloor+2}$ with two planar edges. We repeat the procedure for all vertices of set N, except for vertices $v_{N,-1}$ and $vN, 1$, which are already connected to all vertices of set M. In this way, we connect both vertices of the pair $\{v_{M,-\lfloor m/2 \rfloor+1}, v_{M,-\lfloor m/2 \rfloor+2}\}$ to all vertices of set N. We apply the same algorithm to connect the pairs of vertices $\{v_{M,-\lfloor m/2 \rfloor+3}, v_{M,-\lfloor m/2 \rfloor+4}\}, ...,$ $\{v_{M,-\lceil m/2 \rceil-3}, v_{M,-\lceil m/2 \rceil-2}\}$ to all vertices of set N. This step has been illustrated in Fig. B.1(c) where auxiliary vertices $v'_{N,3}$, $v'_{N,2}$, and $v'_{N,-2}$ have been placed inside the face $\{v_{M,-1}, v_{N,-1}, v_{M,1}, v_{N,1}\}$, connected to vertices $v_{N,3}$, $v_{N,2}$, and $v_{N,-2}$ by 3D edges, respectively, and to $v_{M,1}$ and $v_{M,-1}$ by planar edges. For $m = 3$, Step 2 is skipped.

Step 3: So far, we connected all vertices of set M to all vertices of set N, except for vertex $v_{M,\lceil m/2 \rceil-1}$ that is connected only to $v_{N,-1}$ and $v_{N,1}$ and still needs to be connected to the remaining $(n-2)$ vertices of set N. There are $\lceil n/2 \rceil - 1$ such vertices on the positive side of the y-axis: $v_{N,\lceil n/2 \rceil}, v_{N,\lceil n/2 \rceil-1}, ..., v_{N,2}$ and $\lfloor n/2 \rfloor - 1$ on the negative side of the y-axis: $v_{N,-2}, v_{N,-3}, ..., v_{N,\lfloor n/2 \rfloor}$. Depending on n, one of these two numbers is even, and the other is odd. If $\lceil n/2 \rceil - 1$ is even and $\lfloor n/2 \rfloor - 1$ is odd, then each of the following pairs of vertices $\{v_{N,\lceil n/2 \rceil}, v_{N,\lceil n/2 \rceil-1}\}, ..., \{v_{N,3}, v_{N,2}\}$, $\{v_{N,-2}, v_{N,-3}\}, ..., \{v_{N,-\lfloor n/2 \rfloor+2}, v_{N,-\lfloor n/2 \rfloor+1}\}$ together with the pair of vertices

$\{v_{M,-\lfloor m/2 \rfloor}, v_{M,\lceil m/2 \rceil}\}$ define one face. In each of these faces, we can place one auxiliary vertex $v'_{M,\lceil m/2 \rceil-1}, v''_{M,\lceil m/2 \rceil-1}, v'''_{M,\lceil m/2 \rceil-1}, ...,$ see Fig. B.1(c), where there is only one such auxiliary vertex $v'_{M,\lceil m/2 \rceil-1} = v'_{M,2}$. Each of these auxiliary vertices can be connected to $v_{M,\lceil m/2 \rceil-1}$ by a 3D edge and to the respective pair of vertices of set N (that define the face in which the auxiliary vertex is placed) by two planar edges. After this step, there will be only one missing edge between vertices $v_{M,\lceil m/2 \rceil-1}$ and $v_{N,-\lfloor n/2 \rfloor}$, and we directly connect these two vertices by a single 3D edge, see Fig. B.1(c). Similarly, if $\lceil n/2 \rceil - 1$ is odd and $\lfloor n/2 \rfloor - 1$ is even, we can group the vertices of set N into pairs as $\{v_{N,\lceil n/2 \rceil-1}, v_{N,\lceil n/2 \rceil-2}\}, ..., \{v_{N,3}, v_{N,2}\},$ $\{v_{N,-2}, v_{N,-3}\}, ..., \{v_{N,-\lfloor n/2 \rfloor+1}, v_{N,-\lfloor n/2 \rfloor}\}$, which would define faces together with the pair of vertices $\{v_{M,-\lfloor m/2 \rfloor}, v_{M,\lceil m/2 \rceil}\}$. After placing and connecting auxiliary vertices as described, the only missing edge would be between $v_{M,\lceil m/2 \rceil-1}$ and $v_{N,-\lceil n/2 \rceil}$, and we would connect them by one 3D edge.

The case when at least one of the numbers m and n is even is simpler. We can assume without loss of generality that m is even and n is odd. By constructing the spanning maximum planar subgraph of $K_{m,n}$ as described above, we will get a subgraph where each of the following $(m-2)/2$ pairs of vertices $\{v_{M,-\lfloor m/2 \rfloor+1}, v_{M,-\lfloor m/2 \rfloor+2}\},$ $\{v_{M,-\lfloor m/2 \rfloor+3}, v_{M,-\lfloor m/2 \rfloor+4}\}, ..., \{v_{M,\lceil m/2 \rceil-2}, v_{M,\lceil m/2 \rceil-1}\}$ together with the pair of vertices $\{v_{N,-1}, v_{N,1}\}$ define one face. After performing Step 2 as described above, we will connect all vertices of set M to all vertices of set N. Figure B.1(d) shows an example of the result of the algorithm for the case of $K_{4,4}$.

The described algorithm allows to replace two missing planar edges by one 3D edge. The number of necessary 3D edges hence amounts to

$$\mu_{m,n}^{\text{(surf, BT)}} = \left\lceil \frac{(m-2)(n-2)}{2} \right\rceil, \tag{B.4}$$

which reduces to Eq. (4.4) for $m = n$. The ceiling function in Eq. (B.4) is used to include the case when the number of missing edges is odd (both m and n are odd) and not divisible by two (one single missing edge needs to be realized with one single 3D edge). This algorithm is just an example and not the unique way of

constructing a layout that results in the number of 3D edges given by Eq. (B.4): For example, in Step 1 we could construct the spanning maximum planar subgraph in a different way and then modify Steps 2 and 3 accordingly.

It should be pointed out that Eq. (B.4) does not necessarily give the minimum number of necessary 3D edges, but an upper bound. In our construction we started from the spanning maximum planar subgraph, and we split some vertices in two by introducing auxiliary vertices. We did, however, not show that the spanning maximum planar subgraph of $K_{m,n}$ is the optimal way to start with. We could have also started with a non-maximum planar subgraph and could have used larger split ratio switches $1 \times n'$, $n' < n$ and $1 \times m'$, $m' < m$, and place them in the auxiliary vertices. Furthermore, the graph model of the device where $1 \times n$ and $m \times 1$ switches at the input and output ports are realized as BT of 1×2 and 2×1 switches, is not a complete bipartite graph $K_{m,n}$. The crossing number of the SAS circuit realized with such an approach is subject to ongoing investigations.

B.3 Facet-coupled SAS circuits

B.3.1 Facet-coupled SAS realized in single-layer and hybrid 2D/3D photonic integration

For facet-coupled SAS circuits, all input and output ports are implemented by waveguide facets arranged along the chip boundaries, making it impossible to route waveguides "behind" the ports, i.e., between the ports and the chip boundary. In the graph drawing of the circuit, all vertices representing input and output ports must hence be placed on a closed curve that represents the boundary of the chip surface, and no waveguide (graph edge) routing outside the area enclosed by the curve is allowed. In addition, in contrast to surface coupling, the graph of a facet-coupled SAS is not anymore a complete bipartite graph: For the case of surface coupling, a port and the associated $1 \times n$ or $m \times 1$ switch can be combined into a single vertex, whereas facet-coupled circuits must be represented by a first kind of vertices for the switches and a second kind of vertices for the ports, which

must be placed onto the boundary curve. Every port vertex must be connected to the associated switch by a graph edge that represents the *access* waveguide. This results in a *3-partite* graph, which comprises three parties of vertices represented by the ports, the $1 \times n$ switches, and the $m \times 1$ switches, and which is not complete. For a general description of facet-coupled SAS circuits, we can hence not resort any more to the existing theory of complete bipartite graphs. This renders theoretical assessment of the topologies more diffcult and requires simplifying assumptions for quantifying the numbers of WGX or WOP. Nevertheless, we believe that non-planar facet-coupled SAS circuits can also greatly benefit from replacing WGX by WOP.

To support this claim, we first consider the basic non-optimized representation of a 4×4 SAS circuit, see Fig. B.2(a). This representation relies on the same simplistic approach as the surface-coupled SAS circuit that is sketched in Fig. 4.2(a). In this approach, each pair of vertices of set M is connected by four edges to each pair of vertices of set N, and the four edges make exactly one crossing. The number of crossings is therefore equal to the product of numbers of ways to choose two-element subsets of M and N and amounts to

$$\eta_{m,n}^{\text{(facet, basic)}} = \binom{m}{2}\binom{n}{2} = \left(\frac{m\,(m-1)}{2}\right)\left(\frac{n\,(n-1)}{2}\right), \tag{B.5}$$

which reduces to Eq. (4.1) for the case of $m = n$. Interleaving the input and output ports along the boundary line allows to reduce this number, see Fig. B.2(b). In this case, we can simplify the theoretical assessment to finding the outerplanar crossing number of a complete bipartite graph. This can be seen if we look at the blue dashed line in Fig. B.2(b): All vertices representing $1 \times n$ and $m \times 1$ switches are placed on it, and all edges are routed inside the area bounded by it. Note that this implementation is not yet optimal since it does not exploit the possibility to reduce the number of WGX by routing waveguides between the ports and the corresponding $1 \times n$ or $m \times 1$ switches. For the case of n being an integer multiple of m, the outerplanar crossing number of a complete bipartite graph $K_{m,n}$
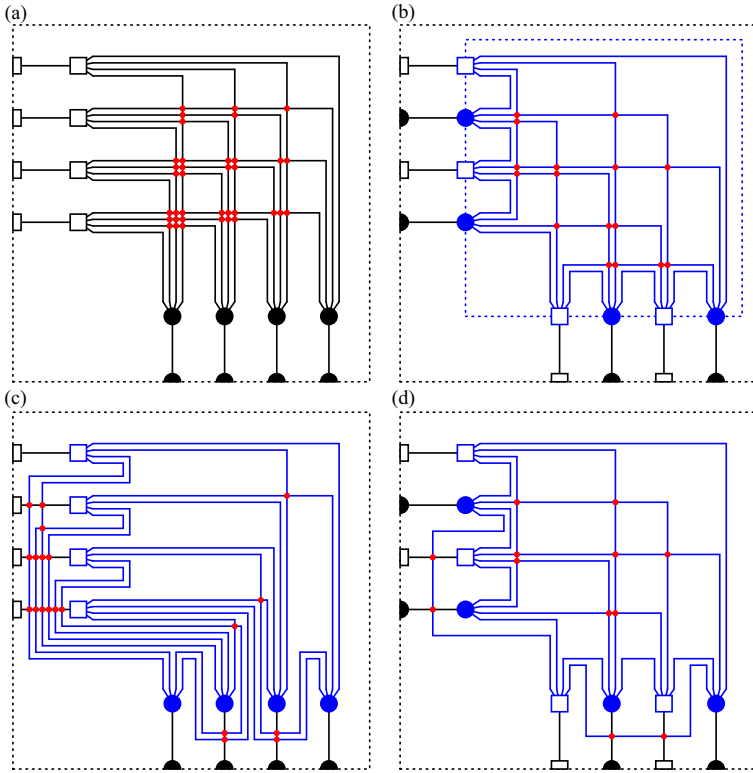
Figure B.2: Different graph drawings of a facet-coupled 4×4 SAS circuit: A first set of vertices (rectangles and half circles) is used to represent facet-coupled optical input and output ports, and a second kind of vertices (squares and full circles) represents the $1 \times n$ or $m \times 1$ switches. Each port vertex is connected to the associated switch vertex by a graph edge that represents the *access* waveguide (a) Simplistic non-optimum graph representation based on the same approach as the surface-coupled SAS circuit shown in Fig. 4.2(a). Input and output ports are clustered into two groups of neighboring vertices along the chip boundary. For a 4×4 SAS circuit, 36 WGX are required. (b) By interleaving the input and output ports along the chip boundary, the number of crossings can be reduced, leading to a total number of 16 WGX for a 4×4 SAS circuit. (c) The number of crossings can also be reduced by allowing routing of waveguides between the ports and the corresponding $1 \times n$ and $n \times 1$ switches, leading to a total number of 20 WGX for the depicted graph drawing. (d) Circuit layout obtained by combining interleaving of input and output ports with routing of waveguides between the ports and the corresponding switches, leading to a total number of 12 WGX.

is obtained when the vertices of set M are evenly interleaved between the vertices of set N and amounts to [153]

$$\eta_{m,n}^{(\text{facet})} = \frac{1}{12} n \, (m-1) \, (2mn - 3m - n) \, . \tag{B.6}$$

For the case $m = n$, this reduces to

$$\eta_{n,n}^{(\text{facet})} = \frac{1}{6} n^2 \, (n-1) \, (n-2) \, , \tag{B.7}$$

Which scales with $n^4/6$ for large n. The associated numbers of WGX for switches implemented as LE are listed in the second column of Table B.1. Further layout optimization steps may involve routing of waveguides between the ports and the corresponding switches, possibly in combination with interleaving of the ports along the chip boundary, see Figs. B.2(c) and B.2(d). Even though we are not aware of any relations specifying the exact crossing numbers of these graphs, we may still use the number of WGX in the associated surface-coupled SAS as a lower bound. This can be understood by observing that both implementations in Figs. B.2(c) and B.2(d). contain a maximum bipartite subgraph (indicated in blue) which is equivalent to that of the corresponding surface-coupled circuit, Fig. 4.2(b), and which is complemented by additional crossings caused by the access waveguides. The number of WGX still scales with at least $n^4/16$, see Eq. (4.2). Similarly to the case of surface-coupled SAS, disaggregating the $1 \times n$ and $m \times 1$ switches into BT of 1×2 switches might reduce the number of WGX — this aspect is still under investigation. For the remainder of this section, we rely on Eq. (B.7) for determining the number of WGX in the facet-coupled $n \times n$ SAS circuit.

For 2D/3D hybrid implementations, the number of WOP in facet-coupled SAS circuits was analyzed based on the simplistic layout shown in Fig. B.2(a) for cases of LE switches and BT cascaded 1×2 switches, see Figs. B.3(a) and B.3(b).

Table B.1: Quantitative comparison of $n \times n$ facet-coupled switch-and-select (SAS) circuit implementations based on WGX in single-layer circuits and on WOP in hybrid 2D/3D photonic integration. The total number of WGX (second column) increases approximately in proportion to $n^4/6$, whereas the number of WOP scales with n^2 for the case of LE switches (third column) and with $n^2/2$ in case the switches are decomposed into BT of 1×2 and 2×1 switches (fourth column). The maximum number of WGX along an optical path increases approximately in proportion to $n^2/2$ for the case of LE switches (fifth column), whereas the maximum number of WOP along an optical path is one in both cases of LE and BT switches (sixth column).

SAS ($n \times n$)	Total number			Maximum number along any optical path	
	WGX (LE)	WOP (LE)	WOP (BT)	WGX (LE)	WOP (LE & BT)
4×4	16	9	5	4	1
8×8	448	49	25	24	1
16×16	8 960	225	113	112	1
32×32	158 720	961	481	480	1
64×64	2 666 496	3 969	1 985	1 984	1

Mathematical details can be found in Appendix B.3.2. For LE switches, this leads to a total WOP number of

$$\mu_{n,n}^{(\text{facet})} = (m-1)(n-1),$$ (B.8)

which reduces to $(n-1)/2$ for $m = n$. For BT switches, the number of WOP amounts to

$$\mu_{n,n}^{(\text{facet, BT})} = \left\lceil \frac{(m-1)(n-1)}{2} \right\rceil,$$ (B.9)

i.e., $\lceil (n-1)^2/2 \rceil$ for $m = n$. Hence, in both cases, the number of WOP in the facet-coupled hybrid 2D/3D implementation scales much more favorably than the number of WGX in the corresponding single-layer SAS circuit, see third and fourth column of Table B.1. Note that this number represents an upper bound for the number of WOP, which might be further reduced by interleaving of ports and by rerouting of connections across the access waveguides, similarly to the case of the surface-coupled planar circuits shown in Figs. 4.2(b)–4.2(d). As in the case of surface coupling, the number of WOP along any optical path through the
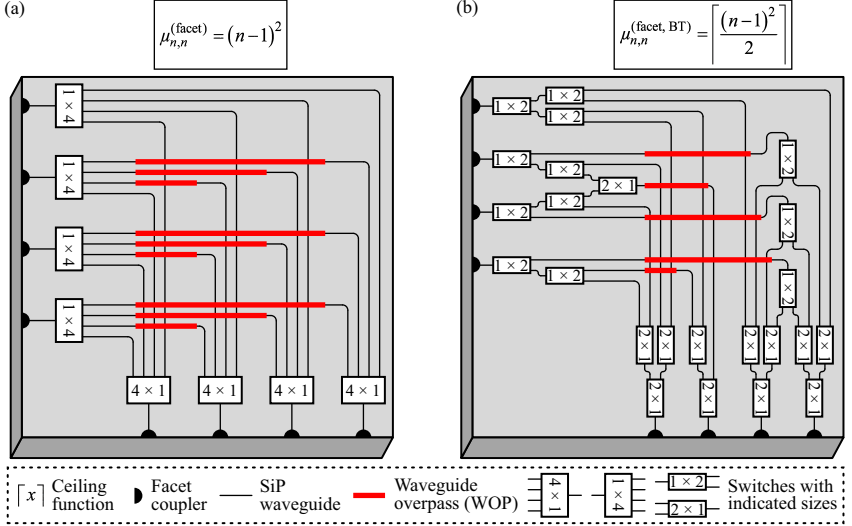
Figure B.3: Circuit layouts for facet-coupled 2D/3D hybrid 4×4 SAS. (a) Simple, but not optimal layout, where the 1×4 and 4×1 switches have been realized as LE. The relation for $\mu_{n,n}^{(\text{facet})}$ represents the exact number of WOP in this simplistic implementation. (b) Best found, but not necessarily optimal layout for the case in which the 1×4 and 4×1 switches have been realized as BT of 1×2 and 2×1 switches. The relation for $\mu_{n,n}^{(\text{facet, BT})}$ is an upper bound for the minimum number of WOP.

facet-coupled hybrid 2D/3D circuit is at most 1, whereas the maximum number of WGX along an optical path in a single-layer implementation shown in Fig. B.2(b) increases in proportion to $n^2/2$. The exact result for the maximum number of WGX along any optical path for this implementation is

$$\xi_{n,n}^{(\text{facet})} = 2 \left\lfloor \frac{n-1}{2} \right\rfloor \left\lceil \frac{n-1}{2} \right\rceil, \tag{B.10}$$

see Section B.3.2. The corresponding numbers for $n = 4, 8, 16, 32$, and 64 are indicated in the fifth and sixth column of Table B.1. For the implementations shown in Figs. B.2(c) and B.2(d), we cannot provide a formula that describes the minimum number of WGX along an optical path.

B.3.2 Graph-theoretical models and analysis of facet-coupled $m \times n$ SAS circuits

Let us first explain Eq. (B.10) which is obtained in case of a drawing of the complete bipartite subgraph $K_{n,n}$ that results in the outerplanar crossing number — the vertices belonging to different vertex sets M and N ($m = n$) are interleaved along the boundary curve. This subgraph is depicted in blue in Fig. B.2(b) for $n = 5$. The concept of this layout is illustrated in Fig. B.4, which shows graph drawings of a complete bipartite graph $K_{n,n}$ with interleaved vertices of two different vertex sets along the boundary (dashed circular line). Each edge divides the bounded area in two parts, and the largest number of crossings will be on an edge $\{v_{M,i}, v_{N,i}\}$ that divides the area such that the numbers of vertices in both parts are as much equal as possible. If n is odd, it is possible to find an edge that divides the bounded area such that both parts have exactly the same number of vertices; on the other hand, if n is even, one part will have one more vertex of each vertex set than the other part. Both cases are illustrated in Fig. B.4 — the edge $\{v_{M,i}, v_{N,i}\}$ is depicted in blue. For both cases, edge $\{v_{M,i}, v_{N,i}\}$ divides the area such that one part contains $\lfloor (n - 1/2) \rfloor$ and the other $\lceil (n - 1/2) \rceil$ vertices of each vertex set. That means that edge $\{v_{M,i}, v_{N,i}\}$ is crossed by $\lfloor (n - 1/2) \rfloor \lceil (n - 1/2) \rceil$ edges connecting $\lfloor (n - 1/2) \rfloor \lceil$ vertices of set M in the first part to $\lceil (n - 1/2) \rceil$ vertices of set N the second part, and the same number of edges connecting $\lfloor (n - 1/2) \rfloor$ vertices of set N in the first part to $d\lceil (n - 1/2) \rceil$ vertices of set M in the second part. From here follows the result of Eq. (B.10).

In order to estimate the number of necessary WOP (3D edges), we will use the simplistic layout shown in Fig. B.2(a). It is suffcient to consider a drawing of $K_{m,n}$ with all vertices placed on a closed boundary curve, since access waveguides do not have any crossings. We construct a corresponding graph drawing by placing all m vertices of set M: $v_{M,1}, v_{M,2}, ...v_{M,m}$ on the x-axis of the 2D Cartesian coordinate system in points $x = 1, 2, ..., m$, see Fig. B.5(a) for an illustration of the case of $K_{4,4}$. Similarly, we place all n vertices of set N: $v_{N,1}, v_{N,2}, ...v_{N,n}$ on the y-axis in points $y = 1, 2, ..., n$. Finally, we connect all vertices of set M
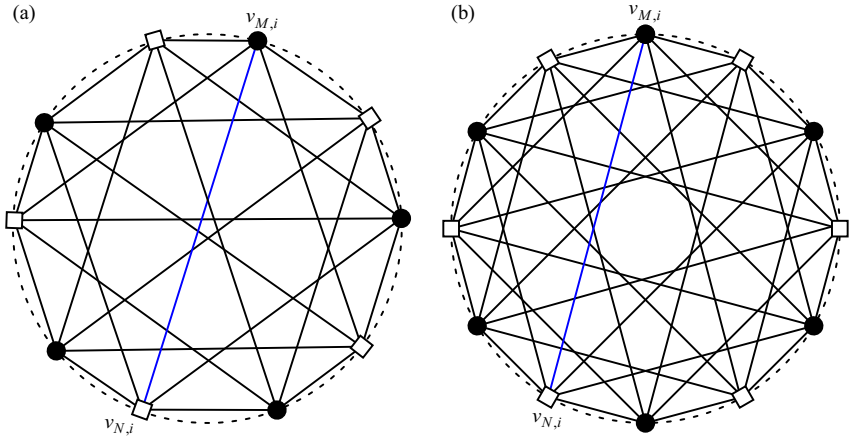
Figure B.4: Drawings of complete bipartite graphs $K_{n,n}$ with all vertices placed on the closed boundary curve (dashed circular line), and the vertices of two different sets being interleaved along the boundary. Equation (B.10) gives the local crossing number of such drawing, which occurs along the blue edges that divide the boundary area in two parts such that the number of vertices in both parts is as much balanced as possible. (a) In case n is odd (here: $n = 5$), both parts contain the same number of vertices. (b) In case n is even (here: $n = 6$), there is one more vertex of each vertex set in one part.

to all vertices of set N by mn line segments. The boundary curve can be for example a rectangle that is oriented along the x and the y axis, as depicted in green in Fig. B.5(a). The total number of crossings is equivalent to the one given by Eq. (B.5) — it takes four edges and one crossing to connect each possible pair of vertices of set M to each possible pair of vertices of set N. In order to estimate the number of necessary 3D edges, we first construct a spanning planar subgraph of $K_{m,n}$, by connecting vertices $v_{M,1}$ and $v_{N,n}$ to all vertices of the opposite vertex sets, see Fig. B.5(b). This subgraph evidently has $m + n - 1$ edges, and the number of missing edges is therefore equal to $mn - (m + n - 1) = (m - 1)(n - 1)$, which leads to Eq. (B.8). These edges can be realized with help of 3D edges, illustrated by dashed red lines in Fig. B.5(b).

Similarly to the case of surface coupled SAS described in Appendix B.2, if the $1 \times n$ and $m \times 1$ switches at the input and output ports are BT of 1×2 and 2×1
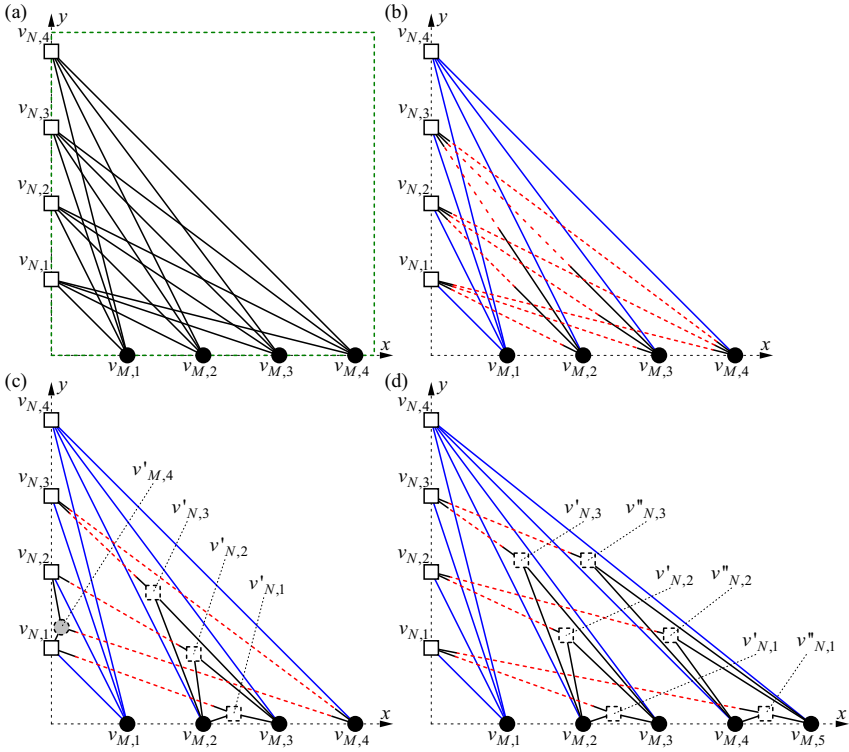
Figure B.5: Different graph drawings of a simplistic model of a facet-coupled 4×4 and 5×4 SAS circuit: (a) Graph drawing of a 4×4 SAS circuit where 1×4 and 4×1 switches at the input and output ports are LE. (b) Planar-edge-crossing-free graph representation of the same circuit. The edges depicted in blue represent a spanning planar subgraph of $K_{4,4}$. The remaining edges are realized with help of 3D edges (representing WOP) depicted as dashed red lines. The 3D edges connect to planar edges depicted in black that connect to the vertices in the drawing plane. (c) If the 1×5 and 5×1 switches at the input and output ports are realized as BT of 1×2 and 2×1 switches, the number of necessary 3D edges can be reduced by splitting the vertices of the original $K_{4,4}$ and by placing them into appropriate areas which are defined by the edges of the spanning planar subgraph (blue) and by the x or y coordinate axes. The white dashed squares represent 1×2 switches, while the filled gray circle represents a 2×1 switch. This approach allows to replace two 3D edges by one. In case where both m and n are even, the number of missing edges is odd, therefore, one missing edge (here: $\{v_{N,3}, v_{M,4}\}$) must be realized with help of one single 3D edge. (d) Graph drawing of a 5×4 SAS circuit, analogous to the case described in (c). In case at least one of the numbers m or n is odd, the number of 3D edges can be reduced exactly 2 times compared to the case when $1 \times n$ and $m \times 1$ switches are realized as LE.

switches, the number of necessary 3D edges reduces. We will split the analysis into two cases: when both m and n are even, and when at least one of them is odd. If both are even, the analysis comprises the following steps:

Step 1: Construct a spanning planar subgraph of $K_{m,n}$ as described above. Each pair of vertices $\{v_{M,2}, v_{M,3}\}, \{v_{M,4}, v_{M,5}, ..., \{v_{M,m-2}, v_{M,m-1}\}\}$, together with vertex $v_{N,n}$ defines one area, which is bounded by two edges between $v_{N,n}$ and the two vertices of set M and a portion of the x-axis between the two vertices of set M. This is illustrated on an example of $K_{4,4}$ in Fig. B.5(c).

Step 2: Put an auxiliary vertex $v'_{N,1}$ inside the area defined by vertices $\{v_{M,2}, v_{M,3}, v_{N,n}\}$, see Fig. B.5(c). We can connect the auxiliary vertex $v'_{N,1}$ and vertex $v_{N,1}$ by a 3D edge, and the same auxiliary vertex and vertices $v_{M,2}$ and $v_{M,2}$ by planar edges. Similarly to the case of surface coupled SAS, we continue adding auxiliary vertices $v'_{N,2}, v'_{N,3}, ..., v'_{N,n-1}$, to the same area until we connect all vertices of set N to $v_{M,2}$ and $v_{M,3}$. We then continue with the same procedure for the following areas defined by groups of three vertices: $\{v_{M,4}, v_{M,5}, v_{N,n}\}, ..., \{v_{M,n-2}, v_{M,n-1}, v_{N,n}\}$.

Step 3: In this fashion, we will connect all vertices of set M to all vertices of set N, except for vertex $v_{M,m}$ that is connected only to $v_{N,n}$. However, each of the following pairs of vertices $\{v_{N,1}, v_{N,2}, ..., \{v_{N,n-3}, v_{N,n-2}\}$,together with vertex $v_{M,1}$ define one area bounded by two edges (between $v_{M,1}$ and the two vertices of set N) and a portion of the y-axis between the two vertices of set N. In each of these areas, we can place one auxiliary vertex: $v'_{M,m}, v''_{M,m}, v'''_{M,m}, ...$ Each of these auxiliary vertices can be connected to $v_{M,m}$ by a 3D edge, and to the respective pair of vertices of set N that define the area in which the auxiliary vertex is placed by two planar edges. After this step, there will be only one missing edge between vertices $v_{M,m}$ and $v_{N,n-1}$, and we directly connect these two vertices by a single 3D edge, see Fig. B.5(c).

In case when at least one of the numbers m and n is odd, we can assume without loss of generality that m is odd, and n is even. By executing Step 1 as described

123

above, we will get a subgraph where each of the pairs of vertices $\{v_{M,2}, v_{M,3}\}$, $\{v_{M,4}, v_{M,5}\}, ..., \{v_{M,m-1}, v_{M,m}\}$, together with vertex $v_{N,n}$ defines one area bounded by two edges (between $v_{N,n}$ and the two vertices of set M) and a portion of the x-axis between the two vertices of set M. After performing Step 2 as described above, we will connect all vertices of set M to all vertices of set N. This case is illustrated on an example of $K_{5,4}$ in Fig. B.5(d). For at least one of the numbers m and n being odd, the number of missing edges is even, and we can replace two missing planar edges by one 3D edge. Combining the two cases leads to Eq. (B.9).

[end of appendices of publication [J3]]

C 3D-printed PBS: Details on polarization extinction ratio (PER) and data transmission experiment

The content of Appendix C is based on Methods and Supplementary Information of manuscript [J2], and it has been modified to fit the formatting rules of this thesis.

Aleksandar Nesic,[†] Matthias Blaicher,[†] Pablo Marin-Palomo, Christoph Füllner, Sebastian Randel, Wolfgang Freude, and Christian Koos

[†]These authors contributed equally to this work.

[start of the content based on methods and supplementary information of manuscript [J2]]

To be submitted for publication to Light: Science & Applications

C.1 Methods

Simulations

For the simulations shown in Fig. 5.2, the 3D structure of the PBS was modeled using a commercially available 3D numerical time-domain solver (CST Microwave Studio [154]), which is based on the finite integration technique [95]. The final design of the PBS was the result of a manual optimization based on several parameter sweeps.

Fabrication

All 3D-printed structures were fabricated using a home-built two-photon lithography system equipped with a 63× microscope objective lens (numerical aperture 1.4, field number 25 mm) and galvanometer mirrors for rapid beam movement in the lateral directions. As a lithography light source, we use a fs-laser with a pulse length of less than 80 fs (C-Fiber 780 Femtosecond Fiber Laser, Menlo) and a repetition rate of 100 MHz. The lithography system is equipped with a dedicated control software that allows for precise localization of the optical fiber core as well as for automated fabrication of the PBS with high shape fidelity. The system is equipped with a confocal imaging unit using the lithography laser and its beam deflectors for the acquisition of 3D images that are perfectly aligned to the lithography coordinate system and hence to any lithographically fabricated structures. For confocal imaging, the laser power is reduced to avoid any unwanted polymerization in the photoresist. In our current experiments, we use standard writing techniques without taking any measures for process acceleration, leading to fabrication times of typically 5 min per PBS/PR, including the massive mechanical support structures. The fabrication time of the PBS/PR (including mode-field adapters) is below 1 min. Currently, the exposure time is dominated by the slow exposure speed, chosen to achieve the best shape accuracy. In the lithography process, the liquid negative-tone photoresist (Nanoscribe IP-Dip, refractive index $n = 1.52$ at 780 nm, unexposed; see also [155]) simultaneously acts as an immersion medium for the objective lens. Unexposed photoresist is removed in a two-step development process using propylene-glycol-methyl-ether-acetate (PGMEA) as a developer for 20 min, followed by rinsing in isopropyl alcohol (2-propanol).

Trajectory planning and fiber-to-PBS interface

For the polarization rotators and the output waveguides, careful planning of the 3D trajectory is important to ensure efficient coupling between the PBS and other optical structures. To this end, we use a parametrized trajectory and optimize it for low curvature and hence low radiation loss. Along this trajectory, the waveguide cross-section is extruded to form a 3D model of the structure that is

then lithographically fabricated. Low-loss coupling between PBS and the standard single-mode fiber (Corning SMF-28) at its input is achieved by a taper-like mode-field adapter, designed for a mode-field diameter (MFD) of (10.3 ± 0.4) µm at 1550 nm at the fiber side. The MFD is defined as the diameter at which the intensity has dropped to $1/e^2$ of its maximum value measured in the center of the fiber core. The methods are derived from the photonic wire bonding process, details on which can be found in [13].

Characterization using an IR microscope

For characterization of the 3D-printed PBS in Fig. 5.3, we use an IR camera (Goldeye G-032 SWIR, Allied Vision) attached to a microscope (DMRXA with a variable zoom unit DMRD, Leica/Leitz) that is equipped with an IR objective (LMPlan IR $100 \times /0.80$NA, Olympus). An optional rotatable linear polarizer (LPIREA100-C, Thorlabs, PER > 34 dB at 1550 nm) can be inserted into the infinity-optical beam path of the microscope. Laser light generated by a tunable external-cavity laser (IQS-2600B, EXFO) is injected into the SMF, and the polarization is adjusted by a standard fiber-based polarization controller. Each acquired image is corrected for the background signal that is seen with the laser turned off.

Polarization extinction ratio measurement

The Stokes vector response shown in Fig.5.4(c) is measured by an optical component analyzer (Keysight N7788B), which comprises an integrated fast polarization controller and a polarimeter. The polarization controller randomly scrambles the state of polarization, thereby uniformly covering the whole Poincaré sphere. The polarization state and the power at the output of the PBS structure are measured simultaneously by the polarimeter. The PER can be extracted from these measurements, see Appendix C.3 for details. The PER is measured at seven discrete wavelengths between 1270 nm and 1620 nm, using three different tunable laser sources (Ando AQ321D, TUNICS-T1005HP, Agilent 81600B).

Data transmission experiment

In our data transmission experiments, we used four output channels from an AWG (Keysight M8196A) to generate the drive signals for the dual-polarization IQ modulator, see Appendix C.4 for a sketch of the underlying experimental setup. The signals are derived from random bit patterns with different seeds, such that each polarization carries uncorrelated data, and are pre-distorted to compensate for the measured frequency response of the transmitter. After transmitter, band-limited amplified spontaneous-emission (ASE) noise is generated by an ASE source (Orion Laser Technology ASE-C/CL) and added to the signal to vary its optical signal-to-noise ratio (OSNR). The signal is then fed to the receiver, which comprises an erbium-doped fiber amplifier (EDFA) followed by a bandpass filter (full width at half maximum 1 nm) to suppress out-of-band amplified spontaneous emission (ASE) noise. After the preamplifier, the signal is fed to the 3D-printed PBS/PR, where the two orthogonal polarization states are split and rotated to an identical direction. The two partial signals are then detected using a coherent heterodyne scheme, where the optical local oscillator tone (LO, Keysight N7714A) is placed at the edge of the signal spectrum and where two balanced photodiodes (Finisar BPDV2150RQ) remove both signal-signal and LO-LO interference, see Appendix C.4 for details. The outputs of the photodiodes are digitized by a 256 GSa/s real-time oscilloscope (Keysight UXR1004A) and recorded for offline digital signal processing (DSP). In a first DSP step, the signals are shifted in frequency by the difference between the carrier and the LO tone. This is followed by timing recovery, equalization, and carrier recovery. Finally, the signals go through a least-mean-square equalizer and are finally decoded.

C.2 Scattering parameters, Jones matrix, and PER

Figure 5.2(c) of Chapter 5 gives quantitative information on the PBS performance in terms of transmission, crosstalk, leakage, unfilterable crosstalk, and PER. The first four parameters are directly extracted from the corresponding elements of the scattering matrix, as indicated in Fig. 5.2(c) and in Chapter 5. For calculating the

PER, we use the ratio of the squares of the singular values of the simulated Jones matrices of the PBS [156]. The Jones matrix associated with a certain output port describes the propagation of light from the PBS input port to this output ports. In the following, the Jones matrix associated with output port H is denoted as $\mathbf{T}_{\mathrm{PBS},H}$, while $\mathbf{T}_{\mathrm{PBS},V}$ refers to output port V. The Jones vectors at the input port is $\mathbf{J}_I = \begin{bmatrix} E_H^{(I)} & E_V^{(I)} \end{bmatrix}^{\mathrm{T}}$, while the Jones vectors at the output ports H and V are $\mathbf{J}_H = \begin{bmatrix} E_H^{(H)} & E_V^{(H)} \end{bmatrix}^{\mathrm{T}}$ and $\mathbf{J}_V = \begin{bmatrix} E_H^{(V)} & E_V^{(V)} \end{bmatrix}^{\mathrm{T}}$. The Jones-matrix elements can be directly taken from the scattering matrix, such that the relations $\mathbf{J}_H = \mathbf{T}_{\mathrm{PBS},H}\mathbf{J}_I$ and $\mathbf{J}_V = \mathbf{T}_{\mathrm{PBS},V}\mathbf{J}_I$ between the Jones vectors and the input and at the output can be written as

$$\begin{bmatrix} E_H^{(H)} \\ E_V^{(H)} \end{bmatrix} = \begin{bmatrix} \underline{S}_{E_H^{(H)}E_H^{(I)}} & \underline{S}_{E_H^{(H)}E_V^{(I)}} \\ \underline{S}_{E_V^{(H)}E_H^{(I)}} & \underline{S}_{E_V^{(H)}E_V^{(I)}} \end{bmatrix} \begin{bmatrix} E_H^{(I)} \\ E_V^{(I)} \end{bmatrix}, \tag{C.1}$$

$$\begin{bmatrix} E_H^{(V)} \\ E_V^{(V)} \end{bmatrix} = \begin{bmatrix} \underline{S}_{E_H^{(V)}E_H^{(I)}} & \underline{S}_{E_H^{(V)}E_V^{(I)}} \\ \underline{S}_{E_V^{(V)}E_H^{(I)}} & \underline{S}_{E_V^{(V)}E_V^{(I)}} \end{bmatrix} \begin{bmatrix} E_H^{(I)} \\ E_V^{(I)} \end{bmatrix}. \tag{C.2}$$

The PER is then calculated as the ratio of the squares of the singular values s_1 and s_2 of the corresponding Jones matrices [156],

$$\mathrm{PER} = \frac{s_1^2\left(\mathbf{T}_{\mathrm{PBS},H}\right)}{s_2^2\left(\mathbf{T}_{\mathrm{PBS},H}\right)} = \frac{s_1^2\left(\mathbf{T}_{\mathrm{PBS},V}\right)}{s_2^2\left(\mathbf{T}_{\mathrm{PBS},V}\right)}, \tag{C.3}$$

where $s_1 \geq s_2$ without loss of generality.

C.3 Measurement of the PER

The PER of an optical device is generally defined as the ratio of maximum to minimum output power P_{out} that can be found when varying the input polarization over all possible states. In our experiments, the input polarization states were sampled randomly, and a straightforward way of calculating the PER is taking the ratio of the maximum to the minimum recorded output power. However, this approach takes into account only two measured power levels, which bears the

risk that the result is subject to noise and could lead to an overestimated PER. In addition, there is no guarantee that the sampled input states will fall close enough to the states of minimum and maximum transmitted power.

We therefore implemented a PER evaluation technique that considers all power levels recorded for the various input polarization states and relies on fitting a theoretical curve to the full set of measurement data. The experimental setup is described in more detail in, Fig. C.1(a). To explain this technique, we consider only one output port of the 3D-printed polarization-beam- splitter/polarization-rotator combination (PBS/PR) — the other output port can be treated in an analogous way. For simplicity, we further assume that the maximum power transmission for the considered port occurs for a perfectly horizontal (x-polarized) polarization at both the input and the output of the PBS/PR, characterized by Stokes vectors $\mathbf{s}_{in,pass} = \mathbf{s}_{out,pass} = [1 \ 0 \ 0]^{T}$. Note, however, that the input port can only be accessed through an optical fiber that is connected to the polarization scrambler, and that the measurement of the power and the polarization state at the PBS/PR output requires a second optical fiber leading to the polarization analyzer. In the following, we assume fully polarized light such that we can use either Stokes or Jones calculus, as appropriate. We describe the input fiber between the polarization scrambler and the PBS/PR by a Jones matrix $\mathbf{U}$, whereas the output fiber is described by a Jones matrix $\mathbf{U}$, see Fig. C.1(a). For a given polarization state with Jones vector $\mathbf{J}_{scr}$ emitted by the polarization scrambler, the Jones vector of the polarization state $\mathbf{J}_{an}$ received by the polarization analyzer can then be written as

$$\mathbf{J}_{an} = \mathbf{V}\mathbf{T}_{PBS}\mathbf{U}\mathbf{J}_{scr}, \qquad (C.4)$$

where $\mathbf{T}_{PBS}$ corresponds to the Jones matrix of the non-ideal PBS/PR, and where the Jones matrices $\mathbf{U}$ and $\mathbf{V}$ of the input fiber and the output fiber can be assumed to be unitary, see Fig. C.1(a). The light at the PBS/PR input can be expressed by an input Jones vector $\mathbf{J}_{in} = \mathbf{U}\mathbf{J}_{scr}$, which is characterized by an angle α_{in} that
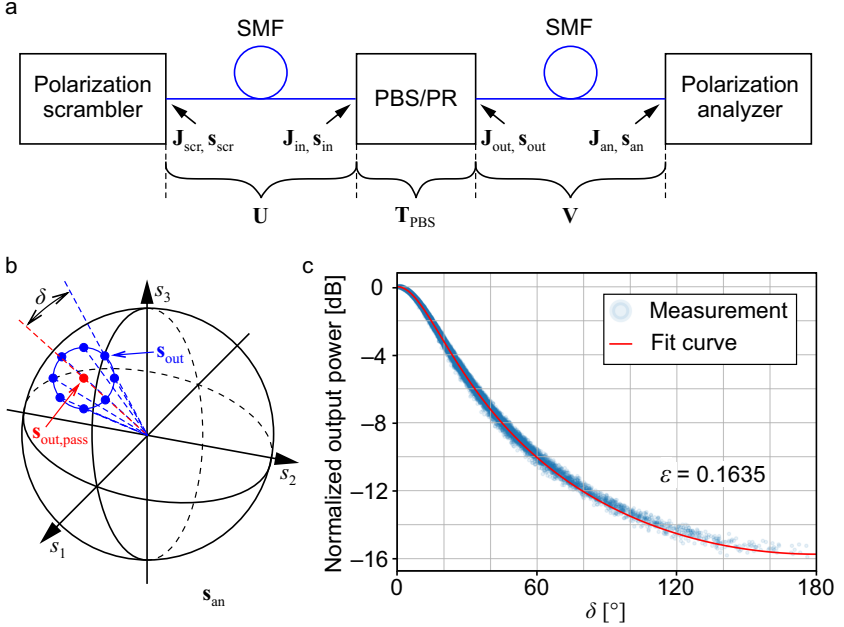
Figure C.1: Measurement and evaluation of the polarization extinction ratio (PER) of the 3D-printed polarization-beam-splitter/polarization-rotator combination (PBS/PR), taking into account the full set of measured output powers and polarization states. (a) Experimental setup: The 3D-printed PBS/PR is fed through a standard single-mode fiber (SMF) by light emitted from a polarization scrambler, and the output power and the output polarization state are measured by a polarization analyzer connected to the PBS/PR by a second SMF. $\mathbf{J}_{\text{scr}}$, $\mathbf{J}_{\text{in}}$, $\mathbf{J}_{\text{out}}$, and $\mathbf{J}_{\text{an}}$ denote the Jones vectors and the output of the polarization scrambler, the input and the output of the PBS/PR, and at the input of the polarization analyzer, while $\mathbf{s}_{\text{scr}}$, $\mathbf{s}_{\text{in}}$, $\mathbf{s}_{\text{out}}$, and $\mathbf{s}_{\text{an}}$ denote the corresponding Stokes vectors. The non-ideal PBS/PR is modeled by a Jones matrix $\mathbf{T}_{\text{PBS}}$, while the two SMF at the input and the output side of the PBS/PR are represented by two unitary Jones matrices U and V, respectively. (b) Illustration of the Stokes vectors recorded by the polarization analyzer. Since we assume fully polarized light, all Stokes vectors are on the surface of the Poincaré sphere. The output power should be the same for all polarization states that are located on a circle which is centered about the state of maximum transmission. The radius of this circle is quantified by the opening angle δ of the associated cone. (c) Normalized output power P_{out} vs. angle δ, as recorded for the data point for Output I at a wavelength of 1460 nm, see Fig. 5.4(d) of the main manuscript. By fitting a model function (red) to the measurement data (blue), we extract a field leakage of $\varepsilon = 0.1635$, corresponding to a PER of 15.7 dB.

defines the ratio of the field amplitudes in the two polarizations and by a phase difference φ between the x- and the y-component,

$$\mathbf{J}_{\text{in}} = |E_{\text{in}}| \left[\cos\left(\alpha_{\text{in}}\right) e^{-\mathrm{j}\varphi/2} \quad \sin\left(\alpha_{\text{in}}\right) e^{+\mathrm{j}\varphi/2} \right]. \tag{C.5}$$

In this relation, $|E_{in}|$ denotes the magnitude of the electric field that is associated with the signal at the input of the 3D-printed PBS/PR — the corresponding power is denoted by $P_{in} \sim |E_{in}|^2$. For the PBS/PR, we assume a simplified Jones matrix $\mathbf{T}_{PBS}$ that corresponds to that of a non-ideal linear polarizer oriented along the x-direction,

$$\mathbf{T}_{PBS} = \begin{bmatrix} 1 & 0 \\ 0 & \varepsilon \end{bmatrix}, \tag{C.6}$$

where ε, $0 \leq \varepsilon \leq 1$, is the magnitude of the polarization leakage. The corresponding PER is then found as the ratio of the squares of the singular values of $\mathbf{T}_{PBS}$ [156]

$$PER = \frac{1}{\varepsilon^2}. \tag{C.7}$$

Note that the model for the Jones matrix according to Eq. C.6 represents an approximation: The Jones matrices $\mathbf{T}_{PBS,H}$ and $\mathbf{T}_{PBS,V}$ that are obtained from our simulations, Eqs. C.1 and C.2, do have non-zero off-diagonal elements and are generally not Hermitian. As a consequence, transformation into a diagonal matrix as assumed in Eq. C.6 is not generally possible. Still, the magnitudes of the off-diagonal elements are small such that the associated error should not be severe, see discussion below.

Using the Jones-matrix model according to Eq. C.6, the relation between a given polarization state, $\mathbf{J}_{in}$ at the input of the PBS/PR and the corresponding output state $\mathbf{J}_{out}$ can be written as

$$\mathbf{J}_{out} = \mathbf{T}_{PBS}\mathbf{J}_{in} = \begin{bmatrix} 1 & 0 \\ 0 & \varepsilon \end{bmatrix} \cdot \begin{bmatrix} \cos{(\alpha_{in})}\,e^{-j\varphi/2} \\ \sin{(\alpha_{in})}\,e^{+j\varphi/2} \end{bmatrix}. \tag{C.8}$$

We can now express the ratio of the power P_{out} at the output of the PBS/PR to the input power P_{out} in terms of the magnitude of the polarization leakage ε and the angle α_{in},

$$\frac{P_{out}}{P_{in}} = \frac{|E_{out}|^2}{|E_{in}|^2} = |\mathbf{J}_{out}|^2 = \cos^2{(\alpha_{in})} + \varepsilon^2 \sin{(\alpha_{in})}^2, \tag{C.9}$$

where $|E_{\text{out}}|$ is the magnitude of the electric field at the PBS/PR output. As expected, Eq. C.9 does not depend on the phase difference φ.

Note that the angle α_{in} and thus the expression for the output power are related to the Jones vector at the output of the PBS/PR, which cannot be accessed in the measurement. To establish a relationship to the known polarization state $\mathbf{J}_{\text{an}}$ at the input of the polarization analyzer, we proceed in two steps. First, we switch to Stokes space and we find a relationship that connects the angle α_{in} and the magnitude of the polarization leakage ϵ in Eq. C.8 to the angle δ between the actual Stokes vector $\mathbf{s}_{\text{out}}$ at the PBS/PR output and the stokes vector $\mathbf{s}_{\text{out,pass}} = [1 \ \ 0 \ \ 0]^{\text{T}}$ that corresponds to maximum transmission. To this end, we first calculate $\mathbf{s}_{\text{out}} = \begin{bmatrix} s_{\text{out},1} & s_{\text{out},2} & s_{\text{out},3} \end{bmatrix}^{\text{T}}$ from the components of vector $\mathbf{J}_{\text{out}}$ using Eqs. (6.1–9a)–(6.1–9d) in [69]. The angle $\delta \in [0, \pi]$ between the measured Stokes vector s_{out} and output Stokes vector $s_{\text{out,pass}} = [1 \ \ 0 \ \ 0]$ of maximum transmission can then be calculated as

$$\cos(\delta) = \mathbf{s}_{\text{out}} \cdot \mathbf{s}_{\text{ref}} = s_{out,1} = \frac{\cos^2(\alpha_{\text{in}}) - \varepsilon^2 \sin(\alpha_{\text{in}})^2}{\cos^2(\alpha_{\text{in}}) + \varepsilon^2 \sin(\alpha_{\text{in}})^2}, \tag{C.10}$$

which can be simplified to

$$\tan\left(\frac{\delta}{2}\right) = \varepsilon \tan(\alpha_{\text{in}}). \tag{C.11}$$

In a second step, we account for the propagation of the signal from the PBS/PR output to the polarization analyzer. To this end, we exploit the fact that the corresponding Jones vectors $\mathbf{J}_{\text{out}}$ and $\mathbf{J}_{\text{an}}$ are related by a unitary transformation that is described by the Jones matrix $\mathbf{V}$. In Stokes space, this transformation simply corresponds to a rotation about the origin, which leaves the relative angle δ between the measured Stokes vectors $\mathbf{s}_{\text{out}}$ and $\mathbf{s}_{\text{out,pass}}$ unchanged. In other words: For a given polarization leakage magnitude ε, the output power P_{out} should be the same for all polarization states that are located on a circle on the surface of the Poincaré sphere which is centered about $\mathbf{s}_{\text{out,pass}}$, see Fig. C.1(b). We may thus

extract this angle directly from the polarization states recorded at the polarization analyzer, where $\mathbf{s}_{\text{out,pass}}$ corresponds to polarization state for which the highest output power was measured. We then use Eq. C.11 with ε as a parameter to extract α_{in} and predict the dependence of the power P_{out} on δ via Eq. C.9, assuming constant P_{in}. We finally vary the magnitude of the polarization leakage ε to find best coincidence between the measured δ-dependence of P_{out} and the associated model prediction, see Fig. C.1(c). Equation C.7 then allows us to calculate the PER for this value of ε.

We show the results of this technique in Fig. C.1(c) for the highest PER that we measured in the context of the wavelength sweep, i.e., for Output I at a wavelength of 1460 nm, see Fig. 5.4(d). From the least-squares model fit shown in Fig. C.1(c), we estimate a field leakage ε of 0.1635, corresponding to a PER of 15.7 dB. To check the validity of the approach, we also extract the PER by simply taking the ratio of the maximum and the minimum transmitted power, which leads to value of 16.1 dB. This confirms the validity of our approach, in particular with respect to the simplified model for the Jones matrix according to Eq. C.6. The result is also in line with the expectation that the PER extracted from the ratio of the maximum and the minimum transmitted power might be slightly overestimated due to measurement noise. We further checked the impact of neglecting the off-diagonal Jones-matrix elements in Eq. C.6 by simulations. To this end, we omit the elements $\underline{S}_{E_H^{(H)} E_V^{(I)}}$, $\underline{S}_{E_V^{(H)} E_H^{(I)}}$, $\underline{S}_{E_V^{(V)} E_H^{(I)}}$, and $\underline{S}_{E_V^{(V)} E_H^{(I)}}$ of the simulated Jones matrices according to Eq. C.1 and C.2 and then extract the PER via Eq. C.7. The resulting PER is then compared to the one extracted from the singular values of the full Jones matrices, see Fig. C.3. We find that omitting the off-diagonal Jones-matrix elements leads to a slight reduction of the extracted PER, and we conclude that the simplification related to Eq. C.6 does not bear the risk to overestimate the PER in our experiments.
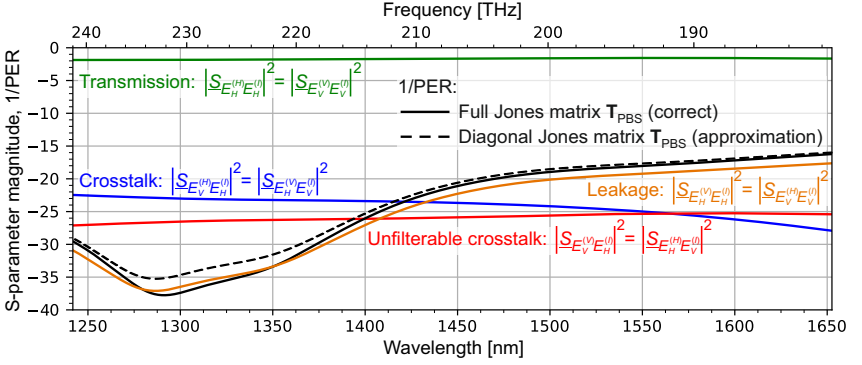
Figure C.2: Comparison of PER extracted from the simulated Jones matrices without any off-diagonal elements according to the simplified model in Eq. (S6) (dashed black lines) and the PER extracted from the full Jones matrix (solid black line). The device is the same as the one described by Fig. 5.2(c) of Chapter 5. For better comparison, we also give the transmission, the crosstalk, the leakage, and the unfilterable crosstalk of the device — they are identical to the curves in Fig. 5.2(c) of Chapter 5.

C.4 Data transmission experiment

The setup used for data transmission experiment is depicted in Fig. C.3. A dual-polarization (DP) IQ modulator is driven by 16QAM signals at a symbol rate of 80 GBd. The drive signals are generated by a high-speed arbitrary waveform generator (AWG, Keysight M8194A 120 GSa/s) using random bit sequences with different seeds for each polarization. The optical carrier at a wavelength of 1550 nm is extracted from an external-cavity laser (ECL, Keysight N7714A). Root-raised-cosine pulse shaping at a roll-off factor of $\beta = 0.1$ is used for improved spectral efficiency. The signal is then sent to the receiver setup. For the OSNR sweep, band-limited amplified-stimulated emission (ASE, Orion Laser Technology ASE-C/CL) noise is added to the optical signal (ASE noise loading). The signal is then amplified by an EDFA, filtered by a bandpass filter (BPF, full width at half maximum 1 nm) to suppress out-of-band amplified ASE noise, and sent to the PBS, which may be either a 3D-printed PBS/PR assembly or a commercial fiber-based PBS that we use as a reference. After the PBS, each polarization is detected using a coherent heterodyne scheme, where the local oscillator (LO,

Keysight N7714A)) is placed at the edge of the signal, see Inset 1 of Fig. C.3. Two balanced photodetectors (BPD, Finisar BPDV2150RQ) are used to suppress both signal-signal and LO-LO mixing products. The outputs of the BPD are digitized by a 256 GSa/s real-time oscilloscope (Keysight UXR1004A) and recorded for offline digital signal processing (DSP). In a first DSP step, the signals are made analytic and are shifted in frequency by the difference between the carrier and the LO. This is followed by timing recovery, equalization, and carrier recovery. Finally, the signals go through a least-mean-square equalizer and are decoded. To benchmark the performance of the PBS/PR assembly, the experiment is also performed with a commercially available PBS (AFW Technologies POBS-15). Since the commercially available PBS exhibits less insertion loss than the PBS/PR-fanout assembly, we adjust the amplification of the EDFA to obtain equal powers at the inputs of the BPD in both cases.
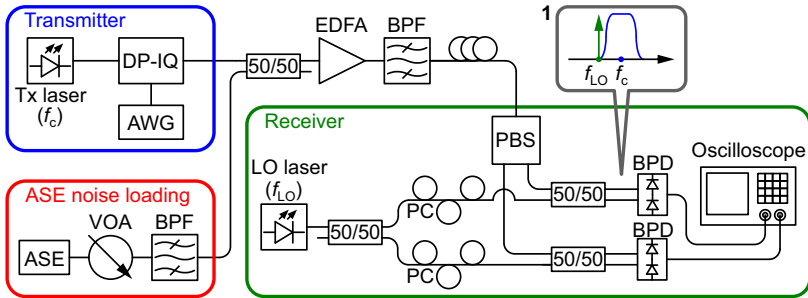
Figure C.3: Data transmission setup: The carrier at $\lambda = 1550$ nm is modulated by a dual polarization IQ (DP-IQ) modulator that is driven by an arbitrary waveform generator (AWG) to generate a 16QAM PDM signal at 80 GBd. The band-limited amplified spontaneous emission (ASE) source generates a noise signal, whose power is varied by the variable optical attenuator (VOA), and added to the 16QAM signal. This sum of two signals is amplified by an EDFA, filtered by a bandpass filter (BPF). and guided to the PBS input in the receiver block. A local oscillator (LO) signal is split, and the two split signals are polarization controlled by two polarization controllers (PC) and added to the two split signals from the two outputs of the PBS. The two interfered signals are led to two balanced photodetectors (BPD) and detected by a high-speed oscilloscope. Inset 1 illustrates the spectrum at the BPD inputs, with the LO placed at the edge of the signal spectrum.

[end of the content based on methods and supplementary information of manuscript [J2]]

D Glossary

D.1 List of abbreviations

16QAM	16-state quadrature amplitude modulation
32QAM	32-state quadrature amplitude modulation
64QAM	64-state quadrature amplitude modulation
ASE	Amplified spontaneous emission
AWG	Arbitrary waveform generator
BER	Bit-error ratio
BOX	Buried oxide
BPD	Balanced photodetector
BPF	Bandpass filter
BPM	Beam propagation method
BT	Binary tree
CMOS	Complementary metal-oxide-semiconductor
CMP	Chemical mechanical planarization
CST MWS$^{®}$	Computer Simulation Technology Microwave Studio [154]
CVD	Chemical vapor deposition
CS	Current source
CW	Continuous wave
DSP	Digital signal processing
ECL	External-cavity laser

EIC	Electronic integrated circuit
EDFA	Erbium-doped fiber amplifier
FDTD	Finite-difference-time-domain
FIT	Finite integration technique
FMA	Fundamental mode approximation
GC	Grating coupler
HD-FEC	Hard-decision forward-error correction
IL	Insertion loss
IQ	In-phase and quadrature
IR	Infra-red(-sensitive)
LE	Lumped element
LO	Local oscillator
MCW	Multi-contact probe wedge
MFD	Mode-field diameter
MMI	Multi-mode-interference (coupler)
MZI	Mach-Zehnder interferometer
NP	Nondeterministic polynomial
OPM	Optical power meter
OSA	Optical spectrum analyzer
OSNR	Optical signal-to-noise (power) ratio
PBS	Polarization beam splitter
PC	Polarization controller
PCB	Printed circuit board
PDM	Polarization-division multiplexing
PER	Polarization extinction ratio
PF	Polarizing filter

PGMEA	Propylene-glycol-methyl-ether-acetate
PIC	Photonic integrated circuit
PR	Polarization rotator
PWB	Photonic wire bond
RMF	Rotation minimizing frame
RMS	Root mean square
S	Scattering
SAS	Switch-and-select
SEM	Scanning electron microscopy
SiN	Silicon-nitride
SiP	Silicon photonic(s)
SMF	Single-mode fiber
SNR	Signal-to-noise (power) ratio
SOH	Silicon-organic hybrid
SOI	Silicon-on-insulator
SWG	Sub-wavelength grating
STED	Stimulated-emission-depletion
TE	Transverse-electric
TIR	Total internal reflection
TLS	Tunable laser source
TM	Transverse-magnetic
TO	Transformation-optics
UV	Ultraviolet
WG	Waveguide
WGX	Waveguide crossing
WOP	Waveguide overpass

D.2 List of symbols

D.2.1 Greek symbols

β	Roll-off factor
η	Maximum number of crossings along any optical path
Δ	Difference
δ	Angle to the preferable polarization on the Poincaré sphere
ε	Dielectric permittivity
$\boldsymbol{\varepsilon}$	Dielectric permittivity tensor
λ	Wavelength
μ	(1) Minimum number of WOP; (2) Magnetic permeability
$\boldsymbol{\mu}$	Magnetic permeability tensor
ξ	Minimum number of waveguide crossings required to realize a PIC
π	Archimedes' constant
φ	(1) Phase shift; (2) Phase difference
χ	Direction of the polarization ellipse
ω	Angular frequency

D.2.2 Latin symbols

A	Transmission of a phase shifter
$\mathrm{cr}\,(G)$	Crossing number of a graph
$\mathrm{cr}^*(G)$	Outerplanar crossing number of a graph
E	Set of edges of a graph
$\underline{E}$	Complex electric field

e	The base of the natural logarithm
f	Frequency
G	Graph
h	Height
i	Integer
J	(1) Jacobian matrix; (2) Jones vector
j	Imaginary unit
j	Integer
$K_{m,n}$	Complete bipartite graph
K_n	Complete graph
lcr (G)	Local crossing number of a graph drawing
m	Integer
M	Set of vertices of a graph
n	(1) Refractive index; (2) Integer
N	Set of vertices of a graph
P	Power
Q	Quality factor
R	Roll angle
r	Position (radius) vector
s	Singular value of a Jones matrix
s	Stokes three-vector
S	Stokes vector
T	Tangent vector (of the RMF)
$\underline{\mathbf{T}}$	(1) Transfer matrix; (2) Jones matrix
U	Vector of the RMF
v	Vertex of a graph

V	Vector of the RMF
w	Width

Bibliography

[1] S. E. Miller, "Integrated optics: An introduction," Bell System Technical Journal **48**, 2059–2069 (1969).

[2] R. Soref and J. Larenzo, "All-silicon active and passive guided-wave components for λ = 1.3 and 1.6 µm," IEEE Journal of Quantum Electronics **22**, 873–879 (1986).

[3] C. Weimann, A. Messner, T. Baumgartner, S. Wolf, F. Hoeller, W. Freude, and C. Koos, "Fast high-precision distance metrology using a pair of modulator-generated dual-color frequency combs," Optics Express **26**, 34305–34335 (2018).

[4] P. Trocha, M. Karpov, D. Ganin, M. H. P. Pfeiffer, A. Kordts, S. Wolf, J. Krockenberger, P. Marin-Palomo, C. Weimann, S. Randel, W. Freude, T. J. Kippenberg, and C. Koos, "Ultrafast optical ranging using microresonator soliton frequency combs," Science **359**, 887–891 (2018).

[5] A. Z. Subramanian, E. Ryckeboer, A. Dhakal, F. Peyskens, A. Malik, B. Kuyken, H. Zhao, S. Pathak, A. Ruocco, A. D. Groote, P. Wuytens, D. Martens, F. Leo, W. Xie, U. D. Dave, M. Muneeb, P. V. Dorpe, J. V. Campenhout, W. Bogaerts, P. Bienstman, N. L. Thomas, D. V. Thourhout, Z. Hens, G. Roelkens, and R. Baets, "Silicon and silicon nitride photonic circuits for spectroscopic sensing on-a-chip," Photonics Research **3**, B47–B59 (2015).

[6] C. V. Poulton, A. Yaacobi, D. B. Cole, M. J. Byrd, M. Raval, D. Vermeulen,

and M. R. Watts, "Coherent solid-state LIDAR with silicon photonic optical phased arrays," Optics Letters **42**, 4091–4094 (2017).

[7] Z. Wang, H.-C. Lee, D. Vermeulen, L. Chen, T. Nielsen, S. Y. Park, A. Ghaemi, E. Swanson, C. Doerr, and J. Fujimoto, "Silicon photonic integrated circuit swept-source optical coherence tomography receiver with dual polarization, dual balanced, in-phase and quadrature detection," Biomedical Optics Express **6**, 2562–2574 (2015).

[8] C. Koos, P. Vorreau, T. Vallaitis, P. Dumon, W. Bogaerts, R. Baets, B. Esembeson, I. Biaggio, T. Michinobu, F. Diederich, W. Freude, and J. Leuthold, "All-optical high-speed signal processing with silicon-organic hybrid slot waveguides," Nature Photonics **3**, 216–219 (2009).

[9] Y. Shen, N. C. Harris, S. Skirlo, M. Prabhu, T. Baehr-Jones, M. Hochberg, X. Sun, S. Zhao, H. Larochelle, D. Englund, and M. Soljačić, "Deep learning with coherent nanophotonic circuits," Nature Photonics **11**, 441–446 (2017).

[10] P. Steglich, M. Hülsemann, B. Dietzel, and A. Mai, "Optical biosensors based on silicon-on-insulator ring resonators: A review," Molecules **24**, 519 (2019).

[11] N. Lindenmann, G. Balthasar, D. Hillerkuss, R. Schmogrow, M. Jordan, J. Leuthold, W. Freude, and C. Koos, "Photonic wire bonding: a novel concept for chip-scale interconnects," Optics Express **20**, 17667 (2012).

[12] N. Lindenmann, S. Dottermusch, M. L. Goedecke, T. Hoose, M. R. Billah, T. P. Onanuga, A. Hofmann, W. Freude, and C. Koos, "Connecting silicon photonic circuits to multicore fibers by photonic wire bonding," Journal of Lightwave Technology **33**, 755–760 (2015).

[13] M. Blaicher, M. R. Billah, J. Kemal, T. Hoose, P. Marin-Palomo, A. Hofmann, Y. Kutuvantavida, C. Kieninger, P.-I. Dietrich, M. Lauermann, S. Wolf, U. Troppenz, M. Moehrle, F. Merget, S. Skacel, J. Witzens,

S. Randel, W. Freude, and C. Koos, "Hybrid multi-chip assembly of optical communication engines by in situ 3D nano-lithography," Light: Science & Applications **9** (2020).

[14] Y. Ma, Y. Zhang, S. Yang, A. Novack, R. Ding, A. E.-J. Lim, G.-Q. Lo, T. Baehr-Jones, and M. Hochberg, "Ultralow loss single layer submicron silicon waveguide crossing for SOI optical interconnect," Optics Express **21**, 29374 (2013).

[15] Y. Zhang, A. Hosseini, X. Xu, D. Kwong, and R. T. Chen, "Ultralow-loss silicon waveguide crossing using bloch modes in index-engineered cascaded multimode-interference couplers," Optics Letters **38**, 3608 (2013).

[16] T. J. Seok, N. Quack, S. Han, R. S. Muller, and M. C. Wu, "Large-scale broadband digital silicon photonic switches with vertical adiabatic couplers," Optica **3**, 64 (2016).

[17] L. Chen and Y. K. Chen, "Compact, low-loss and low-power 8×8 broadband silicon optical switch," Optics Express **20**, 18977 (2012).

[18] W. S. Zaoui, A. Kunze, W. Vogel, and M. Berroth, "CMOS-compatible polarization splitting grating couplers with a backside metal mirror," IEEE Photonics Technology Letters **25**, 1395–1397 (2013).

[19] B. Shen, P. Wang, R. Polson, and R. Menon, "An integrated-nanophotonics polarization beamsplitter with $2.4 \times 2.4\ \mu m^2$ footprint," Nature Photonics **9**, 378–382 (2015).

[20] W. D. Sacher, T. Barwicz, B. J. F. Taylor, and J. K. S. Poon, "Polarization rotator-splitters in standard active silicon photonics platforms," Optics Express **22**, 3777–3786 (2014).

[21] M. R. Watts, H. A. Haus, and E. P. Ippen, "Integrated mode-evolution-based polarization splitter," Optics Letters **30**, 967–969 (2005).

[22] J. Chiles, T. Sjaardema, A. Rao, and S. Fathpour, "Topographically anisotropic photonics for broadband integrated polarization diversity," https://arxiv.org/abs/1702.05806 (2017).

[23] K. Okamoto, *Fundamentals of optical waveguides* (Academic Press, 2005).

[24] J. Leuthold, C. Koos, W. Freude, L. Alloatti, R. Palmer, D. Korn, J. Pfeifle, M. Lauermann, R. Dinu, S. Wehrli, M. Jazbinsek, P. Günter, M. Waldow, T. Wahlbrink, J. Bolten, H. Kurz, M. Fournier, J. Fedeli, H. Yu, and W. Bogaerts, "Silicon-organic hybrid electro-optical devices," IEEE Journal of Selected Topics in Quantum Electronics **19**, 114–126 (2013).

[25] L. Xu, M. Nikoufard, X. J. M. Leijtens, T. de Vries, E. Smalbrugge, R. Notzel, Y. S. Oei, and M. K. Smit, "High-performance InP-based photodetector in an amplifier layer stack on semi-insulating substrate," IEEE Photonics Technology Letters **20**, 1941–1943 (2008).

[26] L. R. Chen, J. Wang, B. Naghdi, and I. Glesk, "Subwavelength grating waveguide devices for telecommunications applications," IEEE Journal of Selected Topics in Quantum Electronics **25**, 1–11 (2019).

[27] W. Bogaerts, D. Taillaert, P. Dumon, D. V. Thourhout, R. Baets, and E. Pluk, "A polarization-diversity wavelength duplexer circuit in silicon-on-insulator photonic wires," Optics Express **15**, 1567–1578 (2007).

[28] D. Taillaert, F. V. Laere, M. Ayre, W. Bogaerts, D. V. Thourhout, P. Bienstman, and R. Baets, "Grating couplers for coupling between optical fibers and nanophotonic waveguides," Japanese Journal of Applied Physics **45**, 6071–6077 (2006).

[29] W. S. Zaoui, M. F. Rosa, W. Vogel, M. Berroth, J. Butschke, and F. Letzkus, "Cost-effective cmos-compatible grating couplers with backside metal mirror and 69% coupling efficiency," Optics Express **20**, B238–B243 (2012).

[30] T. Yoshida, S. Tajima, R. Takei, M. Mori, N. Miura, and Y. Sakakibara, "Vertical silicon waveguide coupler bent by ion implantation," Optics Express **23**, 29449 (2015).

[31] M. Blaicher, M. R. Billah, T. Hoose, P.-I. Dietrich, A. Hofmann, S. Randel, W. Freude, and C. Koos, "3D-printed ultra-broadband highly efficient out-of-plane coupler for photonic integrated circuits," (Optical Society of America, San Jose, California, 2018), OSA Technical Digest (online), p. STh1A.1.

[32] X. Mu, S. Wu, L. Cheng, and H. Fu, "Edge couplers in silicon photonic integrated circuits: A review," Applied Sciences **10**, 1538 (2020).

[33] P.-I. Dietrich, M. Blaicher, I. Reuter, M. Billah, T. Hoose, A. Hofmann, C. Caer, R. Dangel, B. Offrein, U. Troppenz, M. Moehrle, W. Freude, and C. Koos, "In situ 3D nanoprinting of free-form coupling elements for hybrid photonic integration," Nature Photonics **12**, 241–247 (2018).

[34] M. R. Billah, M. Blaicher, T. Hoose, P.-I. Dietrich, P. Marin-Palomo, N. Lindenmann, A. Nesic, A. Hofmann, U. Troppenz, M. Moehrle, S. Randel, W. Freude, and C. Koos, "Hybrid integration of silicon photonics circuits and InP lasers by photonic wire bonding," Optica **5**, 876 (2018).

[35] R. L. Bishop, "There is more than one way to frame a curve," The American Mathematical Monthly **82**, 246 (1975).

[36] F. Klok, "Two moving coordinate frames for sweeping along a 3D trajectory," Computer Aided Geometric Design **3**, 217–229 (1986).

[37] D. Bechmann and D. Gerber, "Arbitrary shaped deformations with DOGME," The Visual Computer **19**, 175–186 (2003).

[38] M. Heiblum and J. Harris, "Analysis of curved optical waveguides by conformal transformation," IEEE Journal of Quantum Electronics **11**, 75–83 (1975).

[39] W. A. Gambling, H. Matsumura, and C. M. Ragdale, "Curvature and microbending losses in single-mode optical fibres," Optical and Quantum Electronics **11**, 43–59 (1979).

[40] D. Marcuse, "Bend loss of slab and fiber modes computed with diffraction theory," IEEE Journal of Quantum Electronics **29**, 2957–2961 (1993).

[41] F. Ladouceur and E. Labeye, "A new general approach to optical waveguide path design," Journal of Lightwave Technology **13**, 481–492 (1995).

[42] C. G. Poulton, C. Koos, M. Fujii, A. Pfrang, T. Schimmel, J. Leuthold, and W. Freude, "Radiation modes and roughness loss in high index-contrast waveguides," IEEE Journal of Selected Topics in Quantum Electronics **12**, 1306–1321 (2006).

[43] G. Bouchitté, M. L. Mascarenhas, and L. Trabucho, "On the curvature and torsion effects in one dimensional waveguides," ESAIM: Control, Optimisation and Calculus of Variations **13**, 793–808 (2007).

[44] M. Smit, E. Pennings, and H. Blok, "A normalized approach to the design of low-loss optical waveguide bends," Journal of Lightwave Technology **11**, 1737–1742 (1993).

[45] A. Melloni, P. Monguzzi, R. Costa, and M. Martinelli, "Design of curved waveguides: the matched bend," Journal of the Optical Society of America A **20**, 130–137 (2003).

[46] C. Koos, C. G. Poulton, L. Zimmermann, L. Jacome, J. Leuthold, and W. Freude, "Ideal bend contour trajectories for single-mode operation of low-loss overmoded waveguides," IEEE Photonics Technology Letters **19**, 819–821 (2007).

[47] T. Chen, H. Lee, J. Li, and K. J. Vahala, "A general design algorithm for low optical loss adiabatic connections in waveguides," Optics Express **20**, 22819–22829 (2012).

[48] M. Cherchi, S. Ylinen, M. Harjanne, M. Kapulainen, and T. Aalto, "Dramatic size reduction of waveguide bends on a micron-scale silicon photonic platform," Optics Express **21**, 17814 (2013).

[49] H. Wu, C. Li, L. Song, H.-K. Tsang, J. E. Bowers, and D. Dai, "Ultra-sharp multimode waveguide bends with subwavelength gratings," Laser & Photonics Reviews **13**, 1800119 (2019).

[50] M. Bahadori, M. Nikdast, Q. Cheng, and K. Bergman, "Universal design of waveguide bends in silicon-on-insulator photonics platform," Journal of Lightwave Technology **37**, 3044–3054 (2019).

[51] R. Baets and P. E. Lagasse, "Loss calculation and design of arbitrarily curved integrated-optic waveguides," Journal of the Optical Society of America **73**, 177 (1983).

[52] Y. Y. Lu and P. L. Ho, "Beam propagation modeling of arbitrarily bent waveguides," IEEE Photonics Technology Letters **14**, 1698–1700 (2002).

[53] Z. Hu and Y. Y. Lu, "Computing optimal waveguide bends with constant width," Journal of Lightwave Technology **25**, 3161–3167 (2007).

[54] R. N. Sheehan, S. Horne, and F. H. Peters, "The design of low-loss curved waveguides," Optical and Quantum Electronics **40**, 1211–1218 (2008).

[55] X. Antoine, P. Dreyfuss, and K. Ramdani, "A construction of beam propagation methods for optical waveguides," Communications in Computational Physics **6**, 565–576 (2009).

[56] F. Negredo, M. Blaicher, A. Nesic, P. Kraft, J. Ott, W. Dörfler, C. Koos, and C. Rockstuhl, "Fast and reliable method to estimate losses of single-mode waveguides with an arbitrary 2D trajectory," Journal of the Optical Society of America A **35**, 1063–1073 (2018).

[57] L. S. Dolin, "On the possibility of comparison of three-dimensional electromagnetic systems with nonuniform anisotropic filling," Izv. VUZov, Radiofizika **4**, 964–967 (1961).

[58] E. Post, *Formal structure of electromagnetics: General covariance and electromagnetics*, North-Holland Series in Physics (North-Holland Publishing Company, 1962).

[59] I. Lindell, *Methods for electromagnetic field analysis* (Clarendon Press, 1992).

[60] A. J. Ward and J. B. Pendry, "Refraction and geometry in Maxwell's equations," Journal of Modern Optics **43**, 773–793 (1996).

[61] T. Bawab, *Optical switching* (Springer, New York, N.Y, 2006).

[62] V. E. Beneš, *Mathematical theory of connecting networks and telephone traffic* (Academic Press, New York, 1965).

[63] R. Spanke, "Architectures for guided-wave optical space switching systems," IEEE Communications Magazine **25**, 42–48 (1987).

[64] B. G. Lee and N. Dupuis, "Silicon photonic switch fabrics: Technology and architecture," Journal of Lightwave Technology **37**, 6–20 (2019).

[65] L. A. Székely, *Graph theory – Favorite conjectures and open problems – 1; Chapter 13 Turán's brick factory problem: The status of the conjectures of Zarankiewicz and Hill* (Springer International Publishing, 2016), 1st ed.

[66] C. Zarankiewicz, "On a problem of P. Turan concerning graphs," Fundamenta Mathematicae **41**, 137–145 (1955).

[67] R. A. Spanke and V. E. Benes, "N-stage planar optical permutation network," Applied Optics **26**, 1226–1229 (1987).

[68] M. Bass, C. DeCusatis, J. Enoch, V. Lakshminarayanan, G. Li, C. Macdonald, V. Mahajan, and E. Van Stryland, *Handbook of Optics, Third Edition Volume I: Geometrical and Physical Optics, Polarized Light, Components and Instruments(Set)* (McGraw-Hill, Inc., USA, 2009), 3rd ed.

[69] B. Saleh, *Fundamentals of photonics* (Wiley-Interscience, Hoboken, N.J, 2007).

[70] R. C. Jones, "A new calculus for the treatment of optical systems I. description and discussion of the calculus," Journal of the Optical Society of America **31**, 488–493 (1941).

[71] D. Taillaert, Harold Chong, P. I. Borel, L. H. Frandsen, R. M. De La Rue, and R. Baets, "A compact two-dimensional grating coupler used as a polarization splitter," IEEE Photonics Technology Letters **15**, 1249–1251 (2003).

[72] X. Sun, J. S. Aitchison, and M. Mojahedi, "Realization of an ultra-compact polarization beam splitter using asymmetric MMI based on silicon nitride / silicon-on-insulator platform," Optics Express **25**, 8296–8305 (2017).

[73] D. W. Kim, M. H. Lee, Y. Kim, and K. H. Kim, "Planar-type polarization beam splitter based on a bridged silicon waveguide coupler," Optics Express **23**, 998–1004 (2015).

[74] S. Keyvaninia, H. Boerma, M. Wössner, F. Ganzer, P. Runge, and M. Schell, "Highly efficient passive InP polarization rotator-splitter," Optics Express **27**, 25872–25881 (2019).

[75] M. R. Watts and H. A. Haus, "Integrated mode-evolution-based polarization rotators," Optics Letters **30**, 138–140 (2005).

[76] M. Schumann, T. Bückmann, N. Gruhler, M. Wegener, and W. Pernice, "Hybrid 2D-3D optical devices for integrated optics by direct laser writing," Light: Science & Applications **3** (2014).

[77] M. A. Webster, R. M. Pafchek, A. Mitchell, and T. L. Koch, "Width dependence of inherent tm-mode lateral leakage loss in silicon-on-insulator ridge waveguides," IEEE Photonics Technology Letters **19**, 429–431 (2007).

[78] R. Tummidi, T. Nguyen, A. Mitchell, and T. Koch, "An ultra-compact waveguide polarizer based on "anti-magic widths"," in *8th IEEE International Conference on Group IV Photonics, GFP,* (2011), pp. 104–106.

[79] Y. Xu and J. Xiao, "Design and numerical study of a compact, broadband and low-loss TE-pass polarizer using transparent conducting oxides," Optics Express **24**, 15373–15382 (2016).

[80] P. Dong, Y.-K. Chen, G.-H. Duan, and D. T. Neilson, "Silicon photonic devices and integrated circuits," Nanophotonics **3**, 215–228 (2014).

[81] T. Harter, S. Muehlbrandt, S. Ummethala, A. Schmid, S. Nellen, L. Hahn, W. Freude, and C. Koos, "Silicon–plasmonic integrated circuits for terahertz signal generation and coherent detection," Nature Photonics **12**, 625–633 (2018).

[82] S. Ummethala, T. Harter, K. Koehnle, Z. Li, S. Muehlbrandt, Y. Kutuvantavida, J. Kemal, P. Marin-Palomo, J. Schaefer, A. Tessmann, S. K. Garlapati, A. Bacher, L. Hahn, M. Walther, T. Zwick, S. Randel, W. Freude, and C. Koos, "THz-to-optical conversion in wireless communications using an ultra-broadband plasmonic modulator," Nature Photonics **13**, 519–524 (2019).

[83] S. Schneider, M. Lauermann, P.-I. Dietrich, C. Weimann, W. Freude, and C. Koos, "Optical coherence tomography system mass-producible on a silicon photonic chip," Optics Express **24**, 1573–1586 (2016).

[84] J. Sun, E. Timurdogan, A. Yaacobi, E. S. Hosseini, and M. R. Watts, "Large-scale nanophotonic phased array," Nature **493**, 195–199 (2013).

[85] C. Ranacher, C. Consani, A. Tortschanoff, R. Jannesari, M. Bergmeister, T. Grille, and B. Jakoby, "Mid-infrared absorption gas sensing using a silicon strip waveguide," Sensors and Actuators A: Physical **277**, 117–123 (2018).

[86] A. F. Gavela, D. G. García, J. Ramirez, and L. Lechuga, "Last advances in silicon-based optical biosensors," Sensors **16**, 285 (2016).

[87] A. Nesic, M. Blaicher, T. Hoose, A. Hofmann, M. Lauermann, Y. Kutuvantavida, M. Nöllenburg, S. Randel, W. Freude, and C. Koos, "Photonic-integrated circuits with non-planar topologies realized by 3D-printed waveguide overpasses," Optics Express **27**, 17402–17425 (2019).

[88] T. Hoose, M. Blaicher, J. N. Kemal, H. Zwickel, M. R. Billah, P.-I. Dietrich, A. Hofmann, W. Freude, S. Randel, and C. Koos, "Hardwire-configurable photonic integrated circuits enabled by 3D nano-printing," `https://arxiv.org/abs/1912.09942` (2019).

[89] H. Gehring, M. Blaicher, T. Grottke, and W. H. P. Pernice, "Reconfigurable nanophotonic circuitry enabled by direct-laser-writing," IEEE Journal of Selected Topics in Quantum Electronics **26**, 1–5 (2020).

[90] J. Moughames, X. Porte, L. Larger, M. Jacquot, M. Kadic, and D. Brunner, "3D printed multimode-splitters for photonic interconnects," Optical Materials Express **10**, 2952 (2020).

[91] "Ansys-Lumerical," `https://www.lumerical.com`. Accessed: 2022-03-28.

[92] "Synopsis-RSoft Photonic Device Tools," `https://www.synopsys.com/photonic-solutions/rsoft-photonic-device-tools.html`. Accessed: 2022-03-28.

[93] "Optiwave Photonic Software," `https://optiwave.com/`. Accessed: 2022-03-28.

[94] "MIT Electromagnetic Equation Propagation — MEEP," `https://meep.readthedocs.io/en/latest/`. Accessed: 2022-03-28.

[95] M. Clemens and T. Weil, "Discrete electromagnetism with the finite integration technique," Progress in Electromagnetics Research **32**, 65–87 (2001).

[96] Computer Simulation Technology, *Understanding Time Domain Meshing in CST Microwave Studio®* (2010).

[97] J. B. Pendry, D. Schurig, and D. R. Smith, "Controlling electromagnetic fields," Science **312**, 1780–1782 (2006).

[98] D. Schurig, J. J. Mock, B. J. Justice, S. A. Cummer, J. B. Pendry, A. F. Starr, and D. R. Smith, "Metamaterial electromagnetic cloak at microwave frequencies," Science **314**, 977–980 (2006).

[99] O. Ozgun and M. Kuzuoglu, "Form invariance of Maxwell's equations: The pathway to novel metamaterial specifications for electromagnetic reshaping," IEEE Antennas and Propagation Magazine **52**, 51–65 (2010).

[100] M. Rahm, D. A. Roberts, J. B. Pendry, and D. R. Smith, "Transformation-optical design of adaptive beam bends and beam expanders," Optics Express **16**, 11555 (2008).

[101] D.-H. Kwon and D. H. Werner, "Polarization splitter and polarization rotator designs based on transformation optics," Optics Express **16**, 18731 (2008).

[102] D.-H. Kwon and D. H. Werner, "Flat focusing lens designs having minimized reflection based on coordinate transformation techniques," Optics Express **17**, 7807 (2009).

[103] L. H. Gabrielli, D. Liu, S. G. Johnson, and M. Lipson, "On-chip transformation optics for multimode waveguide bends," Nature Communications **3** (2012).

[104] R. Joseph and A. Taflove, "FDTD Maxwell's equations models for non-linear electrodynamics and optics," IEEE Transactions on Antennas and Propagation **45**, 364–374 (1997).

[105] W. Wang, B. Jüttler, D. Zheng, and Y. Liu, "Computation of rotation minimizing frames," ACM Transactions on Graphics **27**, 1–18 (2008).

[106] M. Deubel, G. von Freymann, M. Wegener, S. Pereira, K. Busch, and C. M. Soukoulis, "Direct laser writing of three-dimensional photonic-crystal templates for telecommunications," Nature Materials **3**, 444–447 (2004).

[107] R. Courant, K. Friedrichs, and H. Lewy, "Über die partiellen Differenzen-gleichungen der mathematischen Physik," Mathematische Annalen **100**, 32–74 (1928).

[108] J. Schneider and S. Hudson, "A finite-difference time-domain method applied to anisotropic material," IEEE Transactions on Antennas and Propagation **41**, 994–999 (1993).

[109] S. G. García, T. M. Hung-Bao, R. G. Martín, and B. G. Olmedo, "On the application of finite methods in time domain to anisotropic dielectric waveguides," IEEE Transactions on Microwave Theory and Techniques **44**, 2195–2206 (1996).

[110] M. Nauta, M. Okoniewski, and M. Potter, "FDTD method on a Lebedev grid for anisotropic materials," IEEE Transactions on Antennas and Propagation **61**, 3161–3171 (2013).

[111] M. Salmasi, M. E. Potter, and M. Okoniewski, "Implementation of general dispersive anisotropic materials in Lebedev FDTD," IEEE Transactions on Antennas and Propagation **66**, 7171–7179 (2018).

[112] C. Fong, "Elliptification of rectangular imagery," `https://arxiv.org/abs/1709.07875` (2019).

[113] M. Hochberg, N. C. Harris, R. Ding, Y. Zhang, A. Novack, Z. Xuan, and T. Baehr-Jones, "Silicon photonics: The next fabless semiconductor industry," IEEE Solid-State Circuits Magazine **5**, 48–58 (2013).

[114] L. Chrostowski and M. Hochberg, *Silicon Photonics Design* (Cambridge University Press, 2015).

[115] Y. Liu, J. M. Shainline, X. Zeng, and M. A. Popović, "Ultra-low-loss CMOS-compatible waveguide crossing arrays based on multimode Bloch waves and imaginary coupling," Optics Letters **39**, 335 (2014).

[116] M. R. Garey and D. S. Johnson, "Crossing number is NP-complete," SIAM Journal on Algebraic Discrete Methods **4**, 312–316 (1983).

[117] A. W. Ivan Kaminow, Tingye Li, ed., *Optical fiber telecommunications* (Elsevier Science Publishing Company, Inc., 2013).

[118] F. Chang, K. Onohara, and T. Mizuochi, "Forward error correction for 100 G transport networks," IEEE Communications Magazine **48**, S48–S55 (2010).

[119] K. Itoh, Y. Kuno, Y. Hayashi, J. Suzuki, N. Hojo, T. Amemiya, N. Nishiyama, and S. Arai, "Crystalline/amorphous Si integrated optical couplers for 2D/3D interconnection," IEEE Journal of Selected Topics in Quantum Electronics **22**, 255–263 (2016).

[120] J. Chiles, S. Buckley, N. Nader, S. W. Nam, R. P. Mirin, and J. M. Shainline, "Multi-planar amorphous silicon photonics with compact interplanar couplers, cross talk mitigation, and low crossing loss," APL Photonics **2**, 116101 (2017).

[121] K. Shang, S. Pathak, B. Guan, G. Liu, and S. J. B. Yoo, "Low-loss compact multilayer silicon nitride platform for 3D photonic integrated circuits," Optics Express **23**, 21334 (2015).

[122] K. Shang, S. Pathak, G. Liu, S. Feng, S. Li, W. Lai, and S. J. B. Yoo, "Silicon nitride tri-layer vertical Y-junction and 3D couplers with arbitrary splitting ratio for photonic integrated circuits," Optics Express **25**, 10474 (2017).

[123] A. M. Jones, C. T. DeRose, A. L. Lentine, D. C. Trotter, A. L. Starbuck, and R. A. Norwood, "Ultra-low crosstalk, CMOS compatible waveguide crossings for densely integrated photonic interconnection networks," Optics Express **21**, 12002 (2013).

[124] W. D. Sacher, Y. Huang, G.-Q. Lo, and J. K. S. Poon, "Multilayer silicon nitride-on-silicon integrated photonic platforms and devices," Journal of Lightwave Technology **33**, 901–910 (2015).

[125] K. Suzuki, R. Konoike, K. Tanizawa, S. Suda, H. Matsuura, K. Ikeda, S. Namiki, and H. Kawashima, "Ultralow-crosstalk and broadband multi-port optical switch using SiN/Si double-layer platform," in *Opto-Electronics and Communications Conference (OECC),* (2017), p. PDP3.

[126] W. D. Sacher, J. C. Mikkelsen, P. Dumais, J. Jiang, D. Goodwill, X. Luo, Y. Huang, Y. Yang, A. Bois, P. G.-Q. Lo, E. Bernier, and J. K. S. Poon, "Tri-layer silicon nitride-on-silicon photonic platform for ultra-low-loss crossings and interlayer transitions," Optics Express **25**, 30862 (2017).

[127] Q. Cheng, L. Y. Dai, M. Bahadori, N. C. Abrams, P. E. Morrissey, M. Glick, P. O'Brien, and K. Bergman, "Si/SiN microring-based optical router in switch-and-select topology," in *2018 European Conference on Optical Communication (ECOC),* (IEEE, 2018).

[128] W. D. Sacher, J. C. Mikkelsen, Y. Huang, J. C. C. Mak, Z. Yong, X. Luo, Y. Li, P. Dumais, J. Jiang, D. Goodwill, E. Bernier, P. G.-Q. Lo, and J. K. S. Poon, "Monolithically integrated multilayer silicon nitride-on-silicon waveguide platforms for 3-D photonic circuits and devices," Proceedings of the IEEE **106**, 2232–2245 (2018).

[129] A. Nesic, M. Blaicher, T. Hoose, M. Lauermann, Y. Kutuvantavida, W. Freude, and C. Koos, "Hybrid 2D/3D photonic integration for non-planar circuit topologies," in *ECOC 2016; 42nd European Conference on Optical Communication,* (2016), pp. 1–3.

[130] T. Hoose, M. Billah, M. Blaicher, P. Marin, P.-I. Dietrich, A. Hofmann, U. Troppenz, M. Moehrle, N. Lindenmann, M. Thiel, P. Simon, J. Hoffmann, M. L. Goedecke, W. Freude, and C. Koos, "Multi-chip integration by photonic wire bonding: Connecting surface and edge emitting lasers to silicon chips," in *Optical Fiber Communication Conference,* (OSA, 2016).

[131] C. Galland, A. Novack, Y. Liu, R. Ding, M. Gould, T. Baehr-Jones, Q. Li, Y. Yang, Y. Ma, Y. Zhang, K. Padmaraju, K. Bergmen [sic], A. E.-J. Lim, G.-Q. Lo, and M. Hochberg, "A CMOS-compatible silicon photonic platform for high-speed integrated opto-electronics," in *Integrated Photonics: Materials, Devices, and Applications II,* J.-M. Fédéli, L. Vivien, and M. K. Smit, eds. (SPIE, 2013).

[132] E. de Klerk, J. Maharry, D. V. Pasechnik, R. B. Richter, and G. Salazar, "Improved bounds for the crossing numbers of $K_{m,n}$ and K_n," SIAM Journal on Discrete Mathematics **20**, 189–202 (2006).

[133] A. Errera, "Un théorème sur les liaisons," Comptes Rendus de l'Académie des sciences (Paris) **177**, 489–491 (1923).

[134] Y. Nasu, M. Kohtoku, Y. Hibino, and Y. Inoue, "Waveguide interconnection in silica-based planar lightwave circuit using femtosecond laser," Journal of Lightwave Technology **27**, 4033–4039 (2009).

[135] W. Song, R. Gatdula, S. Abbaslou, M. Lu, A. Stein, W. Y.-C. Lai, J. Provine, R. F. W. Pease, D. N. Christodoulides, and W. Jiang, "High-density waveguide superlattices with low crosstalk," Nature Communications **6** (2015).

[136] J. Pfeifle, L. Alloatti, W. Freude, J. Leuthold, and C. Koos, "Silicon-organic hybrid phase shifter based on a slot waveguide with a liquid-crystal cladding," Optics Express **20**, 15359 (2012).

[137] L. Alloatti, D. Korn, J. Pfeifle, R. Palmer, S. Koeber, M. Baier, R. Schmogrow, S. Diebold, P. Pahl, T. Zwick, H. Yu, W. Bogaerts, R. Baets, M. Fournier, J. Fedeli, R. Dinu, C. Koos, W. Freude, and J. Leuthold, "Silicon-organic hybrid devices," in *Silicon Photonics VIII,* J. Kubby and G. T. Reed, eds. (Proc. SPIE 8629, 2013).

[138] J. Li, M. R. Billah, P. C. Schindler, M. Lauermann, S. Schuele, S. Hengsbach, U. Hollenbach, J. Mohr, C. Koos, W. Freude, and J. Leuthold, "Four-in-one interferometer for coherent and self-coherent detection," Optics Express **21**, 13293–13304 (2013).

[139] D. Dai and J. E. Bowers, "Novel ultra-short and ultra-broadband polarization beam splitter based on a bent directional coupler," Optics Express **19**, 18614–18620 (2011).

[140] C.-W. Hsu, T.-K. Chang, J.-Y. Chen, and Y.-C. Cheng, "8.3 µm in length and CMOS compatible polarization beam splitter based on an asymmetrical directional coupler," Applied Optics **55**, 3313–3318 (2016).

[141] H. Guan, A. Novack, M. Streshinsky, R. Shi, Q. Fang, A. E.-J. Lim, G.-Q. Lo, T. Baehr-Jones, and M. Hochberg, "CMOS-compatible highly efficient polarization splitter and rotator based on a double-etched directional coupler," Optics Express **22**, 2489–2496 (2014).

[142] Z. Lu, Y. Wang, F. Zhang, N. A. F. Jaeger, and L. Chrostowski, "Wide-band silicon photonic polarization beamsplitter based on point-symmetric cascaded broadband couplers," Optics Express **23**, 29413–29422 (2015).

[143] F. Zhang, J. Zheng, Y. Song, W. Liu, P. Xu, and A. Majumdar, "Ultra-broadband and compact polarizing beam splitter in silicon photonics," OSA Continuum **3**, 560–567 (2020).

[144] V. Hahn, S. Kalt, G. M. Sridharan, M. Wegener, and S. Bhattacharya, "Polarizing beam splitter integrated onto an optical fiber facet," Optics Express **26**, 33148–33157 (2018).

[145] T. Barwicz, M. R. Watts, M. A. Popović, P. T. Rakich, L. Socci, F. X. Kärtner, E. P. Ippen, and H. I. Smith, "Polarization-transparent microphotonic devices in the strong confinement limit," Nature Photonics **1**, 57–60 (2007).

[146] A. Muller, J. Breguet, and N. Gisin, "Experimental demonstration of quantum cryptography using polarized photons in optical fibre over more than 1 km," Europhysics Letters (EPL) **23**, 383–388 (1993).

[147] T. M. Babinec, B. J. M. Hausmann, M. Khan, Y. Zhang, J. R. Maze, P. R. Hemmer, and M. Lončar, "A diamond nanowire single-photon source," Nature Nanotechnology **5**, 195–199 (2010).

[148] P. Müller, R. Müller, L. Hammer, C. Barner-Kowollik, M. Wegener, and E. Blasco, "STED-inspired laser lithography based on photoswitchable spirothiopyran moieties," Chemistry of Materials **31**, 1966–1972 (2019).

[149] G. Raybon, A. L. Adamiecki, S. Randel, C. Schmidt, P. J. Winzer, A. Konczykowska, F. Jorge, J.-Y. Dupuy, L. L. Buhl, S. Chandrasekhar, X. Liu, A. H. Gnauck, C. Scholz, and R. Delbue, "All-ETDM 80-Gbaud (640-Gb/s) PDM 16-QAM generation and coherent detection," IEEE Photonics Technology Letters **24**, 1328–1330 (2012).

[150] C. Kuratowski, "Sur le problème des courbes gauches en topologie," Fundamenta Mathematicae **15**, 271–283 (1930).

[151] R. Diestel, *Graph Theory* (Springer Berlin Heidelberg, 2017).

[152] M. Schaefer, *Crossing numbers of graphs* (Taylor & Francis Inc, 2017).

[153] A. Riskin, "On the outerplanar crossing numbers of $K_{m,n}$," Bulletin of the Institute of Combinatorics and its Applications **39**, 16–20 (2003).

[154] "CST — Computer simulation technology," `https://www.cst.com/`.

[155] S. Dottermusch, D. Busko, M. Langenhorst, U. W. Paetzold, and B. S. Richards, "Exposure-dependent refractive index of Nanoscribe IP-Dip photoresist layers," Optics Letters **44**, 29–32 (2019).

[156] B. Heffner, "Deterministic, analytically complete measurement of polarization-dependent transmission through optical devices," IEEE Photonics Technology Letters **4**, 451–454 (1992).

List of publications

Patent applications

[P1] **A. Nesic**, M. Blaicher, and C. Koos, "Verfahren und Vorrichtung zur Polarisationsstrahlteilung und optischen Kopplung," Schutzrechtanmeldung 102020204641.7, (2020).

[P2] M. Blaicher, A. Hofmann, P. Maier, Y. Xu, **A. Nesic**, and C. Koos, "Optisches Wellenleiterbauelement und Verfahren zu dessen Herstellung," Schutzrechtanmeldung 102020212112.5, (2020).

Journal publications

[J1] **A. Nesic**, M. Blaicher, E. Orlandini, T. Olariu, M. Paszkiewicz, F. Negredo, P. Kraft, M. Molochkova, A. Hofmann, W. Dörfler, C. Rockstuhl, W. Freude, and C. Koos, "Transformation-optics modeling of 3D-printed freeform waveguides," Submitted for publication to Optics Express (2022).

[J2] **A. Nesic**, M. Blaicher, P. Marin-Palomo, C. Füllner, S. Randel, W. Freude, and C. Koos, "Ultra-broadband polarization beam splitter and rotator based on 3D-printed waveguides," To be submitted for publication to Light: Science & Applications (2022).

[J3] **A. Nesic**, M. Blaicher, T. Hoose, A. Hofmann, M. Lauermann, Y. Kutuvantavida, M. Nöllenburg, S. Randel, W. Freude, and C. Koos, "Photonic-integrated circuits with non-planar topologies realized by 3D-printed waveguide overpasses," Optics Express **27**, 17402–17425 (2019).

[J4] M. R. Billah, M. Blaicher, T. Hoose, P.-I. Dietrich, P. Marin-Palomo, N. Lindenmann, **A. Nesic**, A. Hofmann, U. Troppenz, M. Moehrle, S. Randel, W. Freude, and C. Koos, "Hybrid integration of silicon photonics circuits and InP lasers by photonic wire bonding," Optica **5**, 876 (2018).

[J5] F. Negredo, M. Blaicher, **A. Nesic**, P. Kraft, J. Ott, W. Dörfler, C. Koos, and C. Rockstuhl, "Fast and reliable method to estimate losses of single-mode waveguides with an arbitrary 2D trajectory," Journal of the Optical Society of America A **35**, 1063–1073 (2018).

Conference publications

[C1] C. Koos, W. Freude, S. Randel, M. R. Billah, M. Blaicher, P.-I. Dietrich, T. Hoose, Y. Xu, J. N. Kemal, **A. Nesic**, and A. Hofmann, "Photonic wire bonding and 3D nanoprinting in photonic integration – from lab demonstrations to production," in *European Conference on Optical Communication (ECOC),* (IEEE 2018).

[C2] C. Koos, W. Freude, M. Blaicher, M. R. Billah, T. Hoose, P.-I. Dietrich, **A. Nesic**, N. Lindenmann, and A. Hofmann, "Hybrid photonic multi-chip integration enabled by 3D nano-printing," in *2017 IEEE Photonics Conference (IPC) Part II,* (IEEE 2017).

[C3] C. Koos, W. Freude, S. Randel, M. R. Billah, M. Blaicher, T. Hoose, P.-I. Dietrich, **A. Nesic**, and A. Hofmann, "3D printing for advanced photonic integration," in *634. WE-Heraeus-Seminar; Merging Micro- and Nano-Optics: 3D Printing for Advanced and Functional Optics,* (2017).

[C4] **A. Nesic**, M. Blaicher, T. Hoose, M. Lauermann, Y. Kutuvantavida, W. Freude, and C. Koos, "Hybrid 2D/3D photonic integration for non-planar circuit topologies," in *ECOC 2016; 42nd European Conference on Optical Communication,* paper W.3.F.4., (2016).

[C5] **A. Nesic**, R. Palmer, S. Koeber, D. Korn, S. Koenig, D. L. Elder, L. R. Dalton, W. Freude and C. Koos, "Demonstration of difference frequency generation in a silicon slot waveguide," in *CLEO 2014; Conference on lasers and Electro-Optics*, paper STh1I.2, (OSA 2014).

[C6] C. Koos, W. Freude, J. Leuthold, L. Alloatti, R. Palmer, D. Korn, J. Pfeifle, P. C. Schindler, M. Lauermann, **A. Nesic**, N. Lindenmann, S. Koeber, T. Hoose, and M. R. Billah "Silicon-organic hybrid (SOH) integration, photonic wire bonding, and frequency combs: Technologies for multi-terabit/s interconnects" in *International Nano-Optoelectronics Workshop iNOW-2013, Cargèse, France,* (2013).

[C7] **A. Nesic**, L. Alloatti, J. Pfeifle, N. Lindenmann, J. Leuthold, W. Freude, and C. Koos "Highly efficient silicon-organic hybrid (SOH) phase shifters for reconfigurable ultra-fast signal processing," in *International Nano-Optoelectronics Workshop iNOW-2013, Cargèse, France,* (2013).

Acknowledgments

Reichel, as well as to my peers Mr. Fernando Negredo, Ms. Maria Paszkiewicz, Ms. Mariia Sukhova, Mr. Pascal Kraft, and Dr. Julian Ott, I thank for the collaboration within the DFG project Wave Phenomena.

I thank Prof. Dr. Maria Axenovich and Prof. Dr. Martin Nöllenburg for discussions on graph theory problems.

I thank my KSOP mentor, Dr. Martin Lauer, for regular mentor meetings, and his suggestions and advices whenever I raised a question or presented a problem.

I want to thank Center for Functional Nanostructures (CFN) staff at the KIT for cleanroom, mask aligner, plasma cleaner, and SEM introduction and to all lecturers and demonstrators of the KSOP modules that I attended. I also thank organizing committees of the conferences and summer schools that I visited, especially to Prof. Dr. Dieter Bimberg of TU Berlin for the summer school iNOW in Cargèse in 2013 and to Prof. Dr. Roel Bats of Ghent University for the Silicon Photonics Summer School in Ghent in 2014. Special thanks go to sponsors who kindly provided rewards for my paper and poster contributions: ADVA Optical Networking, OSKar - Optics Students Karlsruhe e.V., Laztec AG, Sentech GmbH, PBC Lasers GmbH, u^2t Photonics AG, and Russell Berrie Nanotechnology Institute Technion.

I thank my numerous colleagues at IPQ for the wonderful collaboration during all these years. I thank my office mates Dr. Simon Schneider, Dr. Claudius Weimann, Dr. Philipp Trocha, and Dr. Huanfa Peng for the pleasant working atmosphere. Dr. Dietmar Korn, and Dr. Jörg Pfeifle I thank for introducing me to the labs at IPQ at the beginning of my PhD. I would like to thank Dr. Robert Palmer for explaining me all possible lab devices and setups, and Dr. Sven König for explaining me the 40G setup. I thank Dr. Luca Alloatti for numerous discussions on integrated optical switches and matrices, and for many table football games. I thank Dr. Matthias Lauermann for having the patience to answer all my technical questions, especially questions related to photonic integrated circuit design. I express my gratitude to Dr. Matthias Blaicher for our numerous discussions that were anything but boring, and that resulted in many interesting projects. I also thank Dr. Simon Schneider

and Dr. Matthias Lauermann for the great time while riding through California before and after CLEO 2014, and to Dr. Claudius Weimann for solving issues with my accommodation in Germany during my stay at ICFO. Them, and all other colleagues not mentioned so far, listed in alphabetical order: Mr. Md Mosaddek Hossain Adib, Mr. Muhammad Rodlin Billah, Mr. Philipp-Immanuel Dietrich, Dr. Carsten Eschenbaum, Mr. Christoph Füllner, Mr. Denis Ganin, Dr. Tobias Harter, Dr. Wladislaw Hartmann, Dr. David Hillerkuß, Mr. Tobias Hoose, Mr. Djorn Karnick, Dr. Juned Nassir Kemal, Dr. Clemens Kieninger, Dr. Daria Kohler, Mr. Alexander Kotz, Dr. Sebastian Köber, Ms. Kira Köhnle, Mr. Jonas Krimmer, Dr. Yasar Kutuvantavida, Dr. Jingshi Li, Dr. Nicole Lindenmann, Dr. Alexandra Ludwig, Mr. Md Salek Mahmud, Mr. Pascal Maier, Dr. Pablo Marin-Palomo, Dr. Argishti Melikyan, Dr. Johannes Milvich, Mr. Sascha Mühlbrandt, Dr. Sean O'Duill, Dr. Philipp Schindler, Dr. René Schmogrow, Mr. Alban Sherifaj, Mr. Stefan Singer, Ms. Mareike Trappen, Dr. Sandeep Ummethala, Dr. Stefan Wolf, Mr. Sentayehu Fetene Wondimu, Mr. Yilin Xu, and Dr. Heiner Zwickel, I thank for the great time at work and leisure; whether it was going to a Bundesliga football game, ice skating, bowling, or simply going out for beer, it was always pleasurable.

To my colleagues at ICFO, and my office mates from the students' room I thank for the enjoyable time. I specially thank Dr. Miquel Rudé, Dr. Davide Luca Janner, and Dr. Vahagn Mkhitaryan for their support in the lab work.

I also thank my Erasmus Mundus classmates, and to other PhD students with whom I had fruitful discussions at numerous summer schools and conferences.

I would like to thank Mr. Fernando Negredo, Mr. Marcel Schnirring, Mr. Tobias Wingert, Ms. Olga Rikhter, Mr. Tudor Olariu, and Mr. Emilio Orlandini for doing their Bachelor and Master theses under my supervision and supporting my research work. Nonetheless, I am grateful to students who did their research projects, assistantships, and seminar courses in the frame of their KSOP Master studies on topics that I offered: Mr. Alam Bhuiyan Ifte Khairul, Ms. Lisa Kadner, Ms. Olga Rikhter, Mr. Min Chen, Mr. Ashish Thatavarthy, and Mr. Velat Kiliç.